1-1-2013

Synthesis and Characterization of One Dimensional Boron-Based Nanomaterials

Rui Li
University of South Carolina - Columbia

SYNTHESIS AND CHARACTERIZATION OF ONE DIMENSIONAL BORON-BASED NANOMATERIALS

by

Rui Li

Bachelor of Materials Science and Engineering
China University of Geosciences in Beijing, 2005

Master of Applied Chemistry
China University of Geosciences in Beijing, 2007

Submitted in Partial Fulfillment of the Requirements

For the Degree of Doctor of Philosophy in

Mechanical Engineering

College of Engineering and Computing

University of South Carolina

2013

Accepted by:

Xiaodong Li, Major Professor

Anthony Reynolds, Committee Member

Guiren Wang, Committee Member

Goutam Koley, Committee Member

Lacy Ford, Vice Provost and Dean of Graduate Studies

DEDICATION

To

My Family

ACKNOWLEDGEMENTS

First of all, I would like to take this opportunity to sincerely thank my advisor, Dr. Xiaodong Li, for his crucial advice, guidance and support in the research and courses of my graduate work. He deeply impresses on me his enthusiasm towards scientific research, his forsight in the field of nano community, and his extremely hard work to support the group. This dissertation could not be finished without his guidance and support. I highly appreciate all the efforts he has made for me since the beginning of my graduate study in Fall 2007.

I am very grateful for having an exceptional doctoral committee and wish to thank Dr. Tony Reynolds, Dr. Guiren Wang, Dr. Goutam Koley, for their valuable comments, suggestions and encouragement.

I would like to thank Dr. Andreas Heyden and Dr. Jianmin Lu for the assistance with DFT calculation. And thank Dr. Soumitra Ghoshroy, Ms. Jibin Zhao, Dr. Douglas Blom at the USC Electron Microscopy Center. And thank Dr. Hans-Conrad zur Loye and his group members for the characterization service. Thank Dr. Shuguo Ma for the XPS testing.

Many thanks to our group members and alumni: Dr. Zhihui Xu, Dr. Xinnan Wang, Dr. Xinyong Tao, Dr. Lihong Bao, Dr. Jianfeng Zang, Dr. Yong Sun, Dr. Zaiwang Huang, Dr. Dalai Jin, Mr. Peng Huang, Mr. Yingchao Yang, Mr. Haoze Li, Ms. Mantong

Zhao, Mr. Boran Zhou, Mr. Jianchao Chen, Mr. Yanming He, Ms. Ningning Song and Ms. Yang Sun.

I would like to especially thank my parents and my family for their constant support and loves.

ABSTRACT

One dimensional (1D) metal borate and boride nanomaterials have attracted tremendous attention due to their good chemical inertness, high-temperature stability, excellent mechanical properties, and low thermal expansion coefficient.

Beta-BaB_2O_4 (BBO) is a well-known nonlinear optical material with a high second-order nonlinear susceptibility, wide transparency range, and high damage threshold. Using a low temperature, organic-free hydrothermal technique, single-crystalline barium polyborate $Ba_3B_6O_9(OH)_6$ (BBOH) nanorods were synthesized. It was found that BBO nanospindles can be achieved by annealing the BBOH nanorods at a relatively low temperature of 810 ^oC. Transmission electron microscopy (TEM), X-ray diffraction (XRD), and X-ray photoelectron spectroscopy (XPS) techniques were used to characterize these nanomaterials. The formation mechanisms are discussed in conjunction with the crystallographic characteristics and surface energy of the BBOH nanorods and BBO nanospindles. UV-vis absorption spectra demonstrated that both BBOH nanorods and BBO nanospindles are transparent from the ultraviolet to the visible regions.

Single crystalline strontium borate (SrB_2O_4) nanorods were synthesized for the first time via a sol-gel route at low temperature. The SrB_2O_4 nanorods have a good crystalline nature and they are transparent from the ultraviolet to the visible regimes. Nanoscale three-point bending tests were performed directly on individual nanorods to probe their mechanical properties using an atomic force microscope. The elastic modulus

of SrB_2O_4 nanorods was measured to be 158.2 ± 7.9 GPa, exhibiting a significant increase compared with other borate nanostructures and bulk borates. We calculated the Young's moduli of bulk SrB_2O_4 and SrB_2O_4 nanorods with consideration of surface stress effect of nanorods by density functional theory. The simulated results were found consistent with the experimental values.

Zirconium diboride (ZrB_2) is a highly covalent refractory and ultrahigh temperature ceramic material with a hexagonal crystal. This along with its relatively low density of ~6.09 g/cm^3 and good high temperature strength makes it a candidate for high temperature aerospace applications such as hypersonic flight or rocket propulsion systems. We present the synthesis and structural characterization of ZrB_2 nanorods. Single crystalline ZrB_2 nanorods were synthesized for the first time via a simple route at a relatively low temperature of 800 ^oC. The XRD analysis revealed that the as-synthesized nanorods have hexagonal phase of ZrB_2. In this Dissertation, the mechanical properties of ZrB_2 nanorods were also characterized by atomic force microscope-based nanoindentation technique. Furthermore, the Young's modulus of ZrB_2 nanorods was calculated with consideration of surface stress effect of nanorods by density functional theory. This theoretical prediction agrees well with the experimental results.

TABLE OF CONTENTS

LIST OF TABLES

LIST OF FIGURES

LIST OF SYMBOLS

E_n Elastic modulus of SrB_2O_4 nanorods.

I Moment of inertia.

r Radius of the nanorod.

L The suspended length of the nanorod.

F Applied load.

B Bulk modulus.

G Shear modulus.

ν Poisson's ratio.

c_{ij} Elastic constants.

D Diameter.

k_n Spring constant of the nanorod.

LIST OF ABBREVIATIONS

1D ..... One Dimensional

AFM ..... Atomic Force Microscopy

BBO ..... β-BaB_2O_4

BBOH ..... $Ba_3B_6O_9(OH)_6$

CTAB ..... Cetyltrimethylammonium Bromide

CVD ..... Chemical Vapor Deposition

DTA ..... Differential Thermal Analysis

DFT ..... Density Functional Theory

EBID ..... Electron Beam Induced Deposition

EDS ..... Energy Dispersive Spectroscopy

FESEM ..... Field Emission Scanning Electron Microscopy

FFT ..... Fast-Fourier Transform

FTIR ..... Fourier Transform Infrared

HRTEM ..... High-Resolution Transmission Electron Microscopy

SAED ..... Selected Area Electron Diffraction

SEM ..... Scanning Electron Microscopy

TEM ..... Transmission Electron Microscopy

TGA ..... Thermogravimetric Analysis

UV-vis ..... Ultraviolet-Visible

XRD ..... X-Ray Diffraction

XPS ..... X-ray Photoelectron Spectroscopy

CHAPTER 1

Introduction and Literature Review

Boron is a chemical element with chemical symbol B and atomic number 5, and has properties which are borderline between metals and non-metals. Because boron is produced entirely by cosmic ray spallation and not by stellar nucleosynthesis, it is a low-abundance element in both the solar system and the Earth's crust.[1]

Boron-based materials have been widely applied in the areas of glass, ceramics, detergent formulations and bleaching agents, insecticides, semiconductors, magnets, high-hardness and abrasive compounds, shielding in nuclear reactors, and pharmaceutical and biological applications.[1-47]

The literature review on the boron-based nanomaterials in the following sections will be categorized into boron nanomaterials, metal borate nanomaterials and metal boride nanomaterials, in terms of synthesis, properties and applications of these boron-based nanomaterials.

1.1 Boron nanomaterials

Elemental boron is rare and poorly studied because the material is extremely difficult to prepare. Most studies on boron involve samples that contain small amounts of carbon. Chemically, boron behaves more similarly to silicon than to aluminum. Crystalline boron

is chemically inert and resistant to the attack of boiling hydrofluoric or hydrochloric acid. When finely divided, it can be attacked slowly by hot concentrated hydrogen peroxide, hot concentrated nitric acid, hot sulfuric acid or hot mixture of sulfuric and chromic acids.[1]

1.1.1 Synthesis of boron nanomaterials

The crystalline boron nanowires with mean diameter around 10 nm and typical length of several microns were prepared by using Si (100) as a substrate and a simple radio-frequency magnetron sputtering process under argon atmosphere with Au catalyst.[48] The product was influenced by sputtering parameters, such as substrate temperature, sputtering pressure and sputtering time. This method required the vacuum (5.0×10^{-3} Pa), and highly pure argon gas (purity 99.99%) for sputtering deposition growth. Guo *et al.* investigated amorphous boron rich nanowires obtained on ZrB_2 particles using diborane as the gas precursor in a chemical vapor deposition (CVD) process under 20 Torr pressure and at 900 ^{o}C.[49] The gas precursor, diborane, is toxic and harmful to the environment. Vapor-liquid-solid processing of boron nanowires were carried out either using a bottom-up or top-down growth mode.[50] Tian *et al.* studied the patterned boron nanowires on the substrate of Si(111) wafer by thermoreduction method.[51] The patterns on the Si wafer were large-scale and uniform. For the thermoreduction method, three factors have to be considered: the concentration of the nanoparticle solution; the dosage of the solution; the temperature of the wafer. By considering these factors, Tian *et al.* also synthesized flexible boron nanowires via thermoreduction method in boron-oxygen

compounds.[52] Large-scale arrays of feather-like boron nanowires were prepared using magnetron sputtering with a target of highly pure boron and boron oxide mixture.[53] The branched boron nanofeathers always nucleated and grew on the same sidewall of the backbone nanowire. Yang *et al.* reported aligned single crystal boron nanowires by using nanochannel-Al_2O_3 as a substrate and a CVD process.[54] Crystalline boron nanowires were formed on Pt coated sapphire substrates using pulsed laser ablation at different temperatures under the pressure of 50 Pa.[55,56] The synthesis temperatures, intensities of the laser beams, the types of the metal catalysts are the main factors on the growth for pulsed laser ablation method. Zhang *et al.* used boron powders as boron source and, Si and Ni as catalysts to synthesize boron nanowires.[57] For this method, Si and Ni were critical in the synthesis of the boron nanowires. In addition, the boron nanowire yield was significantly improved when Si was added.

All the methods mentioned above have been used to synthesize boron nanomaterials. However, the product purity is low due to the carbon contamination. The synthesis parameters, such as synthesis temperature, compositions of the targets, are not studied systemically in most of these works. Furthermore, diborane, used as the gas precursor, is toxic and harmful to the environment. Therefore, it tends to avoid using diborane for developing the methods for synthesizing boron nanomaterials. It remains a great challenge to develop a not only easy, cost-effective, productive, but also environment-friendly technique for synthesizing boron nanomaterials.

1.1.2 Properties of boron nanomaterials

Boron is a trivalent element possessing strong covalent bonds.[49] As the nearest neighbor of carbon in the Periodic Table of the Elements, boron has exceptional properties, such as low density, low volatility, good resistance to corrosion, and high melting point. It is stronger than steel, harder than corundum, and lighter than aluminum.[58] Boron is one of the hardest materials known (Vicker's hardness, Hv = 3000 kg·mm^{-2}).[49] The mechanical response of crystalline boron nanowires was studied with the mechanical resonance method and tensile testing.[59] The mechanical resonances of cantilevered boron nanowires were excited and their frequencies were used to obtain the Young's modulus of the nanowires, according to simple beam theory.[60] Electrical-transport studies on individual boron nanowires distinguished them as p-type semiconductors with low carrier mobility.[61] It has been revealed that there are six stable configurations of boron nanowires obtained by growing along different base vectors from the unit cell of the bulk alpha-rhombohedral boron (alpha-B) and beta-rhombohedral boron (beta-B). It has been well known that, the bulk boron is usually metallic without magnetic property. However, theoretical results about the magnetic and electronic properties showed that, for both the alpha-B-based and the beta-B-based nanowires, the magnetic property was dependent on the growth direction. When the boron nanowires grew along the base vector [001], they exhibited ferromagnetism with the magnetic moments of 1.98 and 2.62 μ_B for the alpha-c [001] and beta-c [001] directions, respectively. Electronically, when the boron nanowires grew along the alpha-c [001] direction, it showed semiconducting with the direct bandgap

of 0.19 eV. So boron nanowires possessed the unique direction dependence of the magnetic and semiconducting behaviors, which was distinctly different from that of the bulk boron. Therefore, these theoretical findings would bring boron nanowires to many promising applications.[58,61] High-pressure induced superconductivity in boron nanowires with rhombohedral crystal structure was studied by Sun *et al*.[62] These boron nanowires became superconductors with T(c)=1.5 K at 84 GPa, while bulk beta-r-B was still a semiconductor at the same pressure.[62] There was a study showing that the boron nanowire films had good field emission characteristics. The turn-on field was 9.0 V/μm and the threshold field was 14 V/μm.[63] This turn-on field value of boron nanowires is better than that of In_2O_3 nanowires and GaN nanowires, but higher than that of graphene (turn-on electric field of 0.7 V/m) and carbon nanotube (turn-on electric field of 2-3 V/m).[173,174]

In summary, these exceptional properties of boron nanomaterials, including mechanical, magnetic, conductive and optical properties, have been well reported. However, it is still not clear regarding the mechanism that governs these novel properties of boron nanomaterials with reference to the bulk boron materials. The properties of boron nanowires must be further studied in terms of solid-state physics and solid-state chemistry.

1.1.3 Applications of boron nanomaterials

Boron nanomaterials should find applications in many areas, such as semiconductors, flat plane display and electron emission nanodevices, high-hardness and abrasive

compounds.[51,52] Electrical-transport studies on individual boron nanowires established them as p-type semiconductors with low carrier mobility.[61] Boron nanowires with rhombohedral crystal structure could serve as superconductors.[62] It was reported that the boron nanowires could be applied in the field emission community, such as flat plane display and electron emission nanodevices.[63]

The bulk boron materials have been used in various fields, such as in the fields of glass, ceramics, detergent formulations and bleaching agents, insecticides, magnets, high-hardness and abrasive compounds, shielding in nuclear reactors. Some applications of the boron nanomaterials have been reported as mentioned above. However, more applications need to be investigated by learning from the well-developed applications of bulk boron materials, such as those in the fields of glass, ceramics, magnets, high-hardness, abrasive, and shielding in nuclear reactors.

1.2 Metal borate nanomaterials

Recently, more and more attention has been paid to the preparation and characterization of nanowires of the family of one dimensional metal borate nanomaterials due to their novel properties, such as chemical inertness, high-temperature stability, excellent mechanical properties, and low thermal expansion coefficient.[1-47] In this section, synthesis, properties and applications of metal borate nanomaterials will be reviewed.

1.2.1 Synthesis of metal borate nanomaterials

Nanowires of metal borates $Al_{18}B_9O_{33}$ and MgB_4O_7 were synthesized by thermal evaporation of mixed powders containing metal oxide (Al_2O_3 or MgO) and boron

oxide.[13] This method may allow researchers to choose and combine other interesting oxide vapors to fabricate nanowires of new compounds. Anderson *et al.* investigated the phase transformations (dehydration, amorphization, crystallization, polymorphic transitions), thermal expansion of $M^+B_5O_6(OH)_4 \cdot 2H_2O$ (M^+ = K, Rb, Cs) compounds and the polymorphic transformations of the CsB_5O_8 compound.[90] Raja *et al.* prepared single crystals of potassium pentaborate ($KB_5O_8 \cdot 4H_2O$ or KB5) by low temperature solution growth methods.[16] High-aspect-ratio and single-crystal aluminum borate ($Al_{18}B_4O_{33}$) nanowire bundles with an ordered orientation were formed by using an innovative sucrose-assisted growth process.[18] Sucrose, used as the monodispersed solvent and a novel adhesive template in this process, is a cheap and safe reactant. Therefore, this process is environment-friendly and easy for the large-scale production of high-aspect-ratio ordered orientation nanowire bundles.

Magnesium borate ($Mg_2B_2O_5$) nanowires were obtained by CVD method.[9] In addition, Ma *et al.* reported single-crystal $Al_{18}B_4O_{33}$ microtubes using solution method followed by annealing at 1050 °C for 1 h under the gas flow of $N_2(H_2)$.[14] Zhao *et al.* synthesized thorn-like polycrystalline $Ca_2B_2O_5 \cdot H_2O$ microspheres with nano-sized slices using boric acid and calcium hydroxide as reactants by a hydrothermal method.[42] This method is catalyst-free, and carried out at low temperature. Hierarchical laminar superstructures of rhombic priceite ($Ca_4B_{10}O_{19} \cdot 7H_2O$) were reported in terms of hydrothermal synthesis, shape evolution, optical, and thermal decomposition properties.[43,47] A sol-gel route followed by calcination was used to grow various aluminum borate nanowires.[19] The

morphology and structure of $Al_4B_2O_9$ and $Al_{18}B_4O_{33}$ nanowires could be controlled by adjusting the boron oxide content in the sol-gel derived precursors and the calcined temperature. Strontium borate $SrBO_2(OH)$ and barium polyborate $Ba_3B_6O_9(OH)_6$ were prepared using hydrothermal techniques.[25] Zhang *et al*. studied uniformly BN-coated $Al_{18}B_4O_{33}$ nanowires by the reaction of $Al_4B_2O_9$ nanowires with ammonia at high temperature.[26] Experimental investigations by in situ providing the precursors for BN coating indicated that the reaction precursors strongly controlled the composition and morphology of aluminum borate nanomaterials. Liu *et al.* reported rod-like nickel borate by a thermal conversion route.[32] These nickel borate rods had a length within the range of 6-20 μm. Therefore, this method is suitable for synthesizing micro-scale materials.

Bulk beta phase barium borate (beta-BaB_2O_4 or BBO) crystals were generally grown by high temperature methods, such as the modified Kyropoulos and Czochralski techniques.[3,6,8] The beta phase crystal could be directly synthesized from a BaB_2O_4 composition melt without flux elements, although the beta phase crystal was metastable.[8] Zhou *et al.* prepared BBO nanoparticles via coprecipitation using different bases as precipitants.[84] Zhao *et al.* reported network-like BBO nanostructures by a sol-gel method.[87] It was a simple, inexpensive, and efficient sol-gel approach as the first example of a morphology-controlled synthesis of BBO nanostructures with novel 1D morphologies. BBO nanofilms were prepared by sol-gel deposition,[12] metal organic chemical vapor deposition,[24] and injection metal organic chemical vapour deposition.[22] In the method of injection metal organic chemical vapour deposition, pulsed precursor

injection was implemented with a vertical downstream apparatus, avoiding continuous precursor injection and an inverted vertical reactor geometry.

To date, only a few of methods mentioned above have been used to synthesize barium borate nanomaterials, such as coprecipitation, sol-gel deposition, and metal organic chemical vapor deposition. Solution methods usually bring pollutions into the nanomaterials. In addition, the productivity and product purity by using these methods are low. Therefore, it remains a great challenge to develop a cost-effective and productive technique for synthesizing metal borate nanomaterials. Meanwhile, in order to obtain high-quality barium borate nanomaterials, we also need to pay more attention to the process of synthesis.

1.2.2 Properties of metal borate nanomaterials

One dimensional metal borate nanomaterials possess chemical inertness, high-temperature stability, excellent mechanical properties, as well as low thermal expansion coefficient.[1-47] Below are the specific properties of metal borate nanomaterials reported in literature.

The optical, mechanical, lubricative and thermal properties of BBO were reported.[4,5,6,11,12] The dielectric constant and loss tangent of single crystals of potassium pentaborate ($KB_5O_8 \cdot 4H_2O$ or KB5) were determined as a function of temperature.[16] A novel fluorine beryllium borate crystal $Sr_{0.23}Ca_{0.77}Na_2Be_2B_2O_6F_2$ has been grown by high temperature solution method from its self-flux system. Optical transmittance spectrum reveals this compound has a very wide transmission range.

The IR spectrum and thermal behavior of $Sr_{0.23}Ca_{0.77}Na_2Be_2B_2O_6F_2$ were also reported.[64] $Li_3Cs_2B_5O_{10}$ was studied to be a congruently melting and deep UV nonlinear optical material.[40] $Ni_3(BO_3)_2$ particles showed remarkable reflection within the visible light wavelength range of 425-690 nm, as well as within the near ultraviolet wavelength range of 270-400 nm.[32] The presence of NaCl during the synthesis did not show significant effect on the UV-vis properties of the $Ni_3(BO_3)_2$ particles.

These novel properties of metal borate nanomaterials mentioned above have been studied, such as optical and mechanical properties. However, we still need to conduct futher investigation on more properties of metal borate nanomaterials with reference to the properties of bulk metal borates, such as chemical inertness, high-temperature stability. The mechanism that controls these novel behaviors must be further studied to explain the novel phenomena and measure new properties, and more attention should be paid to the relationship between the properties and structures of metal borate nanomaterials.

1.2.3 Applications of metal borate nanomaterials

Metal borate nanomaterials could be applied in various fields, such as glass, ceramics, detergent formulations and bleaching agents, insecticides, semiconductors, flat plane display and electron emission nanodevices, magnets, high-hardness and abrasive compounds, and shielding in nuclear reactors.[51,52] In this section, the applications of metal borate nanomaterials will be introduced.

A novel fluorine beryllium borate crystal, $Sr_{0.23}Ca_{0.77}Na_2Be_2B_2O_6F_2$, exhibited a very wide transmission range revealed by optical transmittance spectrum. Thus, it could be used as an optical material.[64] The BBO crystal has typical applications in nonlinear optics, quantum electronics and radiation shielding.[15,17,33,35,41] Potassium pentaborate was reported to be applied in dielectric components.[16] $Li_3Cs_2B_5O_{10}$ is a deep UV nonlinear optical material.[40]

In summary, some applications of metal borate nanomaterials have been reported in the fields, such as optical and mechanical applications. However, we should probe more applications, such as heterogeneous catalysis, sensors, energy conversion and storage, oxidation-resistant and whisker-reinforced composites, by measuring more novel properties of metal borate nanomaterials, understanding the growth mechanism and the relationship between the properties and structures of these metal borate nanomaterials.

1.3 Metal boride nanomaterials

1.3.1 Synthesis of metal boride nanomaterials

CoB thin films were obtained by the electroless coating technique and showed charge/discharge cyclic characteristics.[65] A solid state heterojunction diode based on a micrometer thick n-Mg_2B_{14} on p-type Si substrates was deposited by laser ablation.[66] The mechanochemical synthesis of W_2B_5 powders was carried out at room temperature.[67] TiB_2 were used to promote $LiBH_4$-MgH_2 composite for reversible hydrogen storage by a novel three-step method.[68] Hafnium boride (HfB_2) was applied to improve the anti-oxidation and ablation properties of carbon/carbon (C/C) composites, by using a two-step

process of in situ reaction and thermal gradient chemical vapor infiltration.[69] Tungsten boride compounds were synthesized by self-propagating high-temperature synthesis method and following leaching process.[71] Yin *et al.* reported the strength at elevated temperatures of in-situ toughened ZrB_2-TiB_2 ceramic composites that were prepared via pressureless sintering at 2100 ^oC for 2 h.[72] Yubuta *et al.* investigated the layered boride $YbAlB_4$ single crystals with $YCrB_4$-type and $ThMoB_4$-type phases derived from a hexagonal AlB_2-type.[82] It is significantly important for understanding transport and magnetic properties to reveal the nanostructures of both phases in the real space.

Zirconium diboride (ZrB_2) is a leading material in the category of ultrahigh temperature ceramics (UHTCs) due to very high melting point, high thermal conductivity, good thermal shock resistance, low coefficient of thermal expansion, retention of strength at elevated temperatures and stability in extreme environments.[110-112] Superior mechanical properties (hardness and four-point bending strength), thermal shock and oxidation resistance are due to the highly covalent nature of this ceramic. These properties render it potential candidate to thermal protection system for hypersonic flight and atmospheric reentry and rocket propulsion. When dropped in the atmosphere of earth, the nose cap and leading edge of space crafts have to endure very high temperature and high speed ions ablation.[110] According to the reentry simulation testing, SiC reinforced ZrB_2 composites possess remarkable properties of antiablation capability and oxidation resistance.

1.3.2 Properties of metal boride nanomaterials

Metal borides, in general, have drawn significant attention because of their promising scientific and technological characteristics, such as efficient field emission, high melting point, hardness, chemical stability, antiablation capability, oxidation resistance, superconductivity, semiconducting, thermal neutron detecting, catalysis, wear resistance and magnetic properties.[74,65] This section focuses on the synthesis, properties and applications of metal boride nanomaterials.

Among the metal borides, lanthanum hexaboride was mainly used in making filaments of electron microscope where a high brightness electron source with long service life was required. LaB_6 had a unique combination of desired properties including high melting point, high electrical conductivity, low work function and low vapor pressure at high temperature. This made it one of the best thermionic materials for high electron density cathodes.[74] A solid state heterojunction diode based on a micrometer thick n-Mg_2B_{14} on p-type Si substrates was demonstrated as thermal neutron detector.[66] WB has a lower compressibility at high pressure. From the partial densities of states (PDOS) of WB, it was found that the Fermi level was mostly contributed by the d states of W atom and p states of B atom, and the contributions from the s, p states of W atom and s states of B atom were small.[75] Rodriguez-Castro *et al*. studied the wear resistance of the FeB/Fe_2B layers using the four-ball test.[76] The brittleness results were comparable to the values of ceramic materials, such as sintered carborundum, Al_2O_3, and aluminum oxide nitride. Zirconium and hafnium diboride were two major material systems that were critical for

applications in ultra-high temperature environments where both oxidation and mechanical damage mechanisms (such as creep) were operative.[77] CrB_4 showed an almost temperature-independent paramagnetism, consistent with low-spin Cr-I in a metallic compound. Conductivity measurements confirmed the metallic character.[73] Fe_2B layers showed good fracture toughness determined by the Vickers indentation,[79] and Berkovich nanoindentation.[80] The structure stability, magnetism, electronic structure and elastic properties of Mo_2FeB_2 in nonmagnetic (NM), ferromagnetic (FM) and antiferromagnetic (AF) cases were reported.[70] HoB_{66} and LuB_{66} were studied on the low-temperature specific heat, magnetic susceptibility, and thermal expansion.[81] HoB_{66} had one of the largest magnetic moments among all rare-earth ions, and hence a higher transition temperature into an ordered state might be expected. Nickel boride nanoparticles exhibited the activity of catalysis in hydrogenation reactions.[78] Low temperature hydrogen treatment ($T < 100\ ^oC$) of nickel boride nanoparticles in the presence of ethanol may induce a substantial increase in the catalyst activity for the direct hydrogenation.

In summary, some novel properties of metal boride nanomaterials have been studied and reported as discussed above, such as wear resistance, low-temperature specific heat, magnetic susceptibility, and thermal expansion. However, more novel properties of metal boride nanomaterials still need to be investigated with reference to the bulk metal borides. The mechanism that controls the exceptional performance must be further studied to explain the novel phenomena and test new properties of metal boride

nanomaterials.

1.3.3 Applications of metal boride nanomaterials

Metal boride nanomaterials should find applications in various areas, including glass, ceramics, catalysis, wear resistance, semiconductors, flat plane display and electron emission nanodevices, magnets, high-hardness and abrasive compounds, and shielding in nuclear reactors.[74,65] In this section, the applications of metal borate nanomaterials will be discussed.

Hafnium boride (HfB_2) was applied to improve the anti-oxidation and ablation properties of carbon/carbon (C/C) composites.[69] The wear resistance of the FeB/Fe_2B layers was reported by using the four-ball test.[76] LaB_6 could be used as filaments of electron microscope and thermionic materials for high electron density cathodes.[74] HoB_{66} and LuB_{66} could be applied as magnets due to their low-temperature specific heat, magnetic susceptibility, and thermal expansion.[81] Nickel boride nanoparticles were used as catalyst in hydrogenation reactions.[78] Although these applications of metal boride nanomaterials have been investigated, more applications of these nanomaterials still need to be further studied with reference to the applications of their bulk counterparts.

In our group, $Mg_2B_2O_5$ nanowires with (010) twins were synthesized for the first time using a catalyst-free method. The microstructure of the $Mg_2B_2O_5$ nanowires was extensively studied by cross-sectional high-resolution transmission electron microscopy. The mechanical properties of the $Mg_2B_2O_5$ nanowires were tested by nanoindentation directly on individual nanowires. It was found that the twinned $Mg_2B_2O_5$ nanowires

achieved comparable hardness but 19% decrease in elastic modulus compared to their bulk counterpart. The elastic softening mechanisms of the $Mg_2B_2O_5$ nanowires were discussed with reference to their twin defects, size, and surface effects.[20]

Single crystalline $Ca_2B_2O_5 \cdot H_2O$ (CBOH) nanobelts and stacking faulted $Ca_2B_2O_5$ (CBO) nanogrooves were synthesized by catalyst-free routes and its structural and mechanical properties were characterized.[28] The CBOH nanobelts grew along the [104] direction. The mechanical properties of the CBOH nanobelts (Figure 1.1) and the CBO nanogrooves were tested by nanoindentation performed directly on individual CBOH nanobelts and CBO nanogrooves. The measured elastic modulus and hardness of the CBOH nanobelts were 126.6 ± 15.2 and 6.3 ± 1.2 GPa, respectively. It was found that the CBOH nanobelts, with the presence of hydrated H_2O, achieved 28.7% increase in elastic modulus, whereas the stacking faulted CBO nanogrooves, with the absence of hydrated H_2O, exhibited 99% loss in elastic modulus, compared to bulk CBO.

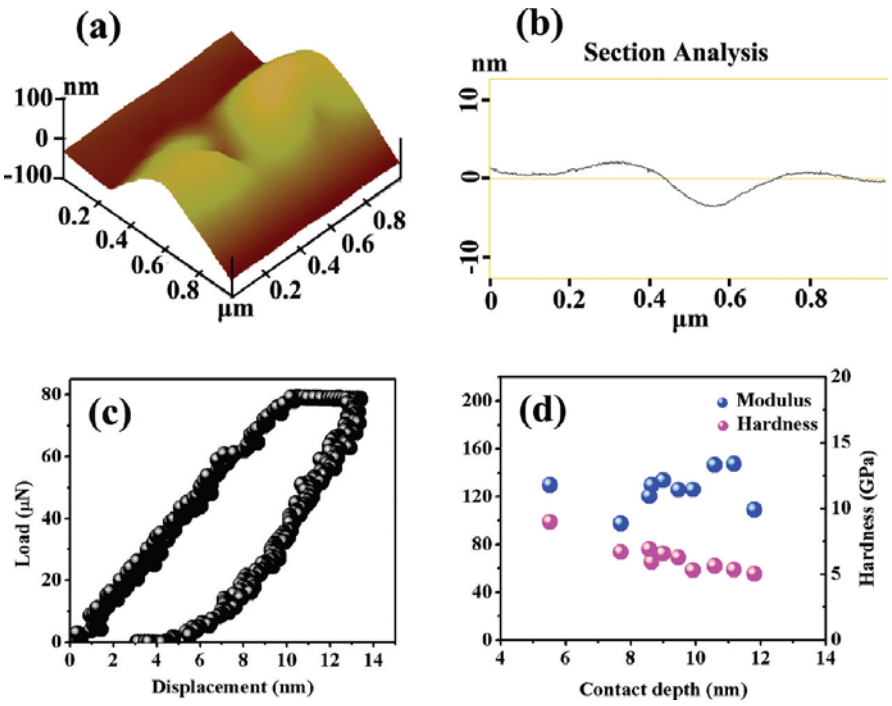

Figure 1.1 Nanoindentation on individual $Ca_2B_2O_5 \cdot H_2O$ (CBOH) nanobelts. (a) 3D AFM image of a nanoindentation mark made on a CBOH nanobelt. (b) Cross-sectional height profile of the nanoindentation mark shown in (a). (c) Representative nanoindentation load-displacement curve. (d) Elastic modulus and hardness of as a function of indentation contact depth. [28]

Two kinds of aluminum borate nanowires, $Al_4B_2O_9$ and $Al_{18}B_4O_{33}$, were synthesized by a one-step combustion method through control of the Al:B atomic ratio and synthesis temperature.[85] Both nanowires are single crystalline but have distinguishing growth habits. Nanomechanical characterization (Figure 1.2) shows the elastic modulus and indentation hardness values of the $Al_4B_2O_9$ nanowires were 102.8 ± 1.3 and 10.4 ± 0.3 GPa, respectively. It was found that the elastic modulus of $Al_{18}B_4O_{33}$ nanowires was reduced by 70% compared with their bulk counterpart. The elastic modulus and hardness values of the $Al_{18}B_4O_{33}$ nanowires were measured to be 121 ± 4 and 12.8 ± 0.4 GPa,

respectively. $Al_{18}B_4O_{33}$ nanowires exhibited higher hardness and elastic modulus than $Al_4B_2O_9$ nanowires.

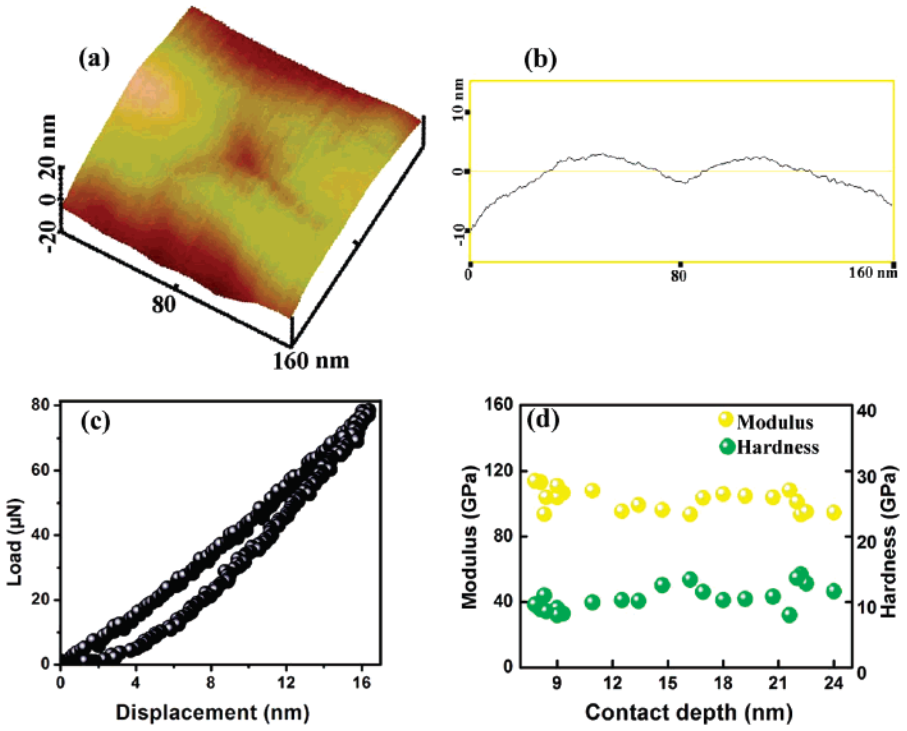

Figure 1.2 (a) Three-dimensional (3D) AFM image of a nanoindentation impression made on a clamped $Al_4B_2O_9$ nanowire. (b) Cross-sectional height profile of the indentation impression shown in (a). (c) Representative nanoindentation load-displacement curve. (d) Elastic modulus and hardness of $Al_4B_2O_9$ nanowires as a function of indentation contact depth.[85]

Necklace-like nanostructures with SiOx beads on boron strings were self-assembled via an environment-friendly method at atmospheric pressure. The electrical conductivity of the boron string was a thousand times higher than that of bulk boron. Due to the unique mechanical interlocking between beads and epoxy matrix, the reinforcement effect of the nanonecklaces in epoxy was better than normal carbon nanotubes. B/SiOx nanonecklaces were expected to exhibit unique electrical and mechanical properties for constructing nanodevices.[107]

Table 1.1 summarizes the synthesis methods, properties and potential applications of boron, borate and boride nanomaterials. Various methods have been used to synthesize these boron-based nanomaterials. However, among these methods, hazardous chemicals or a torch sealed and evacuated tube system is usually essential. For example, the gas precursor, diborane, is usually used to synthesize boron nanomaterials, and it is hazardous to public health and the environment. Therefore, we should develop the methods for synthesizing boron-based nanomaterials without using diborane. It remains a great challenge to develop a not only easy, cost-effective, productive, but also environment-friendly technique for synthesizing boron-based nanomaterials. Meanwhile, we also should pay more attention to the process of synthesis in order to obtain high-quality boron-based nanomaterials. Although the bulk boron-based materials have been used in various fields, the application of boron-based nanomaterials remains an open question. We need to further study the mechanism of the exceptional behaviors mentioned above in these nanomaterials to explain the novel phenomena and measure new properties, especially, pay attention to the relationship between the properties and structures of the boron-based nanomaterials. To the best of our knowledge, only one paper reported the successful production of bulk barium polyborate, $Ba_3B_6O_9(OH)_6$-the first reported chain borate, in which the boron atoms were all tetrahedrally coordinated by oxygen atoms.[25] The $Ba_3B_6O_9(OH)_6$ nanomaterials have not been reported in literature. To date, SrB_2O_4 nanostructures are still absent in literature and their nanoscale-enabled

properties are completely unknown. One dimensional ZrB_2 nanostructures are still lacking and their properties must be further studied.

Table 1.1 Summary of boron, borate and boride nanomaterials.

Nanomaterials	**Synthesis methods**	**Properties**	**Potential Applications**	**Ref.**
boron nanowires	chemical vapor deposition (CVD)	superconductivity T(c)=1.5 K at 84 GPa	superconductor	62
boron nanowire films	CVD	good field emission, turn-on field is 9.0 V/μm and the threshold field is 14 V/μm	nanoscale cool cathode materials in flat panel display devices and electron emission nanodevices	63
boron nanowires	radio-frequency magnetron sputtering process	-	nanodevices	48
amorphous boron rich nanowires	CVD	-	nanodevices	49
boron nanowires	vapor-liquid-solid processing	conductivity with average $V_{critical}$=5.6 V for base-growth, 13.1 V for top-growth; two-	nanodevices	50

		stage behavior of the I–E curves		
patterned boron nanowires	thermoreduction	good field emission: turn-on field is 15 V/μm, and the apparent threshold field is 24 V/μm	nanodevices	51
feather-like boron nanowires	magnetron sputtering	-	nanodevices	53
boron nanowires	pulsed laser ablation	-	nanodevices	55,56
boron nanowires -	-	p-type semiconductivity: ($\delta = 10^{-2}$ $(\Omega\ cm)^{-1}$ with low carrier mobility ($\mu_H = 10^{-3}$ cm^2/Vs), similar to those of bulk boron.	p-type semiconductors	61
B/SiOx nanonecklaces	growth in tube furnace at 1500 ^oC	electrical conductivity, reinforcement effect: hardness=0.34±0.05 GPa, elastic modulus= 4.75±0.39 GPa, a 32.3% increase in elastic modulus, and a 61.9% increase in	electrical and mechanical nanodevices	107

		indentation hardness, compared to the matrix.		
$Al_{18}B_9O_{33}$ nanowires	thermal evaporation	-	nanodevices	13
MgB_4O_7 nanowires	thermal evaporation	-	nanodevices	13
$Al_{18}B_4O_{33}$ nanowire bundles	innovative sucrose-assisted growth process	-	nanodevices	18
$Mg_2B_2O_5$ nanowires	CVD	wide band gap semiconductor: the conductivity is 10^{-4} $(\Omega\ cm)^{-1}$	semiconductor nanodevices	9
$Al_{18}B_4O_{33}$ microtubes	CVD	-	nanodevices	14
Thorn-like $Ca_2B_2O_5 \cdot H_2O$	hydrothermal method	-	optical material	42
$Ca_4B_{10}O_{19} \cdot 7H_2O$ nanosheets	hydrothermal method	weak absorption within the wavelength ranges 280-320 nm (UV region), 550-610 nm, and 750-790 nm(visible region), indicating the quasi transparent characteristic	optical material	43,47
beta-BaB_2O_4	coprecipitation	nonlinear optical	optical	84

nanoparticles		properties	material	
network-like beta-BaB_2O_4	sol-gel method	nonlinear optical properties	optical material	87
beta-BaB_2O_4 nanofilms	sol-gel deposition	nonlinear optical properties	optical material	12
beta-BaB_2O_4 nanofilms	metal organic chemical vapor deposition	optical properties: micro-Raman spectra show an intense peak at 637 cm^{-1} that is the fingerprint of BBO	wave guiding applications	22,24
$KB_5O_8 \cdot 4H_2O$	low temperature solution growth methods	dielectric property	dielectric material	16
$Al_4B_2O_9$ nanowires	sol-gel route followed by calcination	thermal property: a very broad exothermal peak from 100 to 900 ^oC	nanodevices	19
$Al_{18}B_4O_{33}$ nanowires	sol-gel route followed by calcination	thermal property: a constant weight was maintained from 400 to 1000 ^oC	nanodevices	19
$SrBO_2(OH)$	hydrothermal method	thermal property: weight loss of about 6.0% in the range 100–300 ^oC in air	thermal material	25
$Ba_3B_6O_9(OH)_6$	hydrothermal method	thermal property: the	thermal	25

		weight loss corresponding to the removal of the hydroxyl groups is about 7.0% in the range 100–600 ^{o}C in air, with endothermic effects at about 140 and 350 ^{o}C	material	
BN-coated $Al_{18}B_4O_{33}$ nanowires	reaction of $Al_4B_2O_9$ nanowires with ammonia at high temperature	-	-	26
nickel borate	thermal conversion route	-	-	32
$Li_3Cs_2B_5O_{10}$	-	nonlinear optical property	nonlinear optical material	40
$Sr_{0.23}Ca_{0.77}Na_2Be_2B_2O_6F_2$	high temperature solution method from its self-flux system	optical transmittance, thermal behavior	thermal material	64
zinc borate	-	increasing the rapidest decomposition temperature and reducing the decomposition rate of	modification of polymers	123

		wood-flour-polyvinyl chloride composites		
lithium difluoro(oxalato)borate	solution method	electrochemical performances: 0.9 $mol \cdot L^{-1}$ lithium difluoro(oxalato)borate/DMS (1:1, by volume) electrolyte is stability against oxidative decomposition (>5.5 V) and satisfactory conductivity	lithium-ion batteries	124
lithium bis(oxalato)borate	compressing dry granulation method	electrochemical performances: high oxidation potentials (>5.3 V) and satisfactory conductivities	lithium ion batteries	126
$NaSrBO_3:xEu^{3+}$		photoluminescence properties: characteristic red emission of Eu^{3+} ions	phosphors	125
$Mg_2B_2O_5$ nanowires	catalyst-free method	good hardness but 19% decrease in elastic modulus	hard material	20
$Al_4B_2O_9$ nanowires	one-step combustion method	lower hardness and elastic modulus	mechanical area	85

$Al_{18}B_4O_{33}$ nanowires	one-step combustion method	higher hardness and elastic modulus	hard material	85
$Ca_2B_2O_5 \cdot H_2O$ nanobelts	catalyst-free method	elastic modulus	mechanical area	28
$Ca_2B_2O_5$ nanogrooves	catalyst-free method	stacking faulted	mechanical area	28
$LiMnBO_3$ nanoparticle	sol-gel method	electrochemical performances: first discharge capacity of 136 $mAh \cdot g^{-1}$ within a window of 4.7-1.7 Vat C/20 rate.	high-capacity cathode material	127
calcium borate nanoparticles	thermal treatment method via co-precipitation	thermal stability of the annealed samples at higher temperatures	thermal field	128
$Mg_2B_2O_5$ nanorods	soft template method	optical property: Raman spectra	optical material	129
$La_2CaB_{10}O_{19}:Pr^{3+}$ nanocomposites	crystallization from lower temperature solutions	laser operated elasto-optical properties	optical material	130
cerium borate nanoparticles	sol-gel method under micro-emulsion by oleic acid	anti-wear property: friction coefficient of the base oil by the addition of the nanoscale cerium borate particles diminished greatly	anti-wear material	83

nickel borate nanostructures	precursor- mediated route	antiferromagnetic behavior with the Neel temperature ranging from 44 to 47 K	magnet	88
$Al_4B_2O_9$ nanowhiskers	high energy ball-milling pretreatment	-	-	131
$Mg_3B_2O_6$ nanoarchitectures	precipitation reaction and sequential calcination	-	-	132
BN-coated $Al_{18}B_4O_{33}$ nanowhiskers	sol-gel and post-thermal-treatment method	increase in composite hardness by the addition of coated nanowhiskers into Mg alloys	aerospace application	133
$LaBO_3$ hollow nanospheres	soft-template self-assembly process	high coulombic efficiency and charge-discharge cycling capacities of up to 100 cycles in the lithium-ion batteries	lithium-ion batteries	134
Tb modified yttrium borate core-nano silica shell	solid state reaction and sol-gel method	intense green emission	phosphor	135
$Ni_3(BO_3)_2$ nanorods	sol-gel method	-	-	136

magnesium borate nanoparticles	surface-modified method	better tribological capacity in base oil	wear resistance application	137
calcium borate nanoparticles	-	better antiwear property and friction-reducing property in base oil under the novel process	additives in lubricant oils	138
Fe_3BO_6 nanorods	supercooled liquid precursor	-	electrodes, gas sensors, and medical tools	139
calcium borate nanoparticles	modified by oleic acid	significant synergistic effects on tribological properties, and corrosion-inhibiting property	wear resistance application	140
zinc borate nanoflakes	solid-liquid reaction	flame retardant of polyethylene	flame retardant application	141
$Mg_2B_2O_5$ nanorods	solvothermal method at the super-critical conditions	-	-	142
nickel borate nanoparticles	reverse micellar route	antiferromagnetic ordering with Neel temperature of 47 K	magnetic field	143
LiB_3O_5 nanocrystals	mechanical method	UV-induced red shift	optical application	144

Cu^{2+} doped beta-barium borate nanopowder	co-precipitation	Cu^{2+} ions are in a tetragonally distorted octahedral site in the host lattice	optical application	145
$Sr_3Y_2(BO_3)_4$ doped with Eu^{3+} ions	sol-gel Pechini method	photoluminescence properties: red emission with the quantum yield of 54%-55%	phosphor for plasma display panels and luminescent tubes	146
zinc borate/ polypropylene nanocomposites	melt blending method	flammability properties and thermal stability: 38% reduction in the peak heat release rate; a slight increase in the limiting oxygen indices	flame retardant application	147
calcium borate nanoplatelets	one-step precipitation reaction in aqueous solution	an increase in dispensability of oleic acid modified calcium borate in lubrication	lubricant application	148
$Eu(BO_2)_3$ nanowires	direct sintering $Eu(NO_3)_3 \cdot 6H_2O$ and H_3BO_3 with Ag as catalyst	photoluminescence properties: Eu^{3+} orange-red emission at 591 nm	optical application	149
$Al_4B_2O_9$ nanorods	sol-gel method with glucose as the	complex network structures formed in	-	150

	template	aqueous solutions		
lanthanum borate nanoparticles	modified by triethanolamine monooleate	better friction-reducing property in base oil	lubricant application	151
magnesium borate hydroxide nanowhiskers	one step hydrothermal process	optical properties: enhanced absorption in the low-wavelength region; broad emission band with the peak maximum at around 400 nm	optical material	152
zinc borate nanoflakes	coordination homogeneous precipitation method	excellent inflaming retarding effect for polypropylene	flame retardant application	153
MgB_2O_5 nanorods	solvothermal method under supercritical conditions	-	-	154
$Mg_3B_2O_6$ nanorods	solvothermal method under supercritical conditions	-	-	154
$Mg_3B_2O_6$ nanobelts	heating mixed powders of boron and MgO under flowing Ar/H_2O gases at 1100 ^oC	-	-	155
zinc borate	one-step precipitation	the aspect ratios close	thermal	156

nanowhiskers	reaction in aqueous solution	to 10-20; an increase in the thermal stability of polyethylene upon the addition of the nanowhiskers	application	
copper borate nanoparticles	one-step precipitation reaction in aqueous solution	hydrophobic, and the friction coefficients of basic oil decreased with adding the hydrophobic copper borate	lubricant application	157
$Al_4B_2O_9$ nanorods	low-heating-temperature solid-state precursor method	single phase, large surface area, narrow size distribution of 20-30 nm	-	158
zinc borate nanoplatelets	one-step precipitation reaction in aqueous solution	hydrophobic	-	159
zinc borate nanonets	coordination homogeneous precipitation method	better char formation effect	flame-retardant filler	160
$Mg_2B_2O_5$ nanowires	heating the mixed tablet of $Mg(BO_2)_2$ and graphite directly in vacuum at 1200 ^oC	lubricating properties: significantly decrease in the friction coefficient of the oil by the addition of $Mg_2B_2O_5$ nanowires.	lubricant application	161

$Al_{18}B_4O_{33}$ nanowires	spray pyrolysis technique	generation of 3D hollow spherical architectures; good photocatalytic activities	photocatalyst	162
$Mg_2B_2O_5$ nanorods	calcinations of mixed powders containing $Mg(OH)_2$ and H_3BO_3	-	-	163
$Y_{0.9}Er_{0.1}Al_3(BO_3)_4$ nanopowders	sol-gel method	very stable to obtain homogeneous gels and transparent amorphous thin films	integrated optical systems	164
CoB thin films	electroless coating technique	charge/discharge cyclic characteristics	electrical material	65
n-Mg_2B_{14} on p-type Si substrates	laser ablation	electrical property: the neutron signal from a thermal neutron source with 10^5 ns^{-1} cm^{-2} from a spallation beam	solid state heterojunction diode, thermal neutron detector	66
W_2B_5 powders	mechanochemical method	-	-	67
TiB_2	-	reversible hydrogen storage	promote $LiBH_4$-MgH_2 composite	68
HfB_2	in situ reaction and thermal gradient	anti-oxidation and ablation properties	anti-oxidation and ablation	69

	chemical vapor infiltration		material	
Mo_2FeB_2	-	structure stability, magnetism, electronic structure and elastic properties	magnets	70
ZrB_2 nanocrystalline	mechanochemical processing	mechanical properties	hard material	110
tungsten boride	self-propagating high-temperature synthesis	-	-	71
in-situ toughened ZrB_2-TiB_2 ceramic composites	pressureless sintering	the strength at elevated temperatures		72
LaB_6	-	high melting point, high electrical conductivity, low work function and low vapor pressure at high temperature	thermionic materials for high electron density cathodes, filaments of electron microscope	74
FeB/Fe_2B layers	powder-pack boriding method	wear resistance	wear resistance	76
CrB_4	-	temperature-independent paramagnetism and conductivity	magnet	73

Fe_2B layers	powder-pack boriding method	good fracture toughness	nanodevice	80
HoB_{66}	borothermic reduction	low-temperature specific heat, magnetic susceptibility, and thermal expansion	magnetic, thermal material	81
LuB_{66}	borothermic reduction	low-temperature specific heat, magnetic susceptibility, and thermal expansion	magnetic, thermal material	81
nickel boride nanoparticles	sol-gel method	the activity of catalysis in hydrogenation reactions	catalyst	78

1.4 Density functional theory for calculation of elastic properties of nanowires

Density functional theory (DFT) is a quantum mechanical modelling method used in physics and chemistry to investigate the electronic structure (principally the ground state) of many-body systems, in particular atoms, molecules, and the condensed phases. With this theory, the properties of a many-electron system can be determined by using functionals, i.e. functions of another function, which in this case is the spatially dependent electron density. Hence the name density functional theory comes from the use

of functionals of the electron density. DFT is one of the ab initio (or from first principles) methods since it is based only on basic physical laws and is parametrization free in theory, and is among the most popular and versatile methods available in condensed-matter physics, computational physics, and computational chemistry.

For the past 30 years, DFT has been the dominant method for the quantum mechanical simulation of periodic systems. In recent years it has also been adopted by nanomechanic researchers for the simulation of elastic properties of nanowires. Guo and Li[169] elucidated the size dependency of the elastic modulus of ZnO nanowires using the concept of surface stress. Surface stress is defined as the reversible work per unit area required to elastically stretch a surface, while surface energy is the reversible work per unit area required to create a surface. The elastic modulus of a nanowire is proposed to be described in the following form: [168,169]

$$E_n = E_b + \frac{8}{5} g(1-\nu)\frac{L^2}{D^3} \qquad (1\text{-}1)$$

where, E_n and E_b are the elastic modulus of the nanorod and bulk materials, respectively, L and D is the length and diameter of the nanorod, g is the surface stress, and ν is Poisson's ratio. Thus, a positive (tensile) surface stress would lead to an increase in elastic modulus with the decreasing nanowire diameters, while a negative (compressive) surface stress would lead to a decrease in elastic modulus with the decreasing nanorod diameters. The above relation has been shown to be valid for Ag, Pd, and ZnO nanowires.[169] Zhang and Huang[177] found from DFT calculation that the

elastic modulus of ZnO nanoplates with thickness below 3 nm would be higher than those of bulk materials and increase as their size decreases. Guo and Li[178] calculated the bulk and surface properties of the materials using DFT method. The calculated properties include Young's modulus, Poisson's ratio, surface energy, and surface stress. They predicted Young's moduli of Ag, Au, and ZnO nanowires as functions of nanowire diameter.

Although these simulations mentioned above by DFT method are encouraging, they only have determined the elastic properties of a few nanowires, such as Au, Ag, and ZnO. The elastic properties of more nanowires, for example, borate and boride nanomaterials with exceptional mechanical properties, still need to be widely investigated by DFT method.

Our first-principles calculations were performed using the periodic plane wave implementation of density functional theory, VASP.[171,172] We used the projector augmented wave method (PAW) and the GGA-PW91 functional for exchange and correlation. The PAW method is a generalization of the pseudopotential and linear augmented-plane-wave methods, and allows density functional theory calculations to be performed with greater computational efficiency. And GGA-PW91 is one of the popular generalized gradient approximations (GGA) proposed by Perdue and Wang[170]. We chose a kinetic energy cutoff of 600 eV for the plane wave basis sets. In theory all plane waves (with infinite numbers) should be included, but it is practically not viable. So we only keep those important plane waves which have low kinetic energies. Setting the cutoff to

be 600 eV proved to be a fairly good tradeoff between accuracy and efficiency. The energy convergence for all geometry optimization was set to be 1×10^{-5} eV.

CHAPTER 2

Motivation and Research Objectives

2.1 Motivation

From literature review in Chapter 1, although significant advancement in syntheses of low dimentional nanomaterials has been achieved, to the best of our knowledge, only one paper reported the successful production of bulk barium polyborate, $Ba_3B_6O_9(OH)_6$; the $Ba_3B_6O_9(OH)_6$ nanomaterials, SrB_2O_4 nanomaterials and one dimensional ZrB_2 nanostructures have not been investigated in literature. Their nanoscale-enabled properties are completely unknown. Furthermore, there is an urgent need for theory, modeling, simulation and experimental research on the nanoscale to discover to links between the key properties, functionalities and reliabilities of nanomaterials and their size, shape and composition.

2.2 Research objectives

Based on the literature survey and motivation, the objectives of this study are, therefore, to utilize experimental methods to synthesize and probe the intrinsic properties of 1D boron-based nanomaterials:

2.2.1 To synthesize $Ba_3B_6O_9(OH)_6$ nanorods and β-BaB_2O_4 nanospindles, understand the growth mechanism, and investigate the structural, morphological, chemical, thermal, and optical properties of these nanomaterials.

2.2.2 To prepare SrB_2O_4 nanorods, and study the structural, morphological, chemical, mechanical properties of these nanomaterials; to calculate the Young's moduli of bulk SrB_2O_4 and SrB_2O_4 nanorods with consideration of surface stress effect of nanorods by DFT.

2.2.3 To synthesize ZrB_2 nanorods**,** and characterize them in terms of the structural, morphological, chemical, and mechanical properties; To calculate Young's modulus of ZrB_2 nanorods with consideration of surface stress effect of nanorods by DFT.

CHAPTER 3

Low temperature, organic-free synthesis of $Ba_3B_6O_9(OH)_6$ nanorods and β-BaB_2O_4 nanospindles[1]

[1] Rui Li, Xinyong Tao and Xiaodong Li. 2009. *Journal of Materials Chemistry*. 19: 983-987.

Reprinted here with permission of publisher.

3.1 Introduction

One dimensional (1D) metal borate nanomaterials have attracted tremendous attention due to their good chemical inertness, high-temperature stability, excellent mechanical properties, and low thermal expansion coefficient.[9,14,18,19,20,74,91] Barium borate has potential applications in radiation shielding[17], lubricating additives[11] and dielectric devices.[16] It has two crystalline phases with the transition temperature of 925 ^{o}C, namely, high temperature phase α-barium borate and low temperature phase β-barium borate, β-BaB_2O_4 (BBO). Among them, BBO is a well-known nonlinear optical material with a high second-order nonlinear susceptibility (d_{eff} =2.2 pm/V), wide transparency range (189 nm-3500 nm), and high damage threshold.[4,15,23,122] Bulk BBO crystals are generally grown by high temperature methods, such as the modified Kyropoulos and Czochralski techniques.[3,6,8] To date, only a couple of methods have been used to synthesize barium borate nanomaterials. BBO nanoparticles were synthesized via coprecipitation using different bases as precipitants by Zhou *et al.*[84] Network-like BBO nanostructures were produced by a sol-gel method.[87] BBO nanofilms were prepared by sol-gel deposition[12] and metal organic chemical vapor deposition[22]. To date only one paper reported the successful production of bulk barium polyborate, $Ba_3B_6O_9(OH)_6$ (BBOH), which is the first reported chain borate in which the boron atoms are all tetrahedrally coordinated by oxygen atoms.[25] The BBOH nanomaterials, however, have not been reported in literature.

In this chapter, we reported the low temperature, organic-free hydrothermal

synthesis of single crystalline BBOH nanorods. Morever, we found that single crystalline BBO nanospindles can be easily obtained by annealing the BBOH nanorods at a relatively low temperature of 810 ^{o}C. Both BBOH and BBO were transparent from ultraviolet to the visible regions.

3.2 Experimental

All chemicals used in our experiments were purchased and used without further purification. Barium chloride dihydrate ($BaCl_2 \cdot 2H_2O$) was purchased from Alfa. Boric acid (H_3BO_3) and sodium hydroxide (NaOH) were purchased from Fisher.

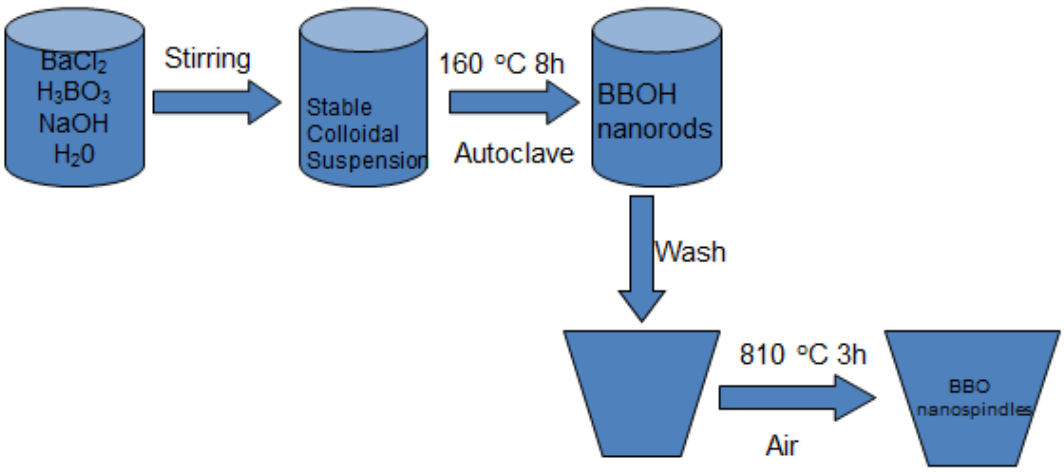

Scheme 3.1 Schematic process of synthesizing the products by hydrothermal method.

In a typical experiment, as shown in Scheme 3.1, 2 mmol of $BaCl_2 \cdot 2H_2O$, 3 mmol of H_3BO_3, and 4 mmol of NaOH were dissolved in 12 ml distilled water under constant magnetic stirring at room temperature. Then, the above suspension was transferred into a 23 ml Teflon-lined stainless steel autoclave. The autoclave was maintained at a fixed temperature of 160 ^{o}C for 8 h without stirring or shaking, and

then was allowed to cool to room temperature naturally. The precipitate was separated by centrifugation, washed with distilled water and absolute ethanol three times, respectively, and then dried at room temperature. The as-prepared powders were placed in a alumina boat and annealed at 810 ^{o}C for 3 h in air .

The products were first analyzed by X-ray diffraction (XRD, Rigaku DMax 2200 using Cu Kα radiation). A few drops of ethanol solution containing the as-prepared products were deposited onto copper grids for transmission electron microscopy (TEM, Hitachi H-8000) and high-resolution transmission electron microscopy (HRTEM, JEOL JEM 2010F) studies. The solvent was then vaporized under ambient conditions. Ultraviolet-visible (UV-vis) absorbance studies were performed using a Beckman Coulter 640 DU spectrophotometer and quartz cuvettes from Starna. Elemental compositions and oxidation states were determined by X-ray photoelectron spectroscopy (XPS), a Kratos Axis Ultra DLD instrument equipped with a monochromated Al Ka X-ray source and hemispherical analyzer capable of an energy resolution of 0.5 eV. Thermogravimetric analysis (TGA) and differential thermal analysis (DTA) were performed using a Thermal Analysis Instruments SDT2960 Thermogravimetric Analyzer, and the sample was scanned at a rate of 20 ^{o}C per minute. Fourier Transform Infrared (FTIR) analysis was performed using a Perkin Elmer Spectrum 100 FTIR spectrometer fitted with a Diamond ATR attachment.

3.3 Results and discussion

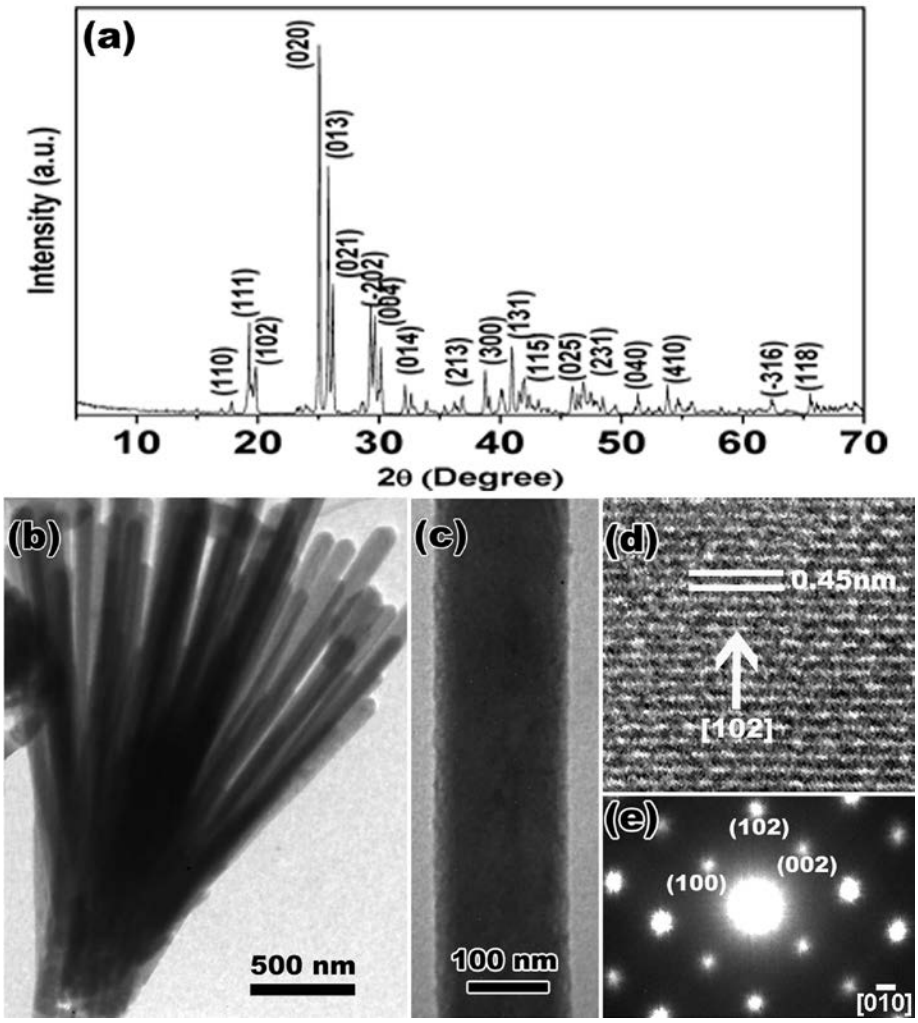

Figure 3.1 (a) XRD pattern of the sample synthesized via hydrothermal at 160℃ for 8 h, (b) low magnification TEM image, (c) high magnification TEM image, (d) HRTEM image, and (e) corresponding SAED pattern of BBOH nanorods.

Figure 3.1a shows a representative XRD pattern of the sample synthesized via hydrothermal method at 160 ^{o}C for 8 h. All the peaks can be readily indexed to the monoclinic phase of BBOH (JCPDS file, no.01-071-2501), with lattice constants of a= 6.99, b= 7.14 and c = 11.92 Å, and space group of $P2/c$. No impurity peaks were

observed. The low and high magnification TEM images (Figure 3.1b and 3.1c) show that the synthesized BBOH exhibits rod-lik morphology with an average diameter of 115 nm and length ranging from 1 to 3 μm. The representative HRTEM image (Figure 3.1d) and corresponding selected area electron diffraction (SAED) pattern (Figure 3.1e) at the zone axis of $[0\bar{1}0]$ jointly indicate that the synthesized BBOH nanorods are single crystals with the growth orientation along the [102] direction. No defects such as dislocations and twins were found. The measured distance between the lattice fringes for the (102) planes is 0.45 nm.

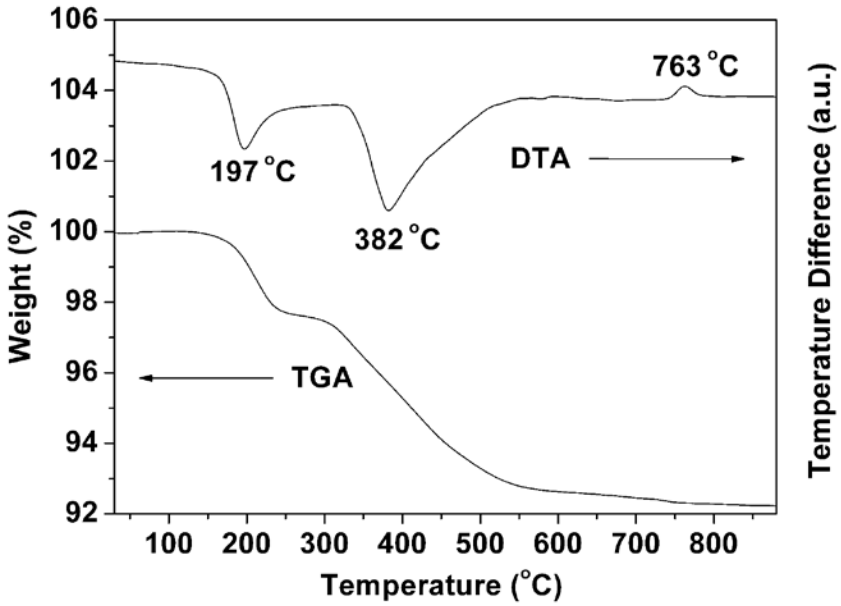

Figure 3.2 TGA and DTA curves of BBOH nanorods.

For the BBOH nanorods, the weight loss was found to be about 7.6% in the range of 100-600 ^{o}C when heated in air (Figure 3.2), in good agreement with the weight loss from the removal of the adsorbed water molecules and the hydroxyl groups. Analysis of the

TGA curve (Figure 3.2) reveals that the weight loss occured in two stages, as in the case for some reported borate hydrates.[90] The first stage is in the temperature range of 125-240 ^{o}C with the weight loss 2.6% and the second stage proceeds in the range of 300-600 ^{o}C with the weight loss 5.0%. These two weight loss stages agree well with the two endothermic effects at about 197 ^{o}C and 382 ^{o}C in the DTA curve (Figure 3.2), which are 57 ^{o}C and 32 ^{o}C higher than those of the bulk BBOH, respectively.[25] The exothermic effect at about 763 ^{o}C can be attributed to the crystallization of the BBO crystals, which will be discussed in the following paragraphs.

Figure 3.3a shows the XRD pattern of the product obtained after annealing the BBOH nanorods at 810 ^{o}C for 3 h in air. All the peaks can be readily indexed to the hexagonal phase of BBO (JCPDS file, no.80-1489), with lattice constants of a=12.53, c=12.73 Å and space group of *R3c*. The TEM images (Figure 3.3b and 3.3c) reveal that the obtained BBO exhibits spindle-like morphology with an average length of 600 nm and width ranging from 35 to 60 nm in the widest section. The HRTEM image and SAED pattern (Figure 3.3d) at the zone axis of $[\bar{1}10]$ further reveal that the BBO nanospindles are single crystals with the growth orientation of the [113] direction. No defects such as dislocations and twins were found. The measured distance between the lattice fringes for the (113) planes is 0.35 nm.

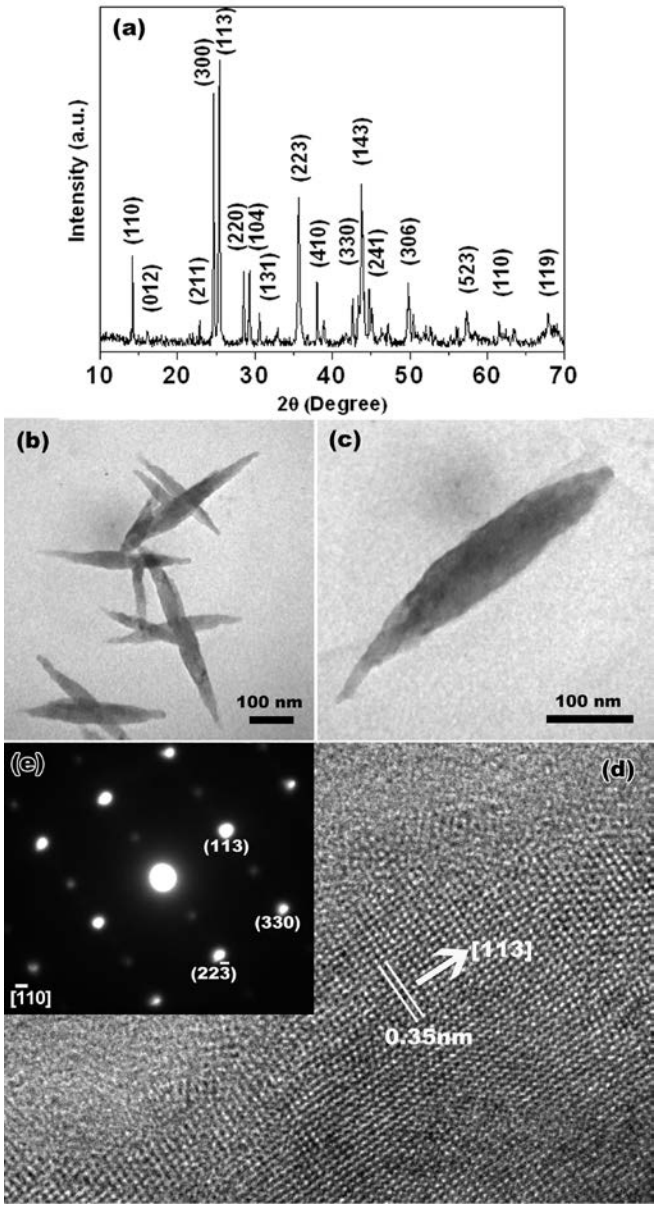

Figure 3.3 (a) XRD pattern, (b) low magnification TEM, (c) high magnification TEM, (d) HRTEM, and (e) corresponding SAED pattern of BBO nanospindles.

XPS analysis was carried out to further characterize the BBOH nanorods and BBO nanospindles (Figure 3.4). The binding energies were corrected by taking C 1s core level at 284.8 eV for the two samples. Both survey spectra, as shown in Figure 3.4a, exhibit Ba 3p, Ba 3d, Ba 4d, Ba 4p, B 1s, O 1s and C 1s core levels, and Ba MNN Auger peak. In

Figure 3.4b, the peaks at 779.8 eV and 795.1 eV in the BBOH curve and the peaks at 780.1 eV and 795.4 eV in the BBO curve can be attributed to Ba $3d_{5/2}$ and Ba $3d_{3/2}$, respectively. B 1s and Ba $4p_{1/2}$ peaks overlapped in the survey spectra, and XPSPEAK software (Version 4.1) was used to fit this overlapped peak with two components, *i. e.*, B 1s and Ba $4p_{1/2}$ peaks. In Figure 3.4c, the peak at 191.7 eV in the BBOH curve and the peak at 191.9 eV in the BBO curve correspond to B 1s core level. The binding energies of Ba 3d and B 1s of BBO are 0.3 eV and 0.2 eV greater than

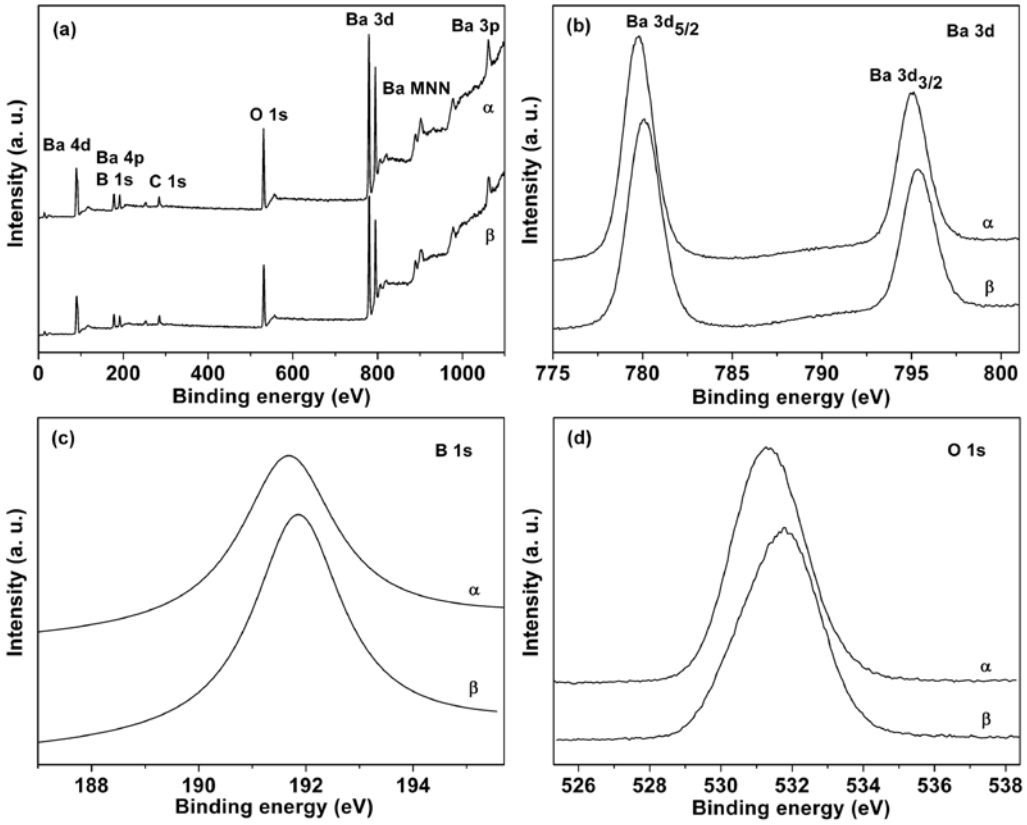

Figure 3.4 XPS spectra of (α) BBOH nanorods and (β) BBO nanospindles. (a) Survey spectra, (b), (c), and (d), detailed spectra of Ba 3d, B 1s and O 1s core levels, respectively.

those of BBOH, respectively, due to the different chemical structures of these two

materials. In Figure 3.4d, the O 1s peaks at 531.27 eV in the BBOH curve and at 531.8 eV in the BBO curve suggest that the oxygen exists as O^{2-} species in the BBOH nanorods and BBO nanospindles. These results for BBO nanospindles are in good agreement with the values for crystalline BBO reported in literature.[2,87]

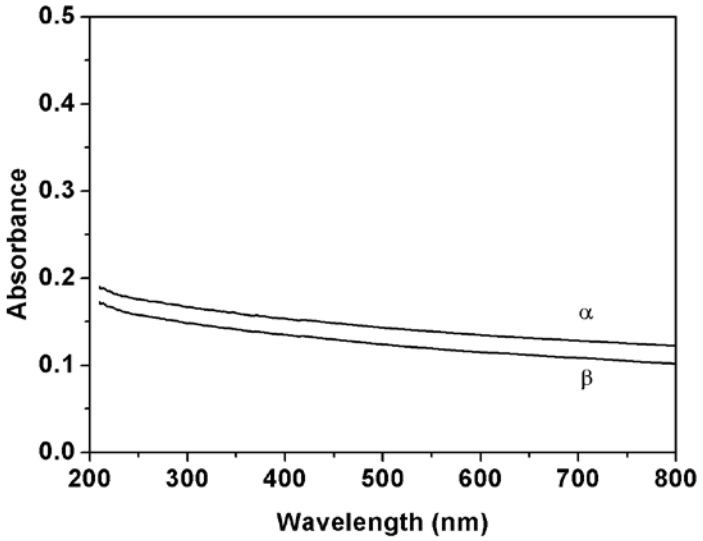

Figure 3.5 UV-vis absorption spectra of (α) BBOH nanorods and (β) BBO nanospindles.

Figure 3.5 shows the UV-vis absorption spectra of BBOH nanorods and BBO nanospindles. It can be seen that both BBOH and BBO are transparent up to 210 nm (5.90 eV) within the limitation of instrument whose working range is 210-790 nm. The absorption spectra are relatively featureless, and the broad and overall constant low absorbance from 210 to 790 nm is consistent with the reported values for bulk BBO single crystals[24] and network-like nanomaterials[87], thus demonstrating that it is transparent from ultraviolet to the visible regions.

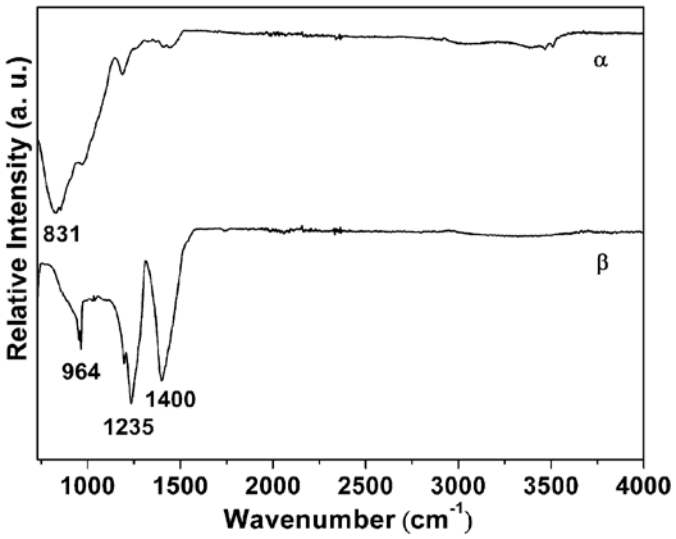

Figure 3.6 FTIR spectra of (α) BBOH nanorods and (β) BBO nanospindles.

Figure 3.6 shows the FTIR spectra of the BBOH nanorods and BBO nanospindles. The BBOH nanorods show an absorption in the range of 4000-2700 cm^{-1}, indicating the presence of hydroxyl groups. The broad strong bands observed close to 831 cm^{-1} are due to the vibrations of tetrahedral $(BO_4)^{5-}$ groups, that are the basic units of the BBOH structure.[25] The FTIR spectrum of the BBO nanospindles exhibits broad absorptions in the 900-1500 cm^{-1} range. The absorption peak at 1235 cm^{-1} results from the B-O stretching in the BO_3^{3-} unit, which is a component of the $(B_3O_6)^{3-}$ ring. The peaks observed at 964 and 1400 cm^{-1} are attributed to B-O extra-ring stretching.[89] The detailed FTIR analyses suggest that the BBO nanospindles have the characteristics of bulk BBO crystals.

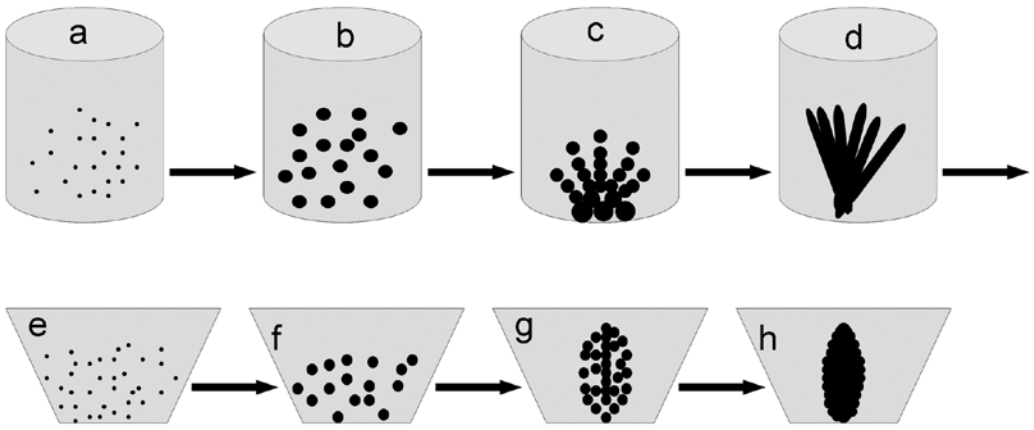

Figure 3.7 Schematic diagram showing the growth processes of BBOH nanorods in the autoclave (a-d) and BBO nanospindles in the alumina boat (e-h).

Based on the above experimental results, the formation mechanisms of the BBOH nanorods and BBO nanospindles are proposed. The whole process, which is described in the following reactions,

$$3\ Ba^{2+} + 6\ H_3BO_3 + 6\ OH^- = Ba_3B_6O_9(OH)_6\downarrow + 9\ H_2O \qquad (3\text{-}1)$$

$$Ba_3B_6O_9(OH)_6 = 3\ BaB_2O_4 + 3\ H_2O\uparrow \qquad (3\text{-}2)$$

can be schematically illustrated in Figure 3.7. Flocculent precipitates, as we observed in the experiments, were formed immediately after solving the reactants in the aqueous solution under intensive stirring. This suspension was transferred into a 23 ml Teflon-lined stainless steel autoclave. The autoclave was maintained at a fixed temperature of 160 ^{o}C for 8 h without stirring or shaking. First, as shown in Figure 3.7a, nuclei were formed from the flocculent precipitates in the suspension under hydrothermal conditions.[10,121] Second, the nuclei grew by consuming the ambient raw materials (Figure 3.7b). Third, the larger nanoparticles fell down to the bottom of the

autoclave and began to aggregate most probably by electrostatic gravitation and intermolecular force (Figure 3.7c). The smaller ones were attached to the aggregate and extended in a certain way because the anisotropic growth of the nanocrystals in a template-free method is generally related to the different surface energy of different crystal planes of the nanocrystals. Those planes with high surface energy have a strong tendency to capture smaller nanoparticles from the reaction solution in order to reduce their surface energy.[10,121] This leads to growth along those planes and formation of the 1D BBOH nanorod bundles in Figure 3.7d. After ultrasonic treatment BBOH nanorods were obtained.

To prepare the BBO nanomaterials, the as-prepared BBOH nanorods were annealed at 810 ^{o}C for 3 h in air. The BBOH nanorods contain water in the form of both hydroxyl ion and adsorbed water molecules. This allows one to rationalize a complex process of dehydration of borates at elevated temperatures which involves elimination of individual adsorbed water molecules and hydroxyl groups, due to association of boron-containing anions (see TGA and DTA curves in Figure 3.2). Dehydration of borates is accompanied by a specific effect of borate rearrangement[5], namely, dehydration causes a complete destruction of the crystal lattice and transition of the BBOH nanorods into the amorphous state; further heating leads to crystallization including the nucleation and growth processes as solid-state reaction. First, in Figure 3.7e, nuclei were formed from amorphous solid under heat-treatment conditions. Second, the nuclei grew by consuming the ambient amorphous solid (Figure 3.7f).

Third, in Figure 3.7g, the nanoparticles aggregated in a certain way driven likely by electrostatic attraction and intermolecular force. Finally single crystal BBO nanospindles were formed (Figure 3.7h).

Spindle-shaped nanostructures have great potential applications in field of optics,[7,21,27] the detailed optical and optoelectronic properties will be studied further in future. The mechanical properties of BBOH nanorods and BBO nanospindles also lack and will be investigated.

3.4 Conclusions

Barium polyborate BBOH nanorods were synthesized via a low temperature, organic-free hydrothermal route. These nanorods can be easily transformed into BBO nanospindles through heat treatment at 810 ^{o}C for 3 h. Both BBOH nanorods and BBO nanospindles are transparent from ultraviolet to the visible regions.

CHAPTER 4

Synthesis, structural, optical and mechanical characterization of SrB_2O_4 nanorods[2]

[2] Rui Li, Lihong Bao and Xiaodong Li. 2011. *CrystEngComm*. 13: 5858-5862. Reprinted here with permission of publisher.

4.1 Introduction

One dimensional (1D) metal borate nanostructures have attracted tremendous attention due to their outstanding chemical inertness, high temperature stability, excellent mechanical properties, and low thermal expansion coefficient.[20,84-100] As an important type of optical materials,[92] strontium borates have shown various promising applications in high pressure sensors,[93] magnetooptical media,[94] ultraviolet (UV) phosphors,[95] and detectors for thermoluminescent dosimetry.[96] Guided by the SrO-B_2O_3 phase diagram,[97] five bulk strontium borate materials have been synthesized, which are $Sr_3B_2O_6$, $Sr_2B_2O_5$, SrB_2O_4, SrB_4O_7, and $Sr_2B_{16}O_{26}$.[98] The representative synthesis techniques include solid state reactions between strontium oxide and boric acid and hydrothermal method. However, to our knowledge, strontium borate nanostructures are still absent in literature and their nanoscale-enabled properties are completely unknown.

In our previous work, 1D nanostructures of magnesium borate,[20] aluminum borate,[85] barium borate,[86] and calcium borate[28] have been successfully synthesized. These borate nanostructures exhibit superior mechanical properties. However, the mechanical properties of strontium borates are rarely reported, even for the bulk materials. On the other hand, the optical properties of strontium borate nanostructures have not been explored or theoretically predicted. In this chapter, we report the synthesis, structural, optical and mechanical characterization of SrB_2O_4 nanorods. Single crystalline SrB_2O_4 nanorods were synthesized for the first time via a sol-gel

route at a relatively low temperature of 800 °C. The X-ray diffraction (XRD) analysis revealed that the as-synthesized nanorods have an orthorhombic phase of SrB_2O_4 with lattice constants of *a*= 12.01, *b*= 4.34 and *c* = 6.59 Å, and space group of *Pbcn* (JCPDS#84-2175). The high-resolution transmission electron microscopy (HRTEM) characterization showed that individual SrB_2O_4 nanorods are single crystals with the growth direction along the [511] orientation. The ultraviolet-visible (UV-vis) absorption spectroscopy study unveiled that the SrB_2O_4 nanorods are transparent from the ultraviolet to the visible regimes. Atomic force microscopy (AFM) three-point bending tests were performed directly on individual nanorods to probe their mechanical properties. The elastic modulus of the SrB_2O_4 nanorods was measured to be 158.2 ± 7.9 GPa. Such structural, optical and mechanical information provides design guidelines for developing SrB_2O_4 nanostructure-based nanodevices and nanocomposites, and lays a constitutive foundation for modeling the nanostructures of strontium borates and other borate nanostructures.

4.2 Experimental

All chemicals used in our experiments were purchased and used without any further purification. Strontium chloride dehydrate ($SrCl_2 \cdot 2H_2O$) was purchased from Alfa Aesar. Sodium borohydride ($NaBH_4$) and cetyltrimethylammonium bromide (CTAB) were purchased from Sigma Aldrich.

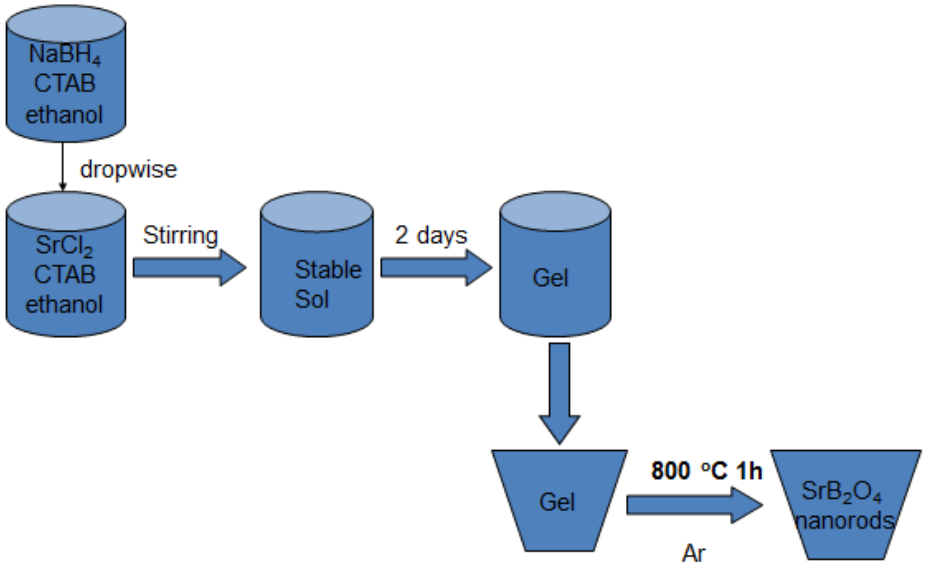

Scheme 4.1 Schematic process of synthesizing the products by sol-gel method.

In a typical experiment, shown in Scheme 4.1, 1 mmol of $SrCl_2 \cdot 2H_2O$ and 1.5 mmol CTAB, and 6 mmol of $NaBH_4$ and 1 mmol CTAB were separately dissolved in 12 ml distilled water with constant magnetic stirring at room temperature. Then the $NaBH_4$ solution was added dropwise to the $SrCl_2$ solution in 2 minutes. The reaction mixture was stirred for half an hour, and then stored in air at room temperature without stirring or shaking, and after 48 h a white gel was formed. The as-prepared precursors were placed in an alumina boat and annealed at 800 ^oC for 1 h in Ar. The white products were washed with distilled water and absolute ethanol three times, respectively, and dried at room temperature.

The chemical process for synthesizing SrB_2O_4 nanorods can be described in the following reaction:

$$SrCl_2 \cdot 2H_2O + 2\ NaBH_4 + 2\ H_2O = SrB_2O_4 + 2\ NaCl + 8\ H_2 \uparrow \qquad (4\text{-}1)$$

The crystal structure of the products was characterized by XRD (Rigaku DMax 2200 using Cu K_α radiation). A few drops of ethanol solution containing the as-prepared products were deposited onto copper grids for transmission electron microscopy (TEM, Hitachi H-8000), and HRTEM (JEOL JEM 2010F) analyses. The solvent was then vaporized under ambient conditions. The resulting product was collected for characterization by scanning electron microscopy (SEM, Zeiss Ultra Plus FESEM). UV-vis absorbance spectrum of the as-prepare products was obtained using a Beckman Coulter 640 DU spectrophotometer and quartz cuvettes from Starna. Chemical compositions and oxidation states of the products were determined by X-ray photoelectron spectroscopy (XPS, a Kratos Axis Ultra DLD instrument equipped with a monochromated Al Ka x-ray source and hemispherical analyzer capable of an energy resolution of 0.5 eV). Thermogravimetric analysis (TGA) and differential thermal analysis (DTA) were carried out using a Thermal Analysis Instruments SDT2960 Thermogravimetric Analyzer with a scan rate of 20 ^oC per minute. Fourier transform infrared (FTIR) analysis was performed using a Perkin Elmer Spectrum 100 FTIR spectrometer fitted with a Diamond ATR attachment. Nanoscale three-point bending tests were performed directly on individual nanorods to probe their mechanical properties using AFM. To avoid sliding during the bending tests, both ends of the nanorods, which bridged over the trench, were clamped by electron beam induced deposition (EBID) of

paraffin in SEM (FEI Quanta 200).[99,100,101] This carbonaceous material thin layer and the strong adhesion force between the nanorod and the edges of the trench insured the fully clamping of the both ends of the suspended SrB_2O_4 nanorod during the bending tests, and thus the suspended SrB_2O_4 nanorod can be treated as a double clamped beam.

4.3 Calculation methods

Our first-principles calculations were performed using the density functional theory implementation, VASP. [171,172] We used the projector augmented wave method and the GGA-PW91 functional for exchange and correlation. We chose a kinetic energy cutoff of 600 eV to expand the electronic wave functions in the plane wave basis. The energy convergence for all geometry optimization was set to be 1×10^{-5} eV.

4.3.1 Bulk materials

Bulk SrB_2O_4 has an orthorhombic structure (space group: Pbcn) with experimental lattice constants of a = 12.014 Å, b = 4.339 Å and c = 6.586 Å. Using a 5×12×8 k-point mesh for k space integration, we have optimized the lattice constants of $SrBO_4$ and calculated the elastic constants of it following the procedure in reference 167.

4.3.2 Nanoscale materials

For the SrB_2O_4 (001) surface calculations, we have used a supercell with 2 layers (8 Sr atoms, 16 B atoms and 32 O atoms) and a vacuum of 15 Å, and employed a 5×12×1 k-point grid for all the subsequent calculations. We deformed the surface along the (100) direction by strains of ε in the range of [-0.02, 0.02] with an interval of 0.005.

4.4 Results and discussion

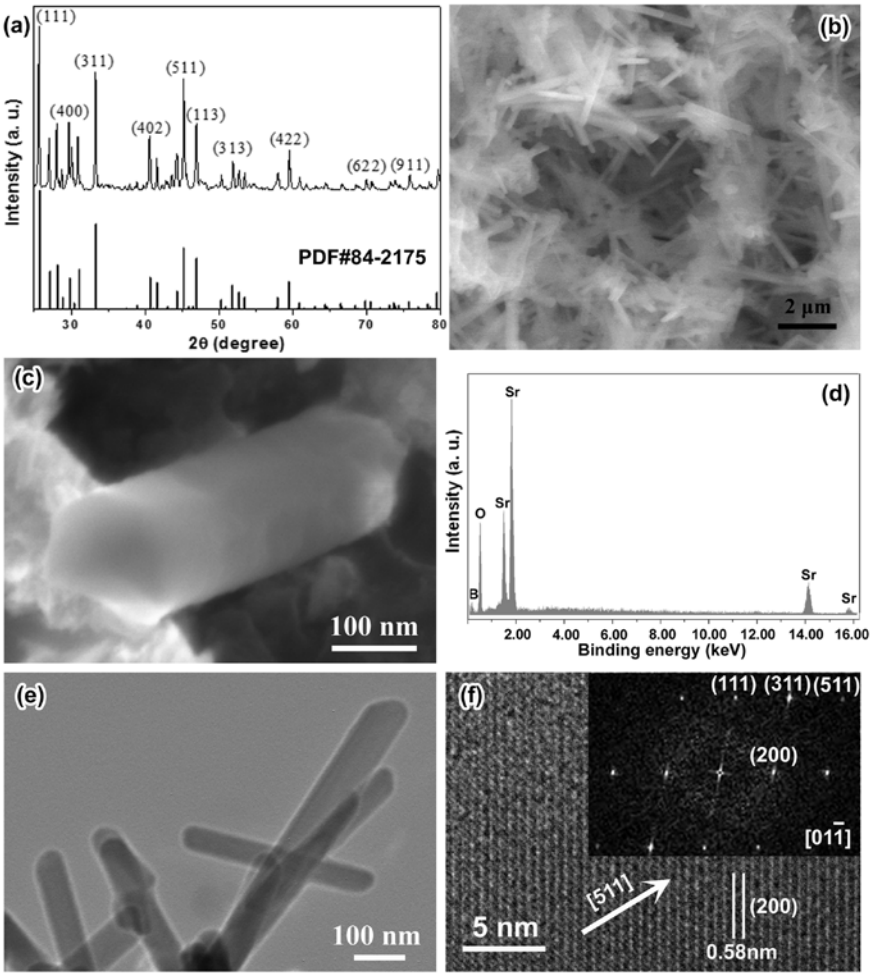

Figure 4.1 (a) XRD pattern and the corresponding JCPDS standard （PDF#84-2175） (b, c) SEM images, (d) EDS spectrum, (e) TEM image, (f) HRTEM image and (inset) corresponding FFT pattern of SrB_2O_4 nanorods.

Figure 4.1a shows a representative XRD spectrum of the product synthesized via the sol-gel method at 800 ^oC for 1 h. All the peaks can be readily indexed to the orthorhombic phase of SrB_2O_4 (JCPDS file, No. 84-2175, with lattice constants of a= 12.01, b= 4.34 and c = 6.59 Å, and space group of *Pbcn*). No impurity peaks were observed, indicating high purity of the product. The SEM image of the product shown

in Figure 4.1b reveals that the product is composed of SrB_2O_4 nanorods with an average diameter of 80 nm and length ranging from 1 to 3 μm. High-magnification SEM image shows that the SrB_2O_4 nanorods have a circle-like cross-section (Figure 4.1c). The energy dispersive spectroscopy (EDS, Figure 4.1d) pattern of the SrB_2O_4 nanorods indicates that the nanorods contain Sr, B and O with the atomic ratio of 18.5: 29.5: 52.0, which is comparable to that obtained by XRD. The TEM image (Figure 4.1e) shows that the SrB_2O_4 nanorods have very smooth surfaces and the average diameter and length of the nanorod are consistent with the SEM results. The representative HRTEM image (Figure 4.1f) and corresponding fast-Fourier transform (FFT) pattern at the zone axis of $[01\bar{1}]$ jointly suggest that the synthesized SrB_2O_4 nanorods are single crystals with the growth direction along the [511] orientation, which is consistent with the stronger diffraction intensity of (511) in the XRD pattern in comparison with the standard XRD pattern in Figure 4.1a. No defects such as dislocations and twins were found in individual SrB_2O_4 nanorods. The measured distance between the lattice fringes for the (200) planes is 0.58 nm, in good agreement with the XRD results.

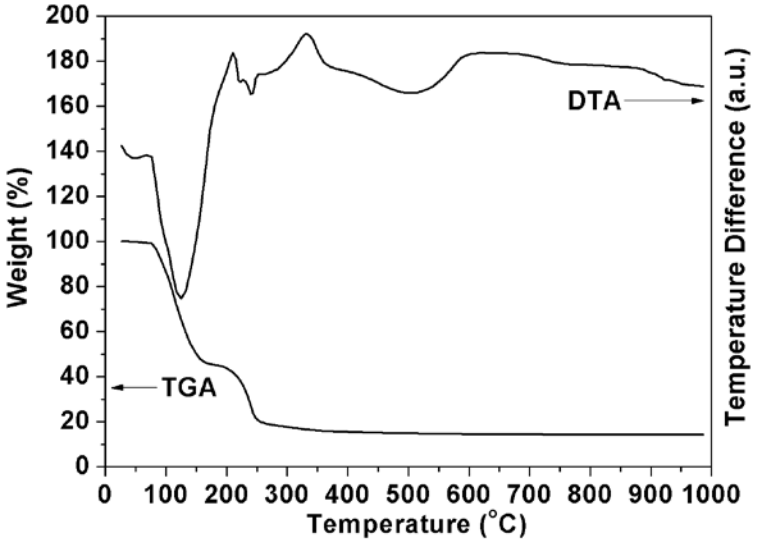

Figure 4.2 TGA and DTA curves of the precursor.

To investigate the growth process of the SrB_2O_4 nanorods from originating precursor (the white color gel obtained from the reaction mixture without heat treatment), both TGA and DTA were performed, as is shown in Figure 4.2. For the precursor, the weight loss was found to be about 82.3% in the range of 25-300 ^oC when heated in air, in good agreement with the weight loss from the removal of the adsorbed water molecules and the organic groups. Detailed analysis of the TGA curve (Figure 4.2) reveals that the weight loss process occurred in two stages, the same as the thermal chemistry process of the reported hydrated borate.[4,5] As determined by EDS, the white color gel (precursor) contains Sr, B, O, C, Na, Cl and Br elements. The contents of C and O reach upto 70 wt%, which indicates that the first stage is related to the removal of the adsorbed water molecules and the hydroxyl groups in the temperature range of 76-180 ^oC with a weight loss of 55.7%, and the second stage is ascribed to the decomposition of the organic

components in the range of 200-300 ^{o}C with a weight loss of 26.1%. These two weight loss stages agree well with the two endothermic effects at about 125 ^{o}C and 240 ^{o}C in the DTA curve (Figure 4.2). The exothermic effect at about 600-870 ^{o}C can be attributed to the crystallization of the SrB_2O_4 crystals.

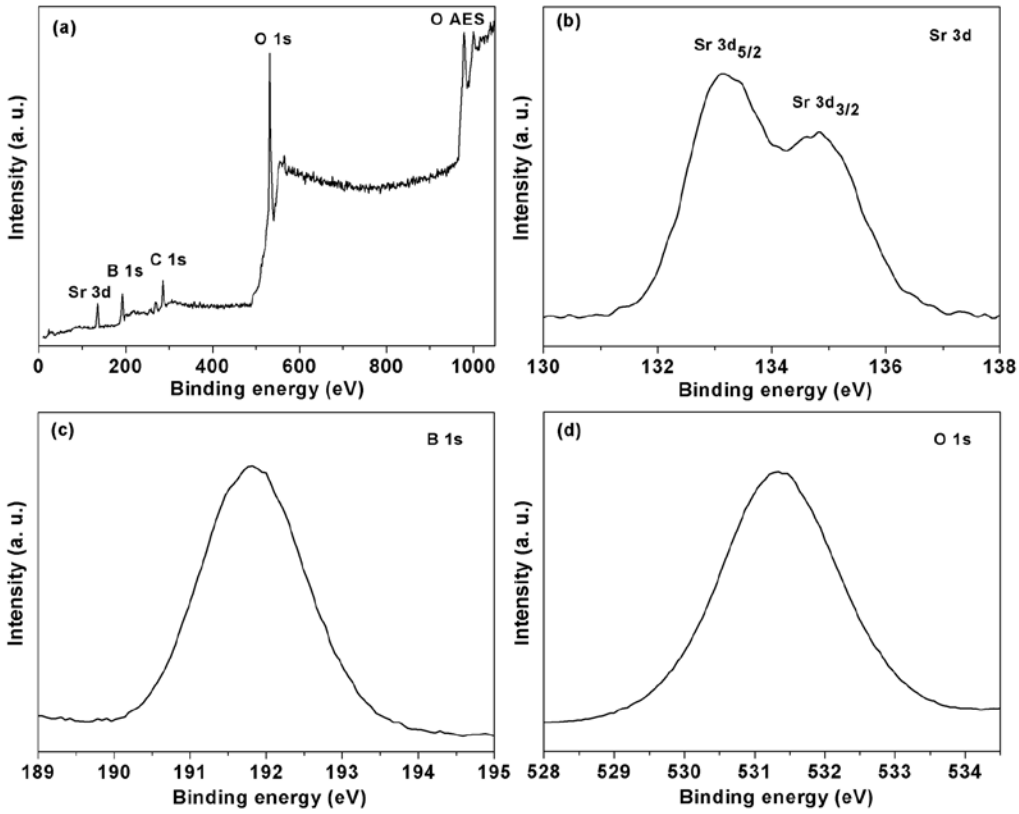

Figure 4.3 XPS spectra of SrB_2O_4 nanorods. (a) Survey spectrum, (b), (c), and (d), detailed spectra of Sr 3d, B 1s and O 1s core levels, respectively.

XPS analysis was carried out to further characterize chemical compositions of the SrB_2O_4 nanorods (Figure 4.3). The binding energies were corrected by taking C 1s at 284.8 eV. The survey spectrum, as shown in Figure 4.3a, exhibits Sr 3d, B 1s, O 1s and C

1s core levels, and O Auger peak. In Figure 4.3b, the peaks at 133.2 eV and 134.8 eV in the curve can be attributed to Sr $3d_{5/2}$ and Sr $3d_{3/2}$, respectively. In Figure 4.3c, the peak at 191.8 eV can be assigned to B 1s core level. In Figure 4.3d, the O 1s peak at 531.3 eV suggests that the oxygen exists as O^{2-} species in the SrB_2O_4 nanorods. The XPS results for the SrB_2O_4 nanorods are in good agreement with the reported values for bulk borates.[86,104]

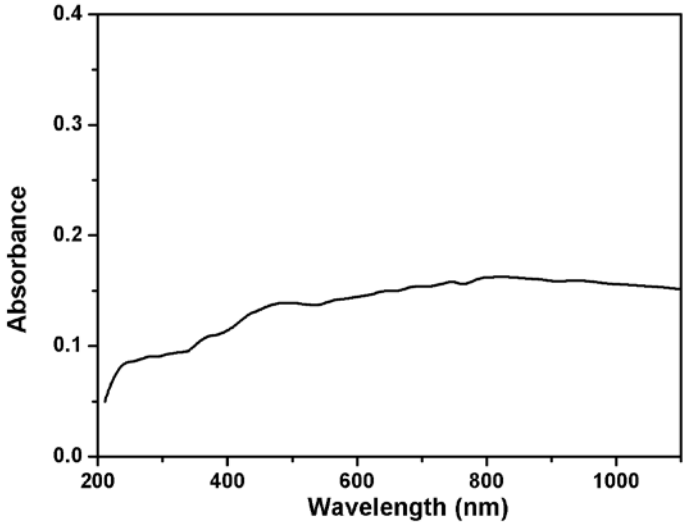

Figure 4.4 UV-vis absorption spectrum of SrB_2O_4 nanorods.

Figure 4.4 shows the UV-vis absorption spectrum of SrB_2O_4 nanorods. It can be seen that the SrB_2O_4 nanorods are transparent from 200 nm (5.90 eV) to 1100 nm within the limitation of the instrument, whose working range is 200-1100 nm. The absorption spectrum is relatively featureless, and the broad and overall constant low absorbance from 200 to 1100 nm, including the nearly no absorbance from 200 to 300 nm, is consistent with the reported values for bulk SrB_2O_4 single crystals,[6]

demonstrating that the SrB_2O_4 nanorods are transparent from the ultraviolet to the visible regimes. This transparent cahracter indicates that the SrB_2O_4 nanorods is very useful for the optical window application.

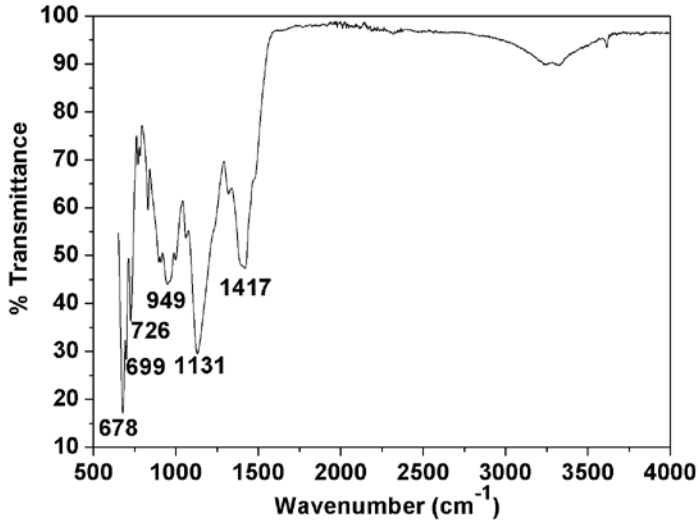

Figure 4.5 FTIR spectrum of SrB_2O_4 nanorods.

Figure 4.5 shows the FTIR spectrum of the SrB_2O_4 nanorods. The spectrum exhibits broad absorptions in the 650-1600 cm^{-1} range. Detailed FTIR analysis suggests that the SrB_2O_4 nanorods have all characteristics of bulk SrB_2O_4 crystals. The peak observed at 949 cm^{-1} are attributed to B-O extra-ring stretching.[7] The bands at about 897 cm^{-1} are due to the BO_3 symmetric stretching modes. The band at 1417 cm^{-1} is due to the asymmetric stretching vibration of the group BO_3. The band at 1131 cm^{-1} is assigned to the in-plane bending of the group BO_3. The bands observed at 726, 699, and 678 cm^{-1} are due to the out-of-plane bending mode of the group BO_3. The FTIR spectrum confirms the existence of the trigonally coordinated boron atoms,

consistent with the crystallographic study.[106]

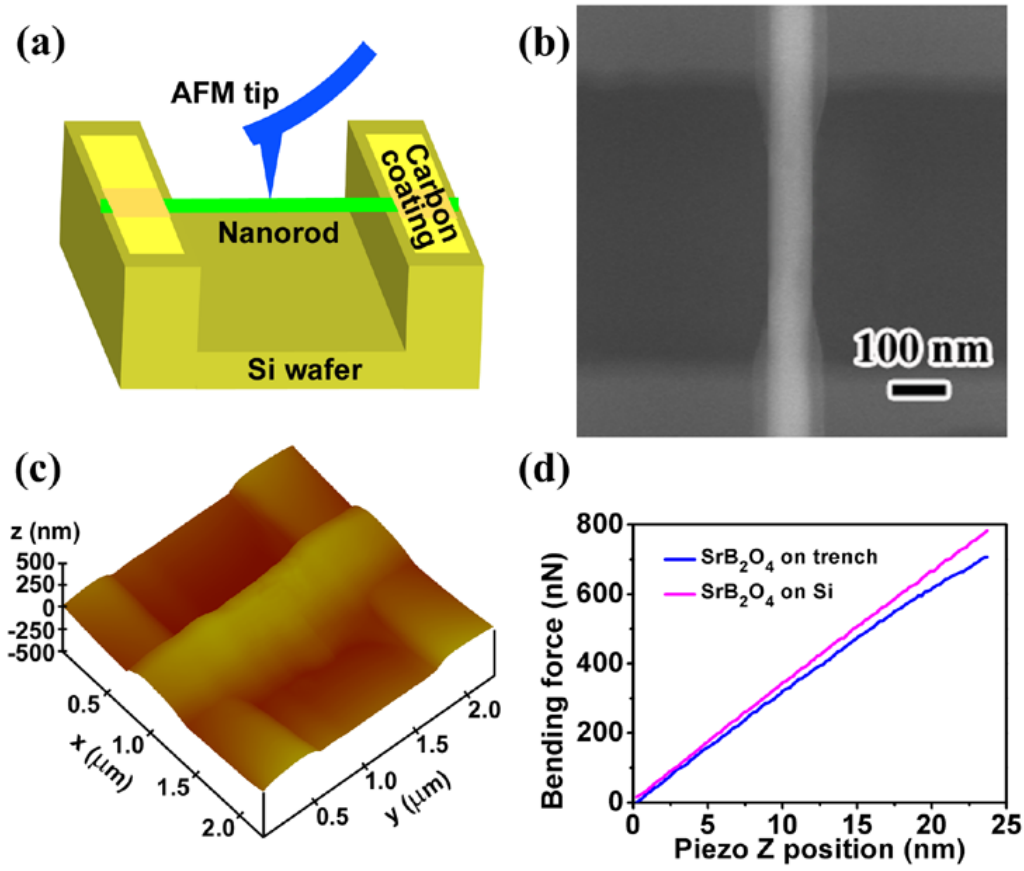

Figure 4.6 AFM three-point bending test on an individual SrB_2O_4 nanorod. (a) Schematic image of an EBID-fixed SrB_2O_4 nanorod in a three-point bending test with an AFM tip. (b) SEM and (c) AFM images of a fixed SrB_2O_4 nanorod suspended over the trench. (d) Representative bending force-piezo position (F-Z) curves of the SrB_2O_4 nanorod directly sitting on Si wafer and the SrB_2O_4 nanorod bridging a trench with both ends of the nanorod fixed.

Nanoscale three-point bending tests[100,107] were performed directly on individual SrB_2O_4 nanorods to probe their mechanical properties (Figure 4.6a). To avoid sliding during the bending tests, both ends of the nanorod, which bridged the trench, were clamped by EBID of paraffin.[99,101] Figure 4.6b and 6c are representative SEM and

AFM images of an EBID-fixed nanorod, respectively. Figure 4.6d shows representative force–piezo position (F-Z) curves obtained along the Z-direction on the nanorod directly sitting on a Si wafer and the suspended nanorod, respectively. The F-Z curves exhibit a strong linear relationship up to 450 nN. On the basis of elastic beam-bending theory, the elastic modulus of SrB_2O_4 nanorods, E_n, can be calculated from the equation:[107]

$$E_n = \frac{FL^3}{192 d_n I} = \frac{k_n L^3}{192 I} \quad (4\text{-}2)$$

where I is the moment of inertia. For a circle-shaped nanorod, $I = \pi r^4/4$, where r is the radius of the nanorod. L is the suspended length of the nanorod and F is the applied load at its mid-point position. k_n ($=F/d_n$) is the spring constant of the nanorod, and can be obtained from the equation:[107]

$$k_n = \frac{k_1 k_2}{k_1 - k_2} \quad (4\text{-}3)$$

where k_1 and k_2 are the slopes of the F-Z curves for the SrB_2O_4 directly sitting on the Si wafer and the suspended SrB_2O_4 nanorod, as shown in Figure 6d, respectively. The average elastic modulus for the SrB_2O_4 nanorods was measured to be 158.2 ± 7.9 GPa. The mechanical properties of strontium borates have been rarely reported, even for the bulk materials. This is the first time to report the mechanical properties of strontium borates. Our SrB_2O_4 nanorods achieved 25.0%, 25.8%, 30.7%, and 53.9% increase in elastic modulus compared with $Ca_2B_2O_5 \cdot H_2O$ nanobelts,[28] $Mg_2B_2O_5$ nanowires,[20]

$Al_{18}B_4O_{33}$ nanowires, and $Al_4B_2O_9$ nanowires,[85] respectively. The observed elastic modulus is also 1.8%, 60.8% increase compared with bulk borates: $Mg_2B_2O_5$,[20] $Ca_2B_2O_5$,[108] respectively; 60.5% decrease compared with bulk $Al_{18}B_4O_{33}$.[109] These findings are significant for designing strontium borate nanostructure-based nanocomposites and nanodevices, and lay a constitutive foundation for modeling the nanostructures of strontium borates and other borate nanostructures.

In this study, we elucidate the size dependency of the elastic modulus (Young's modulus) of SrB_2O_4 nanorods using the concept of surface stress. Surface stress is defined as the reversible work per unit area required to elastically stretch a surface, while surface energy is the reversible work per unit area required to create a surface.[169] In Ref. 168 and 169, the elastic modulus of a nanowire is proposed to be described in the following model:

$$E_n = E_b + \frac{8}{5} g(1-\nu)\frac{L^2}{D^3} \qquad (4\text{-}4)$$

where, E_n and E_b are the elastic modulus of the nanorod and bulk materials, respectively, L and D is the length and diameter of the nanorod, g is the surface stress, and ν is Poisson's ratio. Thus, a positive (tensile) surface stress would lead to an increase in elastic modulus with the decreasing nanowire diameters, while a negative (compressive) surface stress would lead to a decrease in elastic modulus with the decreasing nanorod diameters. The above relation has been shown to be valid for Ag, Pd, and ZnO nanowires.[169] Although these results are encouraging, it has determined the elastic

properties of nanowires by neglecting the experimentally relevant point that different loading methods (tension, bending, or resonance) may yield different elastic properties of nanowires. For example, differences may emerge in nanoscale tension and bending tests because the surfaces of the nanowire carry the most stress during flexural motion. This hypothesis has been confirmed by the atomistic studies of Miller and Shenoy.[175] They found differences in nanowire (thickness of 5 nm) elastic properties under bending and tension. McDowell *et al*.[176] found that the effects of loading method on elastic modulus become significant only in wires with cross-sectional thicknesses below about 5 nm, which is significantly smaller than our experimental size range. Our first-principles calculations for SrB_2O_4 nanorods were performed using the VASP code.[171,172] We used the projector augmented wave method and the generalized gradient approximation of Perdew and Wang[170] for exchange and correlation. We chose a kinetic energy cutoff of 600 eV to expand the electronic wave functions in the plane wave basis. The energy convergence for all geometry optimization was set to be 1×10^{-5} eV.

For using Equation 4-4, we have to know the elastic modulus and Poisson's ratio of bulk SrB_2O_4. Elastic modulus and elastic constants for most pure metals are available over a wide range of temperature in literature. In contrast, data for borate compounds are much more limited. In particular, single crystal elastic modulus and elastic constants, which are required in the basic studies of materials science, are not available except for a few borate compounds. Efforts have been made to calculate the elastic constants theoretically from so-called first principles calculations and, although the bulk modulus

has been calculated for various materials, calculations of elastic constants for SrB_2O_4 have not been reported. Therefore, in literature, there is not any experimental or calculational information about the elastic modulus of bulk SrB_2O_4. This motivated us to calculate all nine independent elastic constants and related properties of SrB_2O_4 from first principle electronic structure calculations by DFT. The nine independent elastic constants of SrB_2O_4 are given in Table 4.1. Young's modulus and Poisson's ratio of SrB_2O_4 calculated from its elastic constants are listed in Table 4.2. Because of the special significance of the bulk modulus and shear modulus for technological and engineering applications, we have also calculated these quantities from the elastic constants.

Table 4.1 The single crystal elastic constants (c_{ij} in GPa) for SrB_2O_4 obtained from DFT calculation.

c_{ij}	c_{11}	c_{22}	c_{33}	c_{44}	c_{55}	c_{66}	c_{12}	c_{13}	c_{23}
DFT (GPa)	163.5	238.8	60.4	17.9	19.4	69.5	63.7	47.9	23.5

Table 4.2 The bulk modulus, *B*, shear modulus, *G*, Young's Modulus, *E*, and Poisson's ratio, *v*, for SrB_2O_4 obtained from the single crystal elastic constants.

	B	*G*	*E*	*v*
DFT (GPa)	81.4	43.2	110.1	0.275

Inputting all those calculated material-dependent parameters into Equation 4-4, we predict Young's modulus of the SrB_2O_4 nanorod with 80 nm in diameter is 147.0 ± 5.1 GPa. Our calculated Young's modulus of the SrB_2O_4 nanorod is found to be in good agreement with the one obtained from our experiment, which is 158.2 ± 7.9 GPa. However, comparing the experimental value of Young's modulus of the SrB_2O_4 nanorod with the calculated one shows a difference of 7%. One possible origin for the discrepancy is that the SrB_2O_4 isotropic bulk modulus was very much smaller than that we currently use a flat, extended surface slab to model the nanorod surfaces. For small nanorods, their surfaces are highly curved and hence have a significant transverse stress (strain) component. Thus, the curvature effect must also be properly addressed in an elaborated model for small nanowires. It is worth mentioning that the Young's modulus increases with decreasing diameter of SrB_2O_4 nanorods because that the positive (tensile) surface stress in SrB_2O_4 nanorods would lead to a hardened Young's modulus when reducing nanowire diameters (the Young's modulus of bulk SrB_2O_4 is 110.1 GPa as we calculated in Table 4.2).

During measurements, some variation is inevitable. It can be contributed by various players such as limits in the uniformity of the object being measured, operator differences, and equipment. On the basis of elastic beam-bending theory, the elastic modulus of SrB_2O_4 nanorods, *E*, can be calculated from Equation 4-2 and Equation 4-3. The method to determine the slopes of the F-Z curves is one source of error in Equation 4-3. From Equations 4-2 and 4-4, the error can be brought into the calculation through the

measurements of beam length, *L*, radius, *r* and diameter *D*. Therefore, the best way to reduce this error is to improve the precision of the measured values of *L, r* and *D*. Instead of FEI Quanta 200 Scanning Electron Microscope, we used the Zeiss Ultraplus Thermal Field Emission Scanning Electron Microscope, which is a high vacuum, high resolution scanning electron microscope. The resolution is 1.0 nm at voltage of 15 kV at working distance of 2 mm with precision of ± 1% (relative). We measured *L*, *r,* and *D* by comparing it to the linear scale bar. The scale bar is shown in the SEM image. With consideration of the propagation of the uncertainty, a common approach established by S. J. Kline and F. A. McClintock[179] was used to calculate the error:

$$w_R = [(\frac{\partial R}{\partial x_1} w_1)^2 + (\frac{\partial R}{\partial x_2} w_2)^2 + (\frac{\partial R}{\partial x_3} w_3)^2 + ... + (\frac{\partial R}{\partial x_n} w_n)^2]^{1/2} \quad (4\text{-}5)$$

Where: *R*- a function of a number of independent variables, $x_1, x_2, x_3, ..., x_n$

w_R - uncertainty of *R*

w_i - uncertainty of component x_i.

For the uncertainty of experimental *E,* plug Equation 4-2 into 4-5 by setting function $R = \frac{k_n L^3}{192I} = \frac{4k_n L^3}{192\pi r^4}$, variables k_n = 364.4 ± 24.9 N/m, *L* = 560.0 ± 5.6 nm, *r* = 40.0 ± 0.4 nm. Then,

$$\begin{aligned} \Delta E = w_R &= [(\frac{\partial \frac{4k_n L^3}{192\pi r^4}}{\partial k_n} \Delta k_n)^2 + (\frac{\partial \frac{4k_n L^3}{192\pi r^4}}{\partial L} \Delta L)^2 + (\frac{\partial \frac{4k_n L^3}{192\pi r^4}}{\partial r} \Delta r)^2]^{1/2} \\ &= [(\frac{4L^3}{192\pi r^4} \Delta k_n)^2 + (\frac{3*4k_n L^2}{192\pi r^4} \Delta L)^2 + (-\frac{4*4k_n L^3}{192\pi r^5} \Delta r)^2]^{1/2} \end{aligned} \quad (4\text{-}6)$$

= 6.3 GPa

The standard devation of E_n is 4.8 GPa for five nanorods. The combination of both sources of errors gives an uncertainty of $E_n = \sqrt{6.3^2 + 4.8^2}$ = 7.9 GPa

For the uncertainty of simulated E_n, plug Equation 4-4 into 4-5 by setting function, $R = E_n = E_b + \frac{8}{5} g(1-\nu)\frac{L^2}{D^3}$, variables L = 560.0 ± 5.6 nm, D = 80.0 ± 0.8 nm. In Table 4.2, E_b = 110.1 GPa, ν = 0.275, and g = 0.451 Pa/m. Then,

$$\Delta E = w_R = [(\frac{\partial(E_b + \frac{8}{5} g(1-\nu)\frac{L^2}{D^3})}{\partial L}\Delta L)^2 + (\frac{\partial(E_b + \frac{8}{5} g(1-\nu)\frac{L^2}{D^3})}{\partial D}\Delta D)^2]^{1/2} \quad (4\text{-}7)$$
$$= [(\frac{8}{5} g(1-\nu)\frac{2L}{D^3})\Delta L)^2 + (\frac{8}{5} g(1-\nu)\frac{-3L^2}{D^4}\Delta D)^2]^{1/2}$$

= 5.1 GPa

Therefore, the uncertainty of experimental E_n is 7.9 GPa and the uncertainty of simulated E_n is 5.1 GPa.

Furthermore, experimentally synthesized nanowires are not defect-free in contrast to the perfect isotropic beam studied using elastic beam-bending theory. To avoid sliding during the bending tests, both ends of the nanorods, which bridged over the trench, were clamped by electron beam induced deposition (EBID) of paraffin in SEM (FEI Quanta 200). The suspended SrB_2O_4 nanorod can be treated as a double clamped beam. However, the suspended SrB_2O_4 nanorod could slightly slide during the bending tests. This leads to the error in measuring the piezo position.

All of these errors could have played a role in causing the measured results being discrepant from the exact value. In order to improve the precision of the measured results, we should eliminate experimental uncertainty in instrument calibration, fixing and mounting of samples, measurement of nanowire diameter, and boundary and loading conditions.

4.5 Conclusions

In summary, single crystalline strontium borate (SrB_2O_4) nanorods were synthesized for the first time via a sol-gel route at low temperature. The SrB_2O_4 nanorods are transparent from the ultraviolet to the visible regimes. AFM-based nanoscale three-point bending tests were performed on individual SrB_2O_4 nanorods to probe their mechanical properties and the average bending elastic modulus is 158.2 ± 7.9 GPa, exhibiting a significant increase compared with bulk SrB_2O_4, other borate nanostructures and bulk borates. We calculated the Young's moduli of bulk SrB_2O_4 and SrB_2O_4 nanorods with consideration of surface stress effect of nanorods by density functional theory (DFT). The simulated results were found consistent with the experimental values. Hence, we proposed based on our results that the tensile surface stress, which is an inherent material property, is responsible for the observed higher Young's modulus of those nanomaterials compared to their bulk modulus. Since surface stress plays a very important role in determining Young's modulus of nanomaterials, it is reasonable to expect that the elastic properties of nanomaterials could be engineered by altering the surface stress through rational control of the adsorptions, charges, structure, and impurities in the surfaces.

CHAPTER 5

ZrB_2 nanorods: synthesis, structural, nanomechanical characterization and calculation by DFT[3]

[3] Rui Li, Jianmin Lu, Andreas Heyden, Goutam Koley, and Xiaodong Li. To be submitted.

5.1 Introduction

Zirconium diboride (ZrB_2) is a highly covalent refractory ceramic material with a hexagonal crystal structure. ZrB_2 is an Ultra High Temperature Ceramic (UHTC) with a melting point of 3246 °C. This along with its relatively low density of ~6.09 g/cm^3 (measured density may be higher due to hafnium impurities) and good high temperature strength makes it a candidate for high temperature aerospace applications such as hypersonic flight or rocket propulsion systems.[110-112] In addition, ZrB_2 can be used in nuclear area, such as fuel rod cladding, structural and flow mixing grids, instrumentation tubes, and guide thimbles. The representative synthesis techniques include solid state reactions between zirconium oxide and boric acid and hydrothermal method. ZrB_2 parts are usually hot pressed (pressure applied to the heated powder) and then machined to shape.[113,114] Sintering of ZrB_2 is hindered by the material's covalent nature and presence of surface oxides which increase grain coarsening before densification during sintering.[115,116] Pressureless sintering of ZrB_2 is possible with sintering additives such as boron carbide and carbon which react with the surface oxides to increase the driving force for sintering but mechanical properties are degraded compared to hot pressed ZrB_2.[117] Additions of ~30 vol% SiC to ZrB_2 is often added to ZrB_2 to improve oxidation resistance through SiC creating - a protective oxide layer - similar to aluminum's protective alumina layer. However, to the best of our knowledge, ZrB_2 nanostructures are still absent in literature and their nanoscale-enabled properties are completely unknown.

In our previous work, 1D nanostructures of magnesium borate, aluminum borate, barium borate, and calcium borate have been successfully synthesized. These borate nanostructures exhibit superior mechanical properties. However, the mechanical properties of ZrB_2 are rarely reported. In this chapter, we investigated the synthesis, structural, and mechanical characterization of ZrB_2 nanorods. Single crystalline ZrB_2 nanorods were synthesized for the first time via a simple route at a relatively low temperature of 800 °C. The X-ray diffraction (XRD) analysis revealed that the as-synthesized nanorods have hexagonal phase of ZrB_2 (JCPDS file, No. 34-0423), with lattice constants of a= 3.17, b= 3.17 and c = 3.53 Å, and space group of *P6/mmm*. The high-resolution transmission electron microscopy (HRTEM) characterization showed that individual ZrB_2 nanorods are single crystals with the growth direction along the [001] orientation. AFM-based nanoindentation tests were performed directly on individual nanorods to probe their mechanical properties. Furthermore, the Young's modulus of ZrB_2 nanorods was calculated with consideration of surface stress effect of nanorods by density functional theory. This theoretical prediction agrees well with the experimental results.

Such structural and mechanical information provides design guidelines for developing ZrB_2 nanostructure-based nanodevices and nanocomposites, and lays a constitutive foundation for modeling the nanostructures of ZrB_2 and other boride nanostructures.

5.2 Experimental

All chemicals used in our experiments were purchased and used without any further

purification. Zirconium chloride ($ZrCl_4$) was purchased from Alfa Aesar. Sodium borohydride ($NaBH_4$) and Sodium chloride (NaCl) were purchased from Sigma Aldrich.

In a typical experiment, 1 mmol of $ZrCl_4$ and 2 mmol of $NaBH_4$ and 10 mmol NaCl were mixed in agate mortar and ground by pestle at room temperature. The as-prepared mixture were placed in an alumina boat and annealed at 800 ^oC for 1 h in Ar. The black products were washed with distilled water and absolute ethanol three times, respectively, and dried at room temperature.

The chemical process for synthesizing ZrB_2 nanorods can be described in the following reaction:

$$ZrCl_4 + 2NaBH_4 = ZrB_2 + 2NaCl + 2HCl\uparrow + 3H_2\uparrow \qquad (5\text{-}1)$$

The crystal structure of the products was characterized by XRD (Rigaku DMax 2200 using Cu K_α radiation). A few drops of ethanol solution containing the as-prepared products were deposited onto copper grids for transmission electron microscopy (TEM, Hitachi H-8000), and HRTEM (JEOL JEM 2010F) analyses. The solvent was then vaporized under ambient conditions. The resulting product was collected for characterization by scanning electron microscopy (SEM, Zeiss Ultra Plus FESEM). Chemical compositions and oxidation states of the products were determined by X-ray photoelectron spectroscopy (XPS, a Kratos Axis Ultra DLD instrument equipped with a monochromated Al Ka x-ray source and hemispherical analyzer capable of an energy resolution of 0.5 eV). Nanoindentation tests were performed directly on individual

nanorods to probe their mechanical properties using AFM. To avoid sliding during the bending tests, both ends of the nanorods, which bridged over the trench, were clamped by electron beam induced deposition (EBID) of paraffin in SEM (FEI Quanta 200).[100-101] This carbonaceous material thin layer and the strong adhesion force between the nanorod and the edges of the trench ensured the fully clamping of the both ends of the ZrB_2 nanorod during the tests.

5.3 Calculation methods

Our first-principles calculations were performed using the density functional theory implementation, VASP. [171,172] We used the projector augmented wave method and the GGA-PW91 functional for exchange and correlation. We chose a kinetic energy cutoff of 600 eV to expand the electronic wave functions in the plane wave basis. The energy convergence for all geometry optimization was set to be 1×10^{-5} eV.

ZrB_2 has the hexagonal AlB_2 structure (space group: P6/mmm) with experimental lattice constants of a = b = 3.168 Å and c = 3.523 Å. For ZrB_2 nanorods grown along the [001] direction, (210) and (110) surface are their lateral facets. For the (210) surface calculations, we have used a supercell with 6 layers (6 Zr atoms and 12 B atoms) and a vacuum of 15 Å, and employed a 17×15×1 k-point grid for all the subsequent calculations. For the (110) surface calculations, we have used a supercell with 5 layers (10 Zr atoms and 20 B atoms) and a vacuum of 15 Å, and employed a 15×9× 1 k-point grid for all the subsequent calculations. To examine the strain effect, we deformed both surfaces by strains of ε in the range of [-0.02, 0.02] with an interval of 0.005.

5.4 Results and discussion

Figure 5.1 shows a representative XRD pattern of the product synthesized via the sol-gel method at 800 ^{o}C for 1 h. All the peaks can be readily indexed to the hexagonal phase of ZrB_2 (JCPDS file, No. 34-0423), with lattice constants of *a*= 3.17, *b*= 3.17 and *c* = 3.53 Å, and space group of *P6/mmm*. No impurity peaks were observed, indicating high purity of the product. The SEM image of the product shown in Figure 5.2a reveals that the product is composed of ZrB_2 nanorods with an average diameter of 70 nm and length ranging from 1 to 3 μm. The TEM image (Figure 5.2b) shows that the ZrB_2 nanorods have very smooth surfaces and the average diameter and length of the nanorod are consistent with the SEM results. The representative HRTEM image and corresponding fast-Fourier transform pattern at the zone axis jointly suggest that the synthesized ZrB_2 nanorods are single crystals with the growth direction along the [001] orientation, which is consistent with the stronger diffraction peak intensity of (001) in the XRD pattern in comparison with the standard XRD pattern in Figure 1a. No defects such as dislocations and twins were found in individual ZrB_2 nanorods. The measured distance between the lattice fringes for the (001) planes is 0.35 nm, in good agreement with the XRD results.

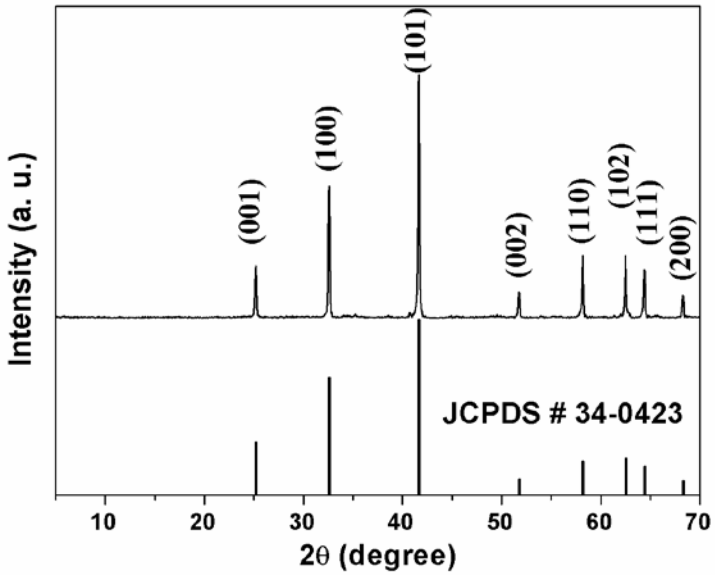

Figure 5.1 XRD pattern of the ZrB_2 nanorods and the corresponding JCPDS #34-0423 standard pattern.

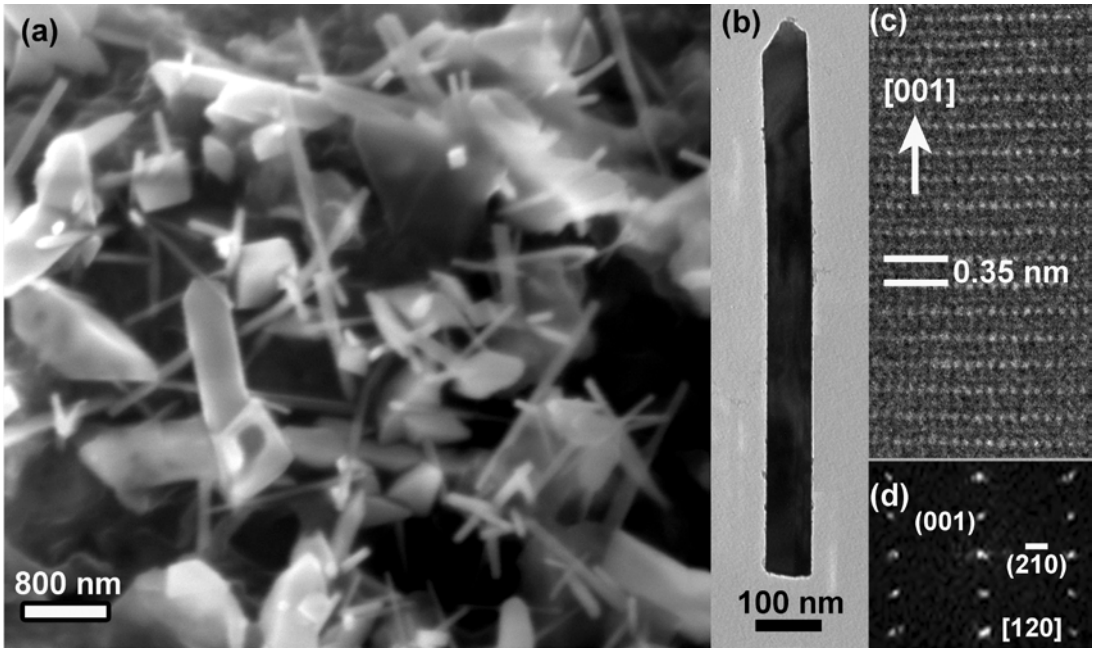

Figure 5.2 (a) SEM image, (b) TEM image, (c) HRTEM image and (d) corresponding fast Fourier transform (FFT) pattern of ZrB_2 nanorods.

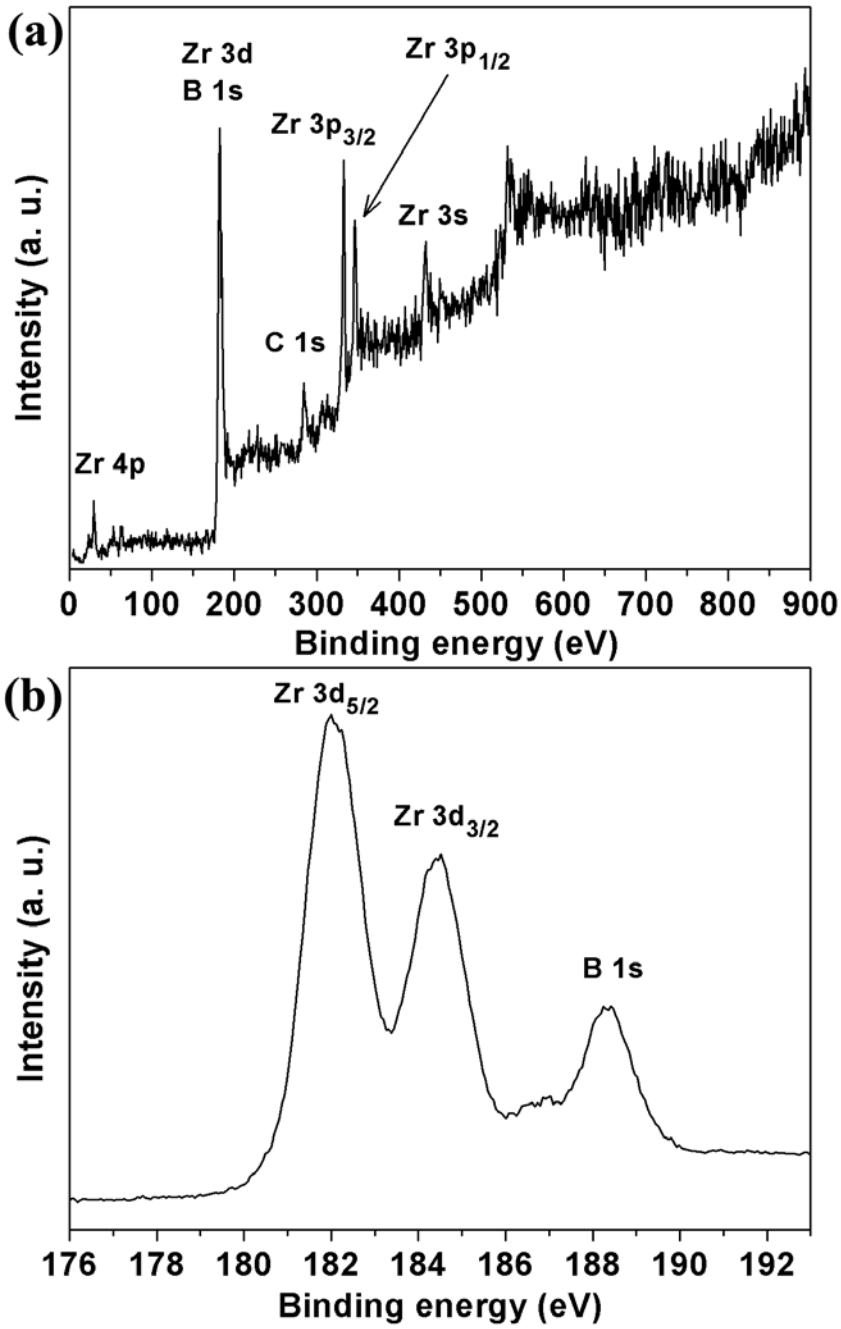

Figure 5.3 XPS spectra of ZrB_2 nanorods. (a) Survey spectrum, (b) detailed spectra of Zr 3d5/2, Zr 3d3/2 and B 1s core levels.

XPS analysis was carried out to further characterize chemical compositions of the ZrB_2 nanorods (Figure 5.3). The binding energies were corrected by taking C 1s at 284.8 eV.

The survey spectrum, as shown in Figure 5.3a, exhibits Zr 3d, B 1s and C 1s core levels, and O Auger peak. In Figure 5.3b, the peaks at 182.1 eV and 184.6 eV in the curve can be attributed to Zr $3d_{5/2}$ and Zr $3d_{3/2}$, respectively. In Figure 5.3b, the peak at 188.5 eV can be assigned to B 1s core level in boride. The XPS results for the ZrB_2 nanorods are in good agreement with the reported values for bulk ZrB_2.

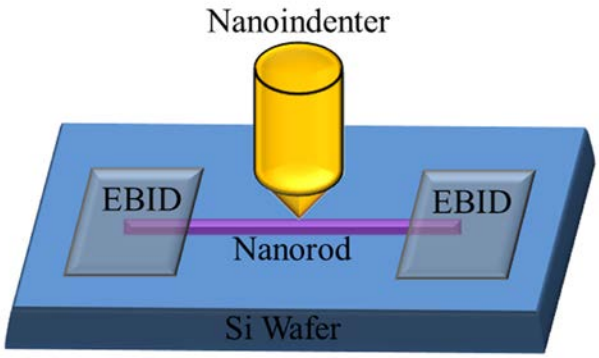

Figure 5.4 Schematic image of an EBID-fixed ZrB_2 nanorod in a nanoindentation test with an AFM tip.

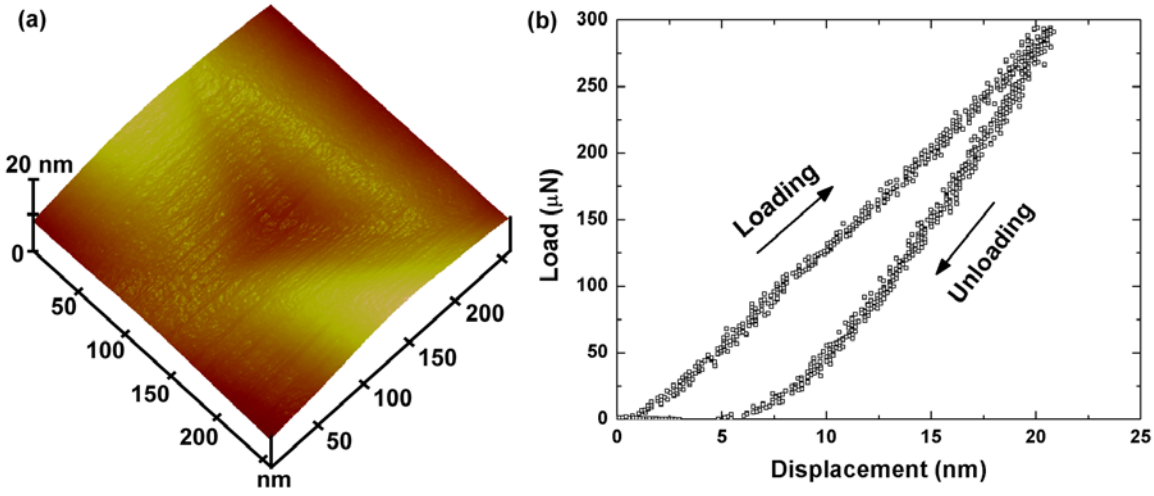

Figure 5.5 (a) 3D AFM image of a nanoindentation impression made on a ZrB_2 nanorod. (b) Representative nanoindentation load-displacement curve.

Figure 5.4 is the schematic of nanoindentation on a nanorod fixed to a silicon substrate by EBID method. Figure 5.5a reveals the representative three dimensional AFM image of an indentation impression on one ZrB_2 nanorod. Figure 5.5b shows a representative nanoindentation load-displacement curve of a ZrB_2 nanorod. Compared to bulk ZrB_2, the Young's modulus of the ZrB_2 nanorods is decreased when decreasing their diameters in Figure 5.6. Li and Bhushan studied that bending strength of silicon beams exhibits a clear specimen size effect with nanoscale numbers being twice as large as numbers reported for large-scale specimens.[165] Haque and Saif discovered that 1D Al and Au nanostructures exhibit reduction in Young's modulus.[118] Petrova *et al*. revealed a decrease in Young's modulus with decreasing size on gold nanowires.[119,120] ZnS nanobelts achieved 79% increase in hardness but 52% decrease in elastic modulus compared to bulk ZnS.[166] The decrease in hardness and elastic modulus of the ZrB_2 nanorods could probably be attributed to their high surface-to-volume ratio. Unlike the atoms locked in the lattice, surface atoms are less constrained, thereby making the ZrB_2 nanorods easier to deform in the elastic regime, and consequently leading to a lower hardness and a lower elastic modulus. It is still not clear regarding the mechanism that controls the mechanical properties of the nanomaterials.

In this dissertation, we elucidate the size dependency of the elastic modulus of ZrB_2 nanorods using the concept of surface stress. Surface stress is defined as the reversible work per unit area required to elastically stretch a surface, while surface energy is the

reversible work per unit area required to create a surface.[169] In Ref. 168 and 169, the elastic modulus of a nanowire is proposed to be described in the following form:

$$E_n = E_b + \frac{8}{5} g(1-\nu)\frac{L^2}{D^3} \qquad (5\text{-}1)$$

where, E_n and E_b are the elastic modulus of the nanorod and bulk materials, respectively, L and D is the length and diameter of the nanorod, g is the surface stress, and ν is Poisson's ratio. Thus, a positive (tensile) surface stress would lead to an increase in elastic modulus with the decreasing nanowire diameters, while a negative (compressive) surface stress would lead to a decrease in elastic modulus with the decreasing nanorod diameters. The above relation has been shown to be valid for Ag, Pd, and ZnO nanowires.[169] Our first-principles calculations for ZrB_2 nanorods were performed using the VASP code.[171,172] We used the projector augmented wave method and the generalized gradient approximation of Perdew and Wang[170] for exchange and correlation. We chose a kinetic energy cutoff of 600 eV to expand the electronic wave functions in the plane wave basis. The energy convergence for all geometry optimization was set to be 1×10^{-5} eV.

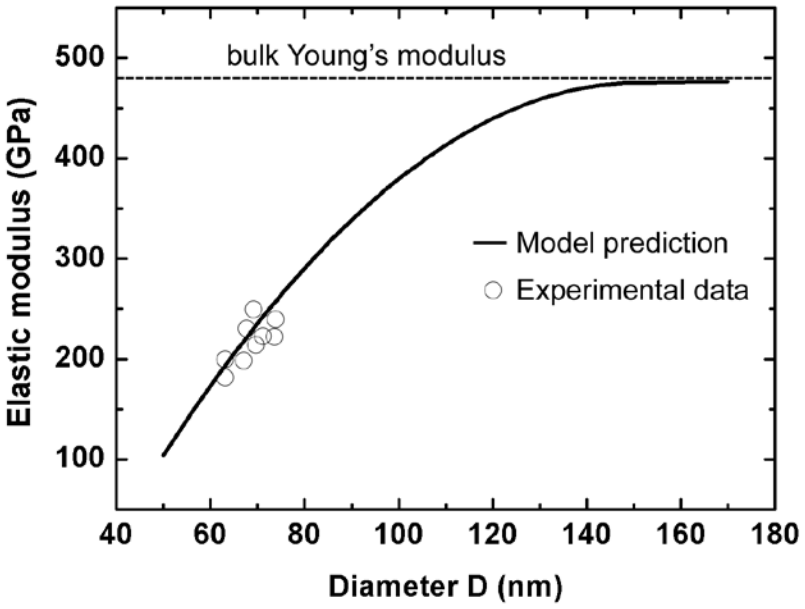

Figure 5.6 Predicted size dependency and experimental data of the elastic modulus of ZrB_2 nanorod.

In Figure 5.6, we plotted the calculated elastic modulus of ZrB_2 nanorods as a function of their diameters. It is predicted that due to surface stress effect, the Young's modulus of ZrB_2 nanorods would be lower than the Young's modulus of bulk ZrB_2 and decreases with the decreasing diameters. Our theoretical predictions are consistent with our experimental measurements. However, comparing the experimental value of Young's modulus of the ZrB_2 nanorod with the calculated one shows a difference of less than 10%. One possible origin for the discrepancy is that their isotropic bulk modulus was very much smaller than that we currently use a flat, extended surface slab to model the nanorod surfaces. For small nanorods, their surfaces are highly curved and hence have a significant transverse stress (strain) component. Thus, the curvature effect must also be

properly addressed in an elaborated model for small nanorods. It is worth mentioning that the Young's modulus decreases with decreasing diameter of ZrB_2 nanorods because that the negative (compressive) surface stress in ZrB_2 nanorods would lead to a softened Young's modulus when reducing nanowire diameters.

During measurements, some variation is inevitable. It can be contributed by various players such as limits in the uniformity of the object being measured, operator differences, and equipment. By first-principles DFT methods, the elastic modulus of ZrB_2 nanorods, *E*, can be calculated from Equation 5-1, the error can be brought into the calculation through the measurements of beam length, *L*, and diameter, *D*. Therefore, the best way to reduce this error is to improve the precision of the measured values of *L* and *D*. Instead of FEI Quanta 200 Scanning Electron Microscope, we used the Zeiss Ultraplus Thermal Field Emission Scanning Electron Microscope, which is a high vacuum, high resolution scanning electron microscope. The resolution is 1.0 nm at voltage of 15 kV at working distance of 2 mm with precision of ± 1% (relative). We measured *L* and *D* by comparing it to the linear scale bar. The scale bar is shown in the SEM image. With consideration of the propagation of the uncertainty, a common approach established by S. J. Kline and F. A. McClintock[179] was used to calculate the error:

$$w_R = [(\frac{\partial R}{\partial x_1} w_1)^2 + (\frac{\partial R}{\partial x_2} w_2)^2 + (\frac{\partial R}{\partial x_3} w_3)^2 + ... + (\frac{\partial R}{\partial x_n} w_n)^2]^{1/2} \qquad (5\text{-}2)$$

Where: *R*- a function of a number of independent variables, $x_1, x_2, x_3, ..., x_n$

w_R - uncertainty of R

w_i - uncertainty of component x_i.

For the uncertainty of simulated E_n, plug Equation 5-1 into 5-2 by setting function, $R = E_n = E_b + \frac{8}{5} g(1-\nu)\frac{L^2}{D^3}$, variables L = 810.0 ± 8.1 nm, D is in the range of 60.0-80.0 ± 1% nm. E_b = 480 GPa, ν = 0.132, and g = -0.127 Pa/m.[180] Then,

$$\Delta E_n = w_R = [(\frac{\partial(E_b + \frac{8}{5} g(1-\nu)\frac{L^2}{D^3})}{\partial L}\Delta L)^2 + (\frac{\partial(E_b + \frac{8}{5} g(1-\nu)\frac{L^2}{D^3})}{\partial D}\Delta D)^2]^{1/2}$$
$$= [(\frac{8}{5} g(1-\nu)\frac{2L}{D^3})\Delta L)^2 + (\frac{8}{5} g(1-\nu)\frac{-3L^2}{D^4}\Delta D)^2]^{1/2} \quad (5\text{-}3)$$
$$= \frac{1.73*10^{-12}}{D^3}$$

D is in the range of 60.0-80.0 ± 1% nm, therefore, the percent uncertainty of E_n is ~ ±3%.

In addition, experimentally synthesized nanowires are not defect-free in contrast to the perfect isotropic beam studied using elastic beam-bending theory. To avoid sliding during the bending tests, both ends of the nanorods, which were placed on the silicon wafer, were clamped by electron beam induced deposition (EBID) of paraffin in SEM (FEI Quanta 200). However, the clamped ZrB_2 nanorod could slightly slide during the bending tests. This leads to the error in measuring the piezo position.

All of these errors could have played a role in causing the measured results being discrepant from the exact value. In order to improve the precision of the measured results, we should eliminate experimental uncertainty in instrument calibration, fixing and

mounting of samples, measurement of nanowire diameter, and boundary and loading conditions.

5.5 Conclusions

We investigated the synthesis and structural characterization of ZrB_2 nanorods. Single crystalline ZrB_2 nanorods were synthesized for the first time via a simple route at a relatively low temperature of 800 ^oC. The XRD analysis revealed that the as-synthesized nanorods have hexagonal phase of ZrB_2. Nanoindentation tests were performed on individual ZrB_2 nanorods to probe their mechanical properties using AFM. Furthermore, the Young's modulus of ZrB_2 nanorods was calculated with consideration of surface stress effect of nanorods by first-principles DFT method. It was found that the theoretical prediction agrees well with the experimental results.

CHAPTER 6

Summary

This dissertation provided the synthesis, characterization and experimental studies on 1D boron-based nanomaterials. Below is the summary of four 1D boron-based nanomaterials that have been studied.

Barium polyborate, $Ba_3B_6O_9(OH)_6$ (BBOH), nanorods were synthesized for the first time via a low temperature, organic-free hydrothermal route. These nanorods can be easily transformed into β-BaB_2O_4 (BBO) nanospindles through heat treatment at 810 ^oC for 3 h. Both BBOH nanorods and BBO nanospindles are transparent from ultraviolet to the visible regions.

Single crystalline strontium borate (SrB_2O_4) nanorods were synthesized for the first time via a sol-gel route at low temperature. The SrB_2O_4 nanorods are transparent from the ultraviolet to the visible regimes. AFM-based nanoscale three-point bending tests were performed on individual SrB_2O_4 nanorods to probe their mechanical properties and the average bending elastic modulus is 158.2 ± 7.9 GPa, exhibiting a significant increase compared with bulk SrB_2O_4, other borate nanostructures and bulk borates. We calculated the Young's moduli of bulk SrB_2O_4 and SrB_2O_4 nanorods with consideration of surface stress effect of nanorods by density functional theory (DFT). The simulated results

were found consistent with the experimental values.

We investigated the synthesis and structural characterization of ZrB_2 nanorods. Single crystalline ZrB_2 nanorods were synthesized for the first time via a simple route at a relatively low temperature of 800 ^oC. The XRD analysis revealed that the as-synthesized nanorods have hexagonal phase of ZrB_2. Nanoindentation tests were performed on individual ZrB_2 nanorods to probe their mechanical properties. Furthermore, the Young's modulus of ZrB_2 nanorods was calculated with consideration of surface stress effect of nanorods by DFT. It was found that the theoretical prediction agrees well with the experimental results.

Overall, the achievements presented here are only basic research on boron-based nanomaterials. More reseach remains to be done in nanoscale mechanics studies to investigate interesting properties of nanomaterials and explore the governing mechanism through various ways. It is hoped that the findings and mechanisms presented in this dissertation may provide the guidelines of rational design and applications of boron-based nanomaterials, further miniaturization of MEMS/NEMS devices and nanocomposites.

CHAPTER 7

Directions of Future Research

The work presented in this dissertation focuses on the synthesis, characterization and experimental studies on four kinds of 1D boron-based nanomaterials. But there are still questions to be solved to fully discover the potential of boron-based nanomaterials.

1. The first step for doing nanomaterials research is to obtain the nanomaterials, in other words, to synthesize the nanomaterials. One major challenge is the difficulty to controllably synthesize the products in term of size, shape and composition. Breakthroughs and proper controls are needed in sample growth process.
2. Another challenge is to reduce or eliminate the use or generation of hazardous substances, which is one of the principles of Green Chemistry. Green chemistry is increasingly seen as a powerful tool that researchers must use to evaluate the environmental impact of nanotechnology.
3. Although some 1D boron-based nanomaterials have been successfully synthesized and investigated, e.g. boron nanowires, there are still fresh lands for exploration on other 1D boron-based nanomaterials. For example, magnesium diboride (MgB_2) becomes superconducting at 39 degrees Kelvin, one of the highest known transition temperatures of any superconductor. What's more, its puzzling characteristics

4. include more than one superconducting energy gap. But the properties of nanoscale MgB_2 are still unknown and need to study.
5. Future research on 1D nanomaterials may direct to molecular scale modeling approaches for predictions of size dependency.
6. Applications in industry of 1D boron-based nanomaterials would be developed, such as, miniaturization of MEMS/NEMS devices, which are inherently small, thus offering attractive characteristics such as reduced size, weight, and power dissipation and improved speed and precision compared to their macroscopic counterparts.

REFERENCES

(1) https://en.wikipedia.org/wiki/Boron.

(2) Atuchin, V. V.; Kesler, V. G.; Kokh, A. E.; Pokrovsky, L. D.: X-ray photoelectron spectroscopy study of beta-BaB_2O_4 optical surface. *Applied Surface Science* **2004**, *223*, 352-360.

(3) Cheng, L. K.; Bosenberg, W. R.; Tang, C. L.: Growth and characterization of nonlinear optical-crystals suitable for frequency-conversion. *Progress in Crystal Growth and Characterization of Materials* **1990**, *20*, 9-57.

(4) Eimerl, D.; Davis, L.; Velsko, S.; Graham, E. K.; Zalkin, A.: Optical, mechanical, and thermal-properties of barium borate. *Journal of Applied Physics* **1987**, *62*, 1968-1983.

(5) Fedorov, P. P.; Kokh, A. E.; Kononova, N. G.: The barium borate beta-BaB_2O_4 as a material for nonlinear optics. *Uspekhi Khimii* **2002**, *71*, 741-763.

(6) Feigelson, R. S.; Raymakers, R. J.; Route, R. K.: Growth of nonlinear crystals for frequency-conversion. *Progress in Crystal Growth and Characterization of Materials* **1990**, *20*, 115-160.

(7) Geng, J.; Zhu, J. J.; Lu, D. J.; Chen, H. Y.: Hollow $PbWO_4$ nanospindles via a facile sonochemical route. *Inorganic Chemistry* **2006**, *45*, 8403-8407.

(8) Kouta, H.; Kuwano, Y.; Ito, K.; Marumo, F.: Beta-BaB_2O_4 single-crystal growth by Czochralski method. *Journal of Crystal Growth* **1991**, *114*, 676-682.

(9) Li, Y.; Fan, Z. Y.; Lu, J. G.; Chang, R. P. H.: Synthesis of magnesium borate ($Mg_2B_2O_5$) nanowires by chemical vapor deposition method. *Chemistry of Materials* **2004**, *16*, 2512-2514.

(10) Liu, B.; Zeng, H. C.: Hydrothermal synthesis of ZnO nanorods in the diameter regime of 50 nm. *Journal of the American Chemical Society* **2003**, *125*, 4430-4431.

(11) Liu, N.; Tian, Y.; Yu, L.; Li, Q.; Meng, F.; Zheng, Y.; Zhang, G.; Liu, Z.; Li, J.; Jiang, F.: Synthesis and surface modification of uniform barium borate nanorods for lubrication. *Journal of Alloys and Compounds* **2008**, *466*, L11-L14.

(12) Lu, C.; Dimov, S. S.; Lipson, R. H.: Poly(vinyl pyrrolidone)-assisted sol-gel deposition of quality beta-barium borate thin films for photonics applications. *Chemistry of Materials* **2007**, *19*, 5018-5022.

(13) Ma, R. Z.; Bando, Y.; Sato, T.: Nanowires of metal borates. *Applied Physics Letters* **2002**, *81*, 3467-3469.

(14) Ma, R. Z.; Bando, Y.; Sato, T.; Tang, C. C.; Xu, F. F.: Single-crystal $Al_{18}B_4O_{33}$ microtubes. *Journal of the American Chemical Society* **2002**, *124*, 10668-10669.

(15) Nikogosyan, D. N.: Beta-barium borate (BBO) - a review of its properties and applications. *Applied Physics A-Materials Science & Processing* **1991**, *52*, 359-368.

(16) Raja, C. R.; Gobinathan, R.; Gnanam, F. D.: Dielectric-propreties of beta-barium borate and potassium pentaborate single-crystals. *Crystal Research and Technology* **1993**, *28*, 737-743.

(17) Singh, S.; Kumar, A.; Singh, D.; Thind, K. S.; Mudahar, G. S.: Barium-borate-flyash glasses: as radiation shielding materials. *Nuclear Instruments & Methods in Physics Research Section B-Beam Interactions with Materials and Atoms* **2008**, *266*, 140-146.

(18) Song, H. S.; Elssfah, E. M.; Zhang, J.; Lin, J.; Luo, J. J.; Liu, S. J.; Huang, Y.; Ding, X. X.; Gao, J. M.; Qi, S. R.; Tang, C. C.: High-aspect-ratio aluminum borate nanowire bundles supported by sucrose. *Journal of Physical Chemistry B* **2006**, *110*, 5966-5969.

(19) Tang, C. C.; Elssfah, E. M.; Zhang, J.; Chen, D. F.: Morphology- and composition-controlled synthesis of aluminium borate nanowires without catalysts. *Nanotechnology* **2006**, *17*, 2362-2367.

(20) Tao, X. Y.; Li, X. D.: Catalyst-free synthesis, structural, and mechanical characterization of twinned $Mg_2B_2O_5$ nanowires. *Nano Letters* **2008**, *8*, 505-510.

(21) Wang, H.; Brandl, D. W.; Le, F.; Nordlander, P.; Halas, N. J.: Nanorice: a hybrid plasmonic nanostructure. *Nano Letters* **2006**, *6*, 827-832.

(22) Wersand-Quell, S.; Orsal, G.; Thevenin, P.; Bath, A.: Growth of beta barium borate (beta-BaB_2O_4) thin films by injection metal organic chemical vapour deposition. *Thin Solid Films* **2007**, *515*, 6507-6511.

(23) Xia, Y. N.; Yang, P. D.; Sun, Y. G.; Wu, Y. Y.; Mayers, B.; Gates, B.; Yin, Y. D.; Kim, F.; Yan, Y. Q.: One-dimensional nanostructures: synthesis, characterization, and applications. *Advanced Materials* **2003**, *15*, 353-389.

(24) Yogo, T.; Kikuta, K.; Niwa, K.; Ichida, M.; Nakamura, A.; Hirano, S.: Processing of beta-BaB_2O_4 thin films through metal organics. *Journal of Sol-Gel Science and Technology* **1997**, *9*, 201-209.

(25) Yu, Z. T.; Shi, Z.; Chen, W.; Jiang, Y. S.; Yuan, H. M.; Chen, J. S.: Synthesis and X-ray crystal structures of two new alkaline-earth metal borates: $SrBO_2(OH)$ and $Ba_3B_6O_9(OH)_6$. *Journal of the Chemical Society-Dalton Transactions* **2002**, 2031-2035.

(26) Zhang, J.; Huang, Y.; Lin, J.; Ding, X. X.; Huang, Z. X.; Qi, S. R.; Tang, C. C.: From $Al_4B_2O_9$ nanowires to BN-coated $Al_{18}B_4O_{33}$ nanowires. *Journal of Physical Chemistry B* **2005**, *109*, 13060-13062.

(27) Zhang, M. F.; Fan, H.; Xi, B. J.; Wang, X. Y.; Dong, C.; Qian, Y. T.: Synthesis, characterization, and luminescence properties of uniform Ln^{3+}-doped YF3 nanospindles. *Journal of Physical Chemistry C* **2007**, *111*, 6652-6657.

(28) Bao, L. H.; Xu, Z.-H.; Li, R.; Li, X. D.: Catalyst-Free Synthesis and structural and mechanical characterization of single crystalline $Ca_2B_2O_5 \cdot H_2O$ nanobelts and stacking faulted $Ca_2B_2O_5$ nanogrooves. *Nano Letters* **2010**, *10*, 255-262.

(29) Guo, L. M.; Kuang, Y. J.; Yang, X. D.; Yu, Y. L.; Yao, J. H.; Cao, Y. A.: Photocatalytic reduction of CO_2 into CH_4 using SrB_2O_4 catalyst. *Acta Physico-Chimica Sinica* **2013**, *29*, 397-402.

(30) Li, R.; Bao, L. H.; Li, X. D.: Synthesis, structural, optical and mechanical characterization of SrB_2O_4 nanorods. *Crystengcomm* **2011**, *13*, 5858-5862.

(31) Liu, D.; Chen, P.; Chen, M.; Liu, Z.: Improved interfacial adhesion in PBO fiber/bismaleimide composite with oxygen plasma plus aging and humid resistance properties. *Materials Science and Engineering A-Structural Materials Properties Microstructure and Processing* **2012**, *532*, 78-83.

(32) Liu, X.; Zhu, W.; Cui, X.; Liu, T.; Zhang, Q.: Facile thermal conversion route synthesis, characterization, and optical properties of rod-like micron nickel borate. *Powder Technology* **2012**, *222*, 160-166.

(33) Lu, C.; Lipson, R. H.: Controlled hydrothermal synthesis of beta-BBO plates for detection of second harmonic generation. *Crystengcomm* **2010**, *12*, 4352-4355.

(34) Meng, T.; Xie, R.; Ju, X. J.; Cheng, C. J.; Wang, S.; Li, P. F.; Liang, B.; Chu, L. Y.: Nano-structure construction of porous membranes by depositing nanoparticles for enhanced surface wettability. *Journal of Membrane Science* **2013**, *427*, 63-72.

(35) Qu, G.; Hu, Z.; Wang, Y.; Yang, Q.; Tong, L.: Synthesis of optical-quality single-crystal beta-BaB_2O_4 microwires and nanowires. *Advanced Functional Materials* **2013**, *23*, 1232-1237.

(36) Rasouli, M.; Yaghobi, N.; Chitsazan, S.; Sayyar, M. H.: Effect of nanocrystalline zeolite Na-Y on meta-xylene separation. *Microporous and Mesoporous Materials* **2012**, *152*, 141-147.

(37) Si, P.; Liu, J.; Zhen, Z.; Liu, X.; Lakshminarayana, G.; Kityk, I. V.: Synthesis and characterization of NLO chromophore with benzo 1,2-b:4,5-b' dithiophene unit as pi-electron bridge. *Tetrahedron Letters* **2012**, *53*, 3393-3396.

(38) Vijayakumar, P.; Babu, C. A.; Ramasamy, P.: Synthesis, crystal growth and characterization of nonlinear optical organic crystal: p-toluidinium p-toluenesulphonate. *Materials Research Bulletin* **2012**, *47*, 957-962.

(39) Wang, Q.; Jiang, H.; Gong, H.; Chu, G.; Lin, C. H.; Dong, X. L.: Synthesis, characterization and thermal stability of a crystalline niobium oxysulfate. *Journal of Alloys and Compounds* **2012**, *521*, 60-65.

(40) Yang, Y.; Pan, S. L.; Hou, X. L.; Wang, C. Y.; Poeppelmeier, K. R.; Chen, Z. H.; Wu, H. P.; Zhou, Z. X.: A congruently melting and deep UV nonlinear optical material: $Li_3Cs_2B_5O_{10}$. *Journal of Materials Chemistry* **2011**, *21*, 2890-2894.

(41) Zhang, J.; He, G. P.; Li, R. H.; Chen, X.: Fabrication and optical properties of single-crystalline beta barium borate nanorods. *Journal of Alloys and Compounds* **2010**, *489*, 504-508.

(42) Zhao, G. W.; Zhang, L. P.; Wang, J. L.; Li, J.; Qian, Q. L.; Pan, X. Y.; Gu, Y. L.: Synthesis of thorn-like $Ca_2B_2O_5 \cdot H_2O$ by hydrothermal method. *Bulletin of Materials Science* **2011**, *34*, 1197-1199.

(43) Zhu, W. C.; Wang, X. L.; Zhang, X.; Zhang, H.; Zhang, Q.: Hierarchical laminar superstructures of rhombic priceite ($Ca_4B_{10}O_{19}\cdot 7H_2O$): facile hydrothermal synthesis, shape evolution, optical, and thermal decomposition properties. *Crystal Growth & Design* **2011**, *11*, 2935-2941.

(44) Zhu, W. C.; Yang, Y.; Hu, S.; Xiang, G. L.; Xu, B.; Zhuang, J.; Wang, X.: $(Ni, Mg)_3Si_2O_5(OH)_4$ solid-solution nanotubes supported by sub-0.06 wt % palladium as a robust high-efficiency catalyst for suzuki-miyaura cross-coupling reactions. *Inorganic Chemistry* **2012**, *51*, 6020-6031.

(45) Zhu, W. C.; Zhang, G. L.; Liu, C. M.; Zhang, Q.; Zhu, S. L.: Hierarchical strontium carbonate submicron spheres self-assembled under hydrothermal conditions. *Crystal Research and Technology* **2010**, *45*, 845-850.

(46) Zhu, W. C.; Zhang, Q.; Xiang, L.; Zhu, S. L.: Repair the pores and preserve the morphology: formation of high crystallinity 1D nanostructures via the thermal conversion route. *Crystal Growth & Design* **2011**, *11*, 709-718.

(47) Zhu, W. C.; Zhang, X.; Wang, X. L.; Zhang, H.; Zhang, Q.; Xiang, L.: Short belt-like $Ca_2B_2O_5\cdot H_2O$ nanostructures: hydrothermal formation, FT-IR, thermal decomposition, and optical properties. *Journal of Crystal Growth* **2011**, *332*, 81-86.

(48) Gao, Y. P.; Xu, Z.; Liu, R. P.: Crystalline boron nanowires grown by magnetron sputtering. *Materials Science and Engineering A-Structural Materials Properties Microstructure and Processing* **2006**, *434*, 53-57.

(49) Guo, L.; Singh, R. N.; Kleebe, H. J.: Nucleation and growth of boron nanowires on ZrB_2 particles. *Chemical Vapor Deposition* **2006**, *12*, 448-452.

(50) Liu, F.; Su, Z. J.; Li, L.; Mo, F. Y.; Jin, S. Y.; Deng, S. Z.; Chen, J.; Shen, C. M.; Gao, H. J.; Xu, N. S.: Effect of contact mode on the electrical transport and field-emission performance of individual boron nanowires. *Advanced Functional Materials* **2010**, *20*, 1994-2003.

(51) Tian, J. F.; Hui, C.; Bao, L. H.; Li, C.; Tian, Y. A.; Ding, H.; Shen, C. M.; Gao, H. J.: Patterned boron nanowires and field emission properties. *Applied Physics Letters* **2009**, *94*, 083101.

(52) Tian, J. F.; Cai, J. M.; Hui, C.; Zhang, C. D.; Bao, L. H.; Gao, M.; Shen, C. M.; Gao, H. J.: Boron nanowires for flexible electronics. *Applied Physics Letters* **2008**, *93*, 122105.

(53) Wang, Y. Q.; Cao, L. M.; Duan, X. F.: Amorphous feather-like boron nanowires. *Chemical Physics Letters* **2003**, *367*, 495-499.

(54) Yang, Q.; Sha, J.; Xu, J.; Ji, Y. J.; Ma, X. Y.; Niu, J. J.; Hua, H. Q.; Yang, D. R.: Aligned single crystal boron nanowires. *Chemical Physics Letters* **2003**, *379*, 87-90.

(55) Yoon, J. W.; Shim, K. B.: Growth of crystalline boron nanowires by pulsed laser ablation. *Journal of Ceramic Processing Research* **2011**, *12*, 199-201.

(56) Zhang, Y. J.; Ago, H.; Yumura, M.; Ohshima, S.; Uchida, K.; Komatsu, T.; Iijima, S.: Study of the growth of boron nanowires synthesized by laser ablation. *Chemical Physics Letters* **2004**, *385*, 177-183.

(57) Zhang, H.; Song, P. X.; Hu, X. Y.; Zhang, Y. J.; Tian, Y. T.; Li, X. J.: Influences of Si and Ni catalysts on the growth of boron nanowires. *Rare Metal Materials and Engineering* **2012**, *41*, 1717-1720.

(58) Li, J. L. L.; He, T.; Yang, G. W.: Ferromagnetism and semiconducting of boron nanowires. *Nanoscale Research Letters* **2012**, *7*, 1-6.

(59) Lin, C. H.; Ni, H.; Wang, X. N.; Chang, M.; Chao, Y. J.; Deka, J. R.; Li, X. D.: In situ nanomechanical characterization of single-crystalline boron nanowires by buckling. *Small* **2010**, *6*, 927-931.

(60) Ding, W. Q.; Calabri, L.; Chen, X. Q.; Kohhaas, K. M.; Ruoff, R. S.: Mechanics of crystalline boron nanowires. *Composites Science and Technology* **2006**, *66*, 1112-1124.

(61) Otten, C. J.; Wang, D. W.; Lu, J. G.; Buhro, W. E.: Electrical properties of boron nanowires. *Modern Aspects of Main Group Chemistry*, **2006**, *917*, 362-375.

(62) Sun, L. L.; Matsuoka, T.; Tamari, Y.; Shimizu, K.; Tian, J. F.; Tian, Y. A.; Zhang, C. D.; Shen, C. M.; Yi, W.; Gao, H. J.; Li, J. Q.; Dong, X. L.; Zhao, Z. X.: Pressure-induced superconducting state in crystalline boron nanowires. *Physical Review B* **2009**, *79*, 140505.

(63) Tian, Y.; Shen, C. M.; Li, C.; Shi, X. Z.; Huang, Y.; Gao, H. J.: Synthesis of monodisperse $CoPt_3$ nanocrystals and their catalytic behavior for growth of boron nanowires. *Nano Research* **2011**, *4*, 780-787.

(64) Huang, H. W.; Yao, W. J.; Wang, X. Y.; Zhai, N. X.; Chen, C. T.: Growth, crystal structure and optical properties of a new layered fluorine beryllium borate, $Sr_{0.23}Ca_{0.77}Na_2Be_2B_2O_6F_2$. *Journal of Alloys and Compounds* **2013**, *558*, 136-141.

(65) Jha, M.; Patra, R.; Ghosh, S.; Ganguli, A. K.: Vertically aligned nanorods of lanthanum hexaboride with efficient field emission properties. *Solid State Communications* **2013**, *153*, 35-39.

(66) Anik, M.; Kucukdeveci, N.; Yilmaz, A.: Charge/discharge characteristics of electroless CoB films. *Thin Solid Films* **2013**, *527*, 69-75.

(67) Bakalova, S.; Speller, R.; Lacey, R. J.; Frost, C.; Kuball, M.: Novel n-type Mg_2B_{14} on silicon diode: demonstration of a thermal solid state neutron detector. *Nuclear Instruments & Methods in Physics Research Section A-Accelerators Spectrometers Detectors and Associated Equipment* **2013**, *700*, 140-144.

(68) Chen, H. H.; Bi, Y.; Cheng, Y.; Ji, G. F.; Peng, F.; Hu, Y. F.: Structural and thermodynamic properties of WB at high pressure and high temperature. *Physica B-Condensed Matter* **2012**, *407*, 4760-4764.

(69) Coskun, S.; Ovecoglu, M. L.: Room-temperature mechanochemical synthesis of W_2B_5 Powders. *Metallurgical and Materials Transactions A-Physical Metallurgy and Materials Science* **2013**, *44A*, 1805-1813.

(70) Garcia-Bustos, E.; Figueroa-Guadarrama, M. A.; Rodriguez-Castro, G. A.; Gomez-Vargas, O. A.; Gallardo-Hernandez, E. A.; Campos-Silva, I.: The wear resistance

of boride layers measured by the four-ball test. *Surface & Coatings Technology* **2013**, *215*, 241-246.

(71) Gouissem, A.; Fan, W.; van Duin, A. C. T.; Sharma, P.: A reactive force-field for zirconium and hafnium di-boride. *Computational Materials Science* **2013**, *70*, 171-177.

(72) Kang, X. D.; Wang, K. K.; Zhong, Y. J.; Yang, B.; Wang, P.: A novel three-step method for preparation of a TiB_2-promoted $LiBH_4$-MgH_2 composite for reversible hydrogen storage. *Physical Chemistry Chemical Physics* **2013**, *15*, 2153-2158.

(73) Knappschneider, A.; Litterscheid, C.; Dzivenko, D.; Kurzman, J. A.; Seshadri, R.; Wagner, N.; Beck, J.; Riedel, R.; Albert, B.: Possible superhardness of CrB_4. *Inorganic Chemistry* **2013**, *52*, 540-542.

(74) Li, H. J.; Yao, D. J.; Fu, Q. G.; Liu, L.; Zhang, Y. L.; Yao, X. Y.; Wang, Y. J.; Li, H. L.: Anti-oxidation and ablation properties of carbon/carbon composites infiltrated by hafnium boride. *Carbon* **2013**, *52*, 418-426.

(75) Meneses-Amador, A.; Campos-Silva, I.; Martinez-Trinidad, J.; Panier, S.; Figueroa-Lopez, U.; Torres-Hernandez, A.: An expression to determine the Vickers indentation fracture toughness obtained by the finite element method on Fe_2B layers. *Surface & Coatings Technology* **2013**, *215*, 285-290.

(76) Rodriguez-Castro, G.; Campos-Silva, I.; Chavez-Gutierrez, E.; Martinez-Trinidad, J.; Hernandez-Sanchez, E.; Torres-Hernandez, A.: Mechanical properties of

FeB and Fe_2B layers estimated by Berkovich nanoindentation on tool borided steel. *Surface & Coatings Technology* **2013**, *215*, 291-299.

(77) Novikov, V. V.; Avdashchenko, D. V.; Bud'ko, S. L.; Mitroshenkov, N. V.; Matovnikov, A. V.; Kim, H.; Tanatar, M. A.; Prozorov, R.: Spin glass and glass-like lattice behaviour in HoB_{66} at low temperatures. *Philosophical Magazine* **2013**, *93*, 1110-1123.

(78) Taghavi, F.; Falamaki, C.; Shabanov, A.; Seyyedi, M.; Zare, M.: An effective method for increasing the activity of nickel boride catalyst nano-particles in hydrogenation reactions: low-temperature hydrogen treatment. *Applied Catalysis A-General* **2013**, *453*, 334-340.

(79) Wang, B.; Liu, Y.; Ye, J. W.; Wang, J.: Electronic, magnetic and elastic properties of Mo_2FeB_2: first-principles calculations. *Computational Materials Science* **2013**, *70*, 133-139.

(80) Yazici, S.; Derin, B.: Effects of process parameters on tungsten boride production from WO_3 by self propagating high temperature synthesis. *Materials Science and Engineering B-Advanced Functional Solid-State Materials* **2013**, *178*, 89-93.

(81) Yin, J.; Huang, Z. R.; Liu, X. J.; Yan, Y. J.; Zhang, H.; Jiang, D. L.: Mechanical properties and in-situ toughening mechanism of pressurelessly densified ZrB_2-TiB_2 ceramic composites. *Materials Science and Engineering A-Structural Materials Properties Microstructure and Processing* **2013**, *565*, 414-419.

(82) Yubuta, K.; Mori, T.; Okada, S.; Prots, Y.; Borrmann, H.; Grin, Y.; Shishido, T.: High-resolution electron microscopy and X-ray diffraction study of intergrowth structures in alpha- and beta-type $YbAlB_4$ single crystals. *Philosophical Magazine* **2013**, *93*, 1054-1064.

(83) Kong, L. T.; Hu, H.; Wang, T. Y.; Huang, D. H.; Fu, J. J.: Synthesis and surface modification of the nanoscale cerium borate as lubricant additive. *Journal of Rare Earths* **2011**, *29*, 1095-1099.

(84) Zhou, Y. F.; Hong, M. C.; Xu, Y. Q.; Chen, B. Q.; Chen, C. Z.; Wang, Y. S.: Preparation and characterization of beta BaB_2O_4 nanoparticles via coprecipitation. *Journal of Crystal Growth* **2005**, *276*, 478-484.

(85) Tao, X. Y.; Wang, X. N.; Li, X. D.: Nanomechanical characterization of one-step, combustion-synthesized $Al_4B_2O_9$ and $Al_{18}B_4O_{33}$ nanowires. *Nano Letters* **2007**, *7*, 3172-3176.

(86) Li, R.; Tao, X. Y.; Li, X. D.: Low temperature, organic-free synthesis of $Ba_3B_6O_9(OH)_6$ nanorods and beta-BaB_2O_4 nanospindles. *Journal of Materials Chemistry* **2009**, *19*, 983-987.

(87) Zhao, Q. R.; Zhu, X.; Bai, X.; Fan, H. H.; Xie, Y.: Synthesis and optical properties of beta-BaB_2O_4 network-like nanostructures. *European Journal of Inorganic Chemistry* **2007**, *13*, 1829-1834.

(88) Menaka; Sharma, S.; Ramanujachary, K. V.; Lofland, S. E.; Ganguli, A. K.: Controlling the size and morphology of anisotropic nanostructures of nickel borate using

microemulsions and their magnetic properties. *Journal of Colloid and Interface Science* **2011**, *360*, 393-397.

(89) Moryc, U.; Ptak, W. S.: Infrared spectra of beta-BaB_2O_4 and LiB_3O_5: new nonlinear optical materials. *Journal of Molecular Structure* **1999**, *512*, 241-249.

(90) Anderson, Y. E.; Filatov, S. K.; Polyakova, I. G.; Bubnova, R. S.: Thermal Behavior of $M^+B_5O_6(OH)_4 \cdot 2H_2O$ (M^+ = K, Rb, Cs) and polymorphic transformations of CsB_5O_8. *Glass Physics and Chemistry* **2004**, *30*, 450-460.

(91) Zhu, Y. C.; Bando, Y.; Ma, R. Z.: Aluminum borate-boron nitride nanocables. *Advanced Materials* **2003**, *15*, 1377-1379.

(92) Korshikova, T. I.; Parkhomenko, S. V.; Tolmachev, A. V.; Tsurikov, V. A.; Yavetskiy, R. P.: Features of strontium tetraborate synthesis by means of borate rearrangement. *Inorganic Materials* **2008**, *44*, 1345-1348.

(93) Datchi, F.; LeToullec, R.; Loubeyre, P.: Improved calibration of the $SrB_4O_7:Sm^{2+}$ optical pressure gauge: advantages at very high pressures and high temperatures. *Journal of Applied Physics* **1997**, *81*, 3333-3339.

(94) Aleksandrovsky, A. S.; Malakhovskii, A. V.; Zabluda, V. N.; Zaitsev, A. I.; Zamkov, A. V.: Optical and magneto-optical spectra of europium-doped strontium tetraborate single crystals. *Journal of Physics and Chemistry of Solids* **2006**, *67*, 1908-1912.

(95) Thakare, D. S.; Omanwar, S. K.; Muthal, P. L.; Dhopte, S. M.; Kondawar, V. K.; Moharil, S. V.: UV-emitting phosphors: synthesis, photoluminescence and applications. *Physica Status Solidi A-Applied Research* **2004**, *201*, 574-581.

(96) Santiago, M.; Lavat, A.; Caselli, E.; Lester, M.; Perisinotti, L. J.; de Figuereido, A. K.; Spano, F.; Ortega, F.: Thermoluminescence of strontium tetraborate. *Physica Status Solidi A-Applied Research* **1998**, *167*, 233-236.

(97) Chenot, C. F.: Phase doundaries in a portion of system $SrO-B_2O_3$. *Journal of the American Ceramic Society* **1967**, *50*, 117-118.

(98) Tang, Z. H.; Chen, X. A.; Li, M.: Synthesis and crystal structure of a new strontium borate, $Sr_2B_{16}O_{26}$. *Solid State Sciences* **2008**, *10*, 894-900.

(99) Ding, W.; Dikin, D. A.; Chen, X.; Piner, R. D.; Ruoff, R. S.; Zussman, E.; Wang, X. N.; Li, X. D.: Mechanics of hydrogenated amorphous carbon deposits from electron-beam-induced deposition of a paraffin precursor. *Journal of Applied Physics* **2005**, *98*, 014905.

(100) Ni, H.; Li, X. D.; Gao, H. S.: Elastic modulus of amorphous SiO_2 nanowires. *Applied Physics Letters* **2006**, *88*, 043108.

(101) Ni, H.; Li, X. D.; Cheng, G. S.; Klie, R.: Elastic modulus of single-crystal GaN nanowires. *Journal of Materials Research* **2006**, *21*, 2882-2887.

(102) Liu, Z. H.; Huang, H. S.: Synthesis and thermochemistry of $SrB_2O_4 \cdot 4H_2O$ and SrB_2O_4. *Thermochimica Acta* **2006**, *448*, 59-62.

(103) Huang, H. S.; Liu, Z. H.: Synthesis and thermochemistry of $SrB_2O_4 \cdot 2.5H_2O$ and $SrB_6O_{10} \cdot 5H_2O$. *Thermochimica Acta* **2007**, *463*, 87-89.

(104) Khattak, G. D.; Tabet, N.; Salim, M. A.: X-ray photoelectron spectroscopic studies of vanadium-strontium-borate $(V_2O_5)_x(SrO)_{0.2}(B_2O_3)_{(0.8-x)}$ oxide glasses. *Journal of Electron Spectroscopy and Related Phenomena* **2003**, *133*, 103-111.

(105) Kim, J. B.; Lee, K. S.; Kim, J. N.: Growth and dielectric properties of SrB_2O_4 single crystal. *Materials Letters* **1997**, *31*, 93-97.

(106) Kim, J. B.; Lee, K. S.; Suh, I. H.; Lee, J. H.; Park, J. R.; Shin, Y. H.: Strontium metaborate, SrB_2O_4. *Acta Crystallographica Section C-Crystal Structure Communications* **1996**, *52*, 498-500.

(107) Tao, X. Y.; Dong, L. X.; Wang, X. N.; Zhang, W. K.; Nelson, B. J.; Li, X. D.: B_4C-nanowires/carbon-microfiber hybrid structures and composites from cotton T-shirts. *Advanced Materials* **2010**, *22*, 2055-2059.

(108) Manupriya; Thind, K. S.; Sharma, G.; Rajendran, V.; Singh, K.; Devi, A. V. G.; Aravindan, S.: Structural and acoustic investigations of calcium borate glasses. *Physica Status Solidi a-Applications and Materials Science* **2006**, *203*, 2356-2364.

(109) Tjong, S. C.; Jiang, W.: Mechanical and thermal behavior of polycarbonate composites reinforced with aluminum borate whiskers. *Journal of Applied Polymer Science* **1999**, *73*, 2247-2253.

(110) Guo, S. Q.; Hu, C. F.; Kagawa, Y.: Mechanochemical processing of nanocrystalline zirconium diboride powder. *Journal of the American Ceramic Society* **2011**, *94*, 3643-3647.

(111) Daw, M. S.; Lawson, J. W.; Bauschlicher, C. W.: Interatomic potentials for zirconium diboride and hafnium diboride. *Computational Materials Science* **2011**, *50*, 2828-2835.

(112) Guicciardi, S.; Melandri, C.; Monteverde, F. T.: Characterization of pop-in phenomena and indentation modulus in a polycrystalline ZrB_2 ceramic. *Journal of the European Ceramic Society* **2010**, *30*, 1027-1034.

(113) Chamberlain, A. L.; Fahrenholtz, W. G.; Hilmas, G. E.: Reactive hot pressing of zirconium diboride. *Journal of the European Ceramic Society* **2009**, *29*, 3401-3408.

(114) Lu, Z. H.; Jiang, D. L.; Zhang, J. X.; Lin, Q. L.: Microstructure and mechanical properties of zirconium diboride obtained by aqueous tape casting process and hot pressing. *Journal of the American Ceramic Society* **2010**, *93*, 4153-4157.

(115) Jayaseelan, D. D.; de Sa, R. G.; Brown, P.; Lee, W. E.: Reactive infiltration processing (RIP) of ultra high temperature ceramics (UHTC) into porous C/C composite tubes. *Journal of the European Ceramic Society* **2011**, *31*, 361-368.

(116) Li, H.; Zhang, L. T.; Zeng, Q. F.; Wang, J. J.; Cheng, L. F.; Ren, H. T.; Guan, K.: Crystal structure and elastic properties of ZrB compared with ZrB_2: a first-principles study. *Computational Materials Science* **2010**, *49*, 814-819.

(117) Sun, C. N.; Gupta, M. C.; Taminger, K. M. B.: Electron beam sintering of zirconium diboride. *Journal of the American Ceramic Society* **2010**, *93*, 2484-2486.

(118) Haque, M. A.; Saif, M. T. A.: Thermo-mechanical properties of nano-scale freestanding aluminum films. *Thin Solid Films* **2005**, *484*, 364-368.

(119) Petrova, H.; Perez-Juste, J.; Zhang, Z. Y.; Zhang, J.; Kosel, T.; Hartland, G. V.: Crystal structure dependence of the elastic constants of gold nanorods. *Journal of Materials Chemistry* **2006**, *16*, 3957-3963.

(120) Park, H. S.; Cai, W.; Espinosa, H. D.; Huang, H. C.: Mechanics of crystalline nanowires. *MRS Bulletin.* **2009**, *34*, 178-183.

(121) Ye, M. F.; Zhong, H. Z.; Zheng, W. J.; Li, R.; Li, Y. F.: Ultralong cadmium hydroxide nanowires: synthesis, characterization, and transformation into CdO nanostrands. *Langmuir* **2007**, *23*, 9064-9068.

(122) Bache, M.; Guo, H. R.; Zhou, B. B.; Zeng, X. L.: The anisotropic Kerr nonlinear refractive index of the beta-barium borate (beta-BaB_2O_4) nonlinear crystal. *Optical Materials Express* **2013**, *3*, 357-382.

(123) Fang, Y. Q.; Wang, Q. W.; Guo, C. G.; Song, Y. M.; Cooper, P. A.: Effect of zinc borate and wood flour on thermal degradation and fire retardancy of polyvinyl chloride (PVC) composites. *Journal of Analytical and Applied Pyrolysis* **2013**, *100*, 230-236.

(124) Li, S. Y.; Zhao, W.; Cui, X. L.; Zhao, Y. Y.; Li, B. C.; Zhang, H. M.; Li, Y. L.; Li, G. X.; Ye, X. S.; Luo, Y. C.: An improved method for synthesis of lithium

difluoro(oxalato)borate and effects of sulfolane on the electrochemical performances of lithium-ion batteries. *Electrochimica Acta* **2013**, *91*, 282-292.

(125) Yang, F.; Liang, Y. J.; Liu, M. Y.; Li, X. J.; Zhang, M. F.; Wang, N.: Photoluminescence properties of novel red-emitting $NaSrBO_3:Eu^{3+}$ phosphor for near-UV light-emitting diodes. *Optics and Laser Technology* **2013**, *46*, 14-19.

(126) Li, S. Y.; Zhao, Y. Y.; Shi, X. M.; Li, B. C.; Xu, X. L.; Zhao, W.; Cui, X. L.: Effect of sulfolane on the performance of lithium bis(oxalato)borate-based electrolytes for advanced lithium ion batteries. *Electrochimica Acta* **2012**, *65*, 221-227.

(127) Afyon, S.; Kundu, D.; Krumeich, F.; Nesper, R.: Nano $LiMnBO_3$, a high-capacity cathode material for Li-ion batteries. *Journal of Power Sources* **2013**, *224*, 145-151.

(128) Erfani, M.; Saion, E.; Soltani, N.; Hashim, M.; Abdullah, W.; Navasery, M.: Facile synthesis of calcium borate nanoparticles and the annealing effect on their structure and size. *International Journal of Molecular Sciences* **2012**, *13*, 14434-14445.

(129) Li, S.; Xu, D. P.; Shen, H. Z.; Zhou, J.; Fan, Y.: Synthesis and Raman properties of magnesium borate micro/nanorods. *Materials Research Bulletin* **2012**, *47*, 3650-3653.

(130) Majchrowski, A.; Lakshminarayana, G.; Reshak, A. H.; Michalski, E.; Olifierczuk, M.; Ozga, K.; Jaroszewicz, L.; Lukasiewicz, T.; Szota, M.; Nabialek, M.: Laser operated elasto-optical features of $La_2CaB_{10}O_{19}:Pr^{3+}$ polymer nanocomposites. *Journal of Luminescence* **2012**, *132*, 2577-2580.

(131) Yu, Z. Y.; Zhao, N. Q.; Liu, E. Z.; Shi, C. S.; Du, X. W.; Wang, J.: Low-temperature synthesis of aluminum borate nanowhiskers on the surface of aluminum powder promoted by ball-milling pretreatment. *Powder Technology* **2011**, *212*, 310-315.

(132) Chen, A. M.; Gu, P.; Ni, Z. M.: 3D flower-like magnesium borate microspheres assembled by nanosheets synthesized via PVP-assisted method. *Materials Letters* **2012**, *68*, 187-189.

(133) Mo, Z. J.; Liang, C. Y.; Lin, J.; Wang, H. S.; Xu, X. W.; Hu, L.; Fan, Y.; Zhang, X. H.; Xue, Y. M.; Tang, C. C.: Synthesis of uniform BN-coated aluminum borate nanowhiskers and their applications in reinforced magnesium matrix composites. *Materials Chemistry and Physics* **2012**, *132*, 347-353.

(134) Sasidharan, M.; Gunawardhana, N.; Luitel, H. N.; Yokoi, T.; Inoue, M.; Yusa, S.; Watari, T.; Yoshio, M.; Tatsumi, T.; Nakashima, K.: Novel $LaBO_3$ hollow nanospheres of size 34 ± 2 nm templated by polymeric micelles. *Journal of Colloid and Interface Science* **2012**, *370*, 51-57.

(135) Chawla, S.; Ravishanker; Khan, A. F.; Yadav, A.; Chander, H.; Shanker, V.: Enhanced luminescence and degradation resistance in Tb modified yttrium borate core-nano silica shell phosphor under UV and VUV excitation. *Applied Surface Science* **2011**, *257*, 7167-7171.

(136) Chen, A. M.; Hu, F. C.; Gu, P.; Ni, Z. M.: Sol-gel synthesis, characterization of nickel borate nanorods. *Chinese Journal of Inorganic Chemistry* **2011**, *27*, 30-34.

(137) Hao, L. F.; Li, J. S.; Xu, X. H.; Ren, T. H.: Preparation and tribological properties of surface-modified borate magnesium nanoparticles. *Journal of Inorganic Materials* **2010**, *25*, 1330-1334.

(138) Hao, L. F.; Li, L. S.; Xu, X. H.; Ren, T. H.: Preparation and tribological properties of a kind of lubricant containing calcium borate nanoparticles as additives. *Industrial Lubrication and Tribology* **2012**, *64*, 16-22.

(139) Kumari, K.; Ram, S.; Kotnala, R. K.: Self-controlled growth of Fe_3BO_6 crystallites in shape of nanorods from iron-borate glass of small templates. *Materials Chemistry and Physics* **2011**, *129*, 1020-1026.

(140) Li, J. S.; Hao, L. F.; Xu, X. H.; Ren, T. H.: Tribological synergism of surface-modified calcium borate nanoparticles and sulfurized olefin. *Industrial Lubrication and Tribology* **2012**, *64*, 217-223.

(141) Li, S. L.; Long, B. H.; Wang, Z. C.; Tian, Y. M.; Zheng, Y. H.; Zhang, Q.: Synthesis of hydrophobic zinc borate nanoflakes and its effect on flame retardant properties of polyethylene. *Journal of Solid State Chemistry* **2010**, *183*, 957-962.

(142) Li, T. B.; Liang, J. A.; Xu, B. S.; Wang, J.: Preparation and characteristic of one-dimensional magnesium borate nanomaterials. *Journal of Inorganic Materials* **2010**, *25*, 947-951.

(143) Menaka; Lofland, S. E.; Ramanujachary, K. V.; Ganguli, A. K.: A new low temperature methodology to obtain pure nanocrystalline nickel borate. *Journal of Organometallic Chemistry* **2010**, *695*, 1002-1005.

(144) Pisarek, J.; Piasecki, M.; Tkaczyk, S.: UV-induced red shift of lithium borate nanocrystallites. *Current Applied Physics* **2011**, *11*, 893-895.

(145) Reddy, C. V.; Krishna, C. R.; Thampy, U. S. U.; Reddy, Y. P.; Rao, P. S.; Ravikumar, R.: Spectral investigations of Cu^{2+} doped beta-barium borate nanopowder by the co-precipitation method. *Physica Scripta* **2011**, *84*.

(146) Shyichuk, A. A.; Lis, S.: Photoluminescence properties of nanosized strontium-yttrium borate phosphor $Sr_3Y_2(BO_3)_4:Eu^{3+}$ obtained by the sol-gel Pechini method. *Journal of Rare Earths* **2011**, *29*, 1161-1165.

(147) Wang, L. J.; He, X. J.; Lu, H. D.; Feng, J. X.; Xie, X. L.; Su, S. P.; Wilkie, C. A.: Flame retardancy of polypropylene (nano)composites containing LDH and zinc borate. *Polymers for Advanced Technologies* **2011**, *22*, 1131-1138.

(148) Xu, S. F.; Chen, A. M.; Ni, Z. M.; Zhao, S. F.: Synthesis and Characterization of OA modified calcium borate nanoplatelets. *Rare Metal Materials and Engineering* **2010**, *39*, 340-343.

(149) Yang, L.; Zhou, L. Q.; Huang, Y.; Tang, Z. W.: Ag-catalyzed synthesis of europium borate $Eu(BO_2)_3$ nanowires, growth mechanism and luminescent properties. *Materials Research Bulletin* **2011**, *46*, 239-243.

(150) Chen, A. M.; Xu, S. F.; Ni, Z. M.: Synthesis, structure and growth mechanism of aluminum borate nanorods. *Acta Physico-Chimica Sinica* **2009**, *25*, 2570-2574.

(151) Hao, L.; Li, J.; Xu, X.; Ren, T.: Preparation, characterization, and tribological evaluation of triethanolamine monooleate-modified lanthanum borate nanoparticles. *Proceedings of the Institution of Mechanical Engineers Part J-Journal of Engineering Tribology* **2010**, *224*, 1163-1171.

(152) Kumari, L.; Li, W. Z.; Kulkarni, S.; Wu, K. H.; Chen, W.; Wang, C. L.; Vannoy, C. H.; Leblanc, R. M.: Effect of surfactants on the structure and morphology of magnesium borate hydroxide nanowhiskers synthesized by hydrothermal route. *Nanoscale Research Letters* **2010**, *5*, 149-157.

(153) Ting, C.; Jian-Cheng, D.; Long-Shuo, W.; Gang, F.: Preparation and characterization of nano-zinc borate by a new method. *Journal of Materials Processing Technology* **2009**, *209*, 4076-4079.

(154) Xu, B. S.; Li, T. B.; Zhang, Y.; Zhang, Z. X.; Liu, X. G.; Zhao, J. F.: New synthetic route and characterization of magnesium borate nanorods. *Crystal Growth & Design* **2008**, *8*, 1218-1222.

(155) Zhang, J.; Li, Z. Q.; Zhang, B.: Formation and structure of single crystalline magnesium borate ($Mg_3B_2O_6$) nanobelts. *Materials Chemistry and Physics* **2006**, *98*, 195-197.

(156) Zheng, Y. H.; Tian, Y. M.; Ma, H. L.; Qu, Y. N.; Wang, Z. C.; An, D. M.; Guan, S. A.; Gao, X. Y.: Synthesis and performance study of zinc borate nanowhiskers. *Colloids and Surfaces A-Physicochemical and Engineering Aspects* **2009**, *339*, 178-184.

(157) Zheng, Y. H.; Wang, Z. C.; Tian, Y. M.; Qu, Y. N.; Li, S. L.; An, D. M.; Chen, X.; Guan, S.: Synthesis and performance of 1D and 2D copper borate nano/microstructures with different morphologies. *Colloids and Surfaces A-Physicochemical and Engineering Aspects* **2009**, *349*, 156-161.

(158) Zhou, J.; Su, D. G.; Luo, J. M.; Zhong, M. F.: Synthesis of aluminum borate nanorods by a low-heating-temperature solid-state precursor method. *Materials Research Bulletin* **2009**, *44*, 224-226.

(159) Tian, Y. M.; He, Y.; Yu, L. X.; Deng, Y. H.; Zheng, Y. H.; Sun, F.; Liu, Z. H.; Wang, Z. C.: In situ and one-step synthesis of hydrophobic zinc borate nanoplatelets. *Colloids and Surfaces A-Physicochemical and Engineering Aspects* **2008**, *312*, 99-103.

(160) Ting, C.; Deng, J. C.; Wang, L. S.; Fan, Y.; Gang, F.: Synthesis of a new netlike nano zinc borate. *Materials Letters* **2008**, *62*, 2057-2059.

(161) Zeng, Y.; Yang, H. B.; Fu, W. Y.; Qiao, L.; Chang, L. X.; Chen, J. J.; Zhu, H. Y.; Li, M. H.; Zou, G. T.: Synthesis of magnesium borate ($Mg_2B_2O_5$) nanowires, growth mechanism and their lubricating properties. *Materials Research Bulletin* **2008**, *43*, 2239-2247.

(162) Zhang, J.; Elsanousi, A.; Lin, J.; Huang, Y.; Elssfah, T. M.; Chen, D. F.; Gao, J. M.; Huang, Z. X.; Ding, X. X.; Tang, C. C.: Aerosol-assisted self-assembly of aluminum borate ($Al_{18}B_4O_{33}$) nanowires into three dimensional hollow spherical architectures. *Crystal Growth & Design* **2007**, *7*, 2764-2767.

(163) Elssfah, E. M.; Elsanousi, A.; Zhang, J.; Song, H. S.; Tang, C. C.: Synthesis of magnesium borate nanorods. *Materials Letters* **2007**, *61*, 4358-4361.

(164) Maia, L. J. Q.; Mastelaro, V. R.; Pairis, S.; Hernandes, A. C.; Ibanez, A.: A sol-gel route for the development of rare-earth aluminum borate nanopowders and transparent thin films. *Journal of Solid State Chemistry* **2007**, *180*, 611-618.

(165) Li, X. D.; Bhushan, B.: Fatigue studies of nanoscale structures for MEMS/NEMS applications using nanoindentation techniques. *Surface & Coatings Technology* **2003**, *163*, 521-526.

(166) Li, X. D.; Wang, X. N.; Xiong, Q. H.; Eklund, P. C.: Mechanical properties of ZnS nanobelts. *Nano Letters* **2005**, *5*, 1982-1986.

(167) Ravindran, P; Fast, L; Korzhavyi, PA; Johansson, B; Wills, J; Eriksson, O.: Density functional theory for calculation of elastic properties of orthorhombic crystals: Application to $TiSi_2$. *Journal of Applied Physics* **1998**, *84*, 4891-4904.

(168) Cuenot, S.; Frétigny C.; Demoustier-Champagne S.; Nysten B.: Surface tension effect on the mechanical properties of nanomaterials measured by atomic force microscopy. *Physics Review B* **2004**, *69*, 165410.

(169) Wang, G. F.; Li, X. D.: Size dependency of the elastic modulus of ZnO nanowires: surface stress effect. *Applied Physics Letters* **2007**, *91*, 231912.

(170) Perdew, J. P.; Wang, Y.: Accurate and simple analytic representation of the electron-gas correlation energy. *Physics Review B* **1992**, *45*, 13244.

(171) Kresse, G.; Hafner, J.: Ab initio molecular dynamics for liquid metals. *Physics Review B* **1993**, *47*, 558.

(172) Kresse, G.; Furthmüller, J.: Efficient iterative schemes for ab initio total-energy calculations using a plane-wave basis set. *Physics Review B* **1996**, *54*, 11169.

(173) Rupesinghe, N. L.; Chhowalla, M.; Teo, K. B. K.; Amaratunga, G. A. J.: Field emission vacuum power switch using vertically aligned carbon nanotubes. *The Journal of Vacuum Science and Technology B* **2003**, *21*, 338-343.

(174) Palnitkar, U. A.; Kashid, R. V.; More, M. A.; Joag, Dilip S.; Panchakarla, L. S.; Rao, C. N. R.: Remarkably low turn-on field emission in undoped, nitrogen-doped, and boron-doped grapheme. *Applied Physics Letters* **2010**, *97*, 063102.

(175) Miller, R. E.; Shenoy, V. B.: Size-dependent elastic properties of nanosized structural elements. *Nanotechnology* **2000**, *11*, 139-147.

(176) McDowell, M. T.; Leach, A. M.; Gall, K.: Bending and tensile deformation of metallic nanowires. *Modelling and Simulation in Materials Science and Engineering* **2008**, *16*, 045003.

(177) Zhang, L.; Huang, H. C.: Young's moduli of ZnO nanoplates: *Ab initio* determinations. Applied Physics Letters **2006**, *89*, *183111*.

(178) G. Wang; X. Li: Predicting Young's modulus of nanowires from first-principles calculations on their surface and bulk materials. *Journal of Applied Physics* **2008**, *104*, 113517.

(179) Kline, S. J.; F. A. McClintock.: Describing uncertainties in single-sample eperiments. *Mechanical Engineering* **1953**, *75*, 3-8.

(180) Li, H.; Zhang, L.; Zeng, Q.; Wang, J.; Cheng, L.; Ren H.; Guan, Kang.: Crystal structure and elastic properties of ZrB compared with ZrB_2: A first-principles study. *Computational Materials Science* **2010**, *49*, 814-819.

APPENDIX A

Copyright Permission Letter for Chapter 3

The Copyright permission letter for Chapter 3 is attached below.

[Rui Li, Xinyong Tao and Xiaodong Li. 2009. *Journal of Materials Chemistry.* 19: 983-987. http://pubs.rsc.org/en/content/articlelanding/2009/jm/b816518a#!divAbstract].

Reproduced by permission of The Royal Society of Chemistry.

RSC | Advancing the Chemical Sciences

Royal Society of Chemistry
Thomas Graham House
Science Park
Milton Road
Cambridge
CB4 0WF

Tel: +44 (0)1223 420 066
Fax: +44 (0)1223 423 623
Email: contracts-copyright@rsc.org

www.rsc.org

Acknowledgements to be used by RSC authors

Authors of RSC books and journal articles can reproduce material (for example a figure) from the RSC publication in a non-RSC publication, including theses, without formally requesting permission providing that the correct acknowledgement is given to the RSC publication. This permission extends to reproduction of large portions of text or the whole article or book chapter when being reproduced in a thesis.

The acknowledgement to be used depends on the RSC publication in which the material was published and the form of the acknowledgements is as follows:

- For material being reproduced from an article in *New Journal of Chemistry* the acknowledgement should be in the form:
    - [Original citation] - Reproduced by permission of The Royal Society of Chemistry (RSC) on behalf of the Centre National de la Recherche Scientifique (CNRS) and the RSC

- For material being reproduced from an article *Photochemical & Photobiological Sciences* the acknowledgement should be in the form:
    - [Original citation] - Reproduced by permission of The Royal Society of Chemistry (RSC) on behalf of the European Society for Photobiology, the European Photochemistry Association, and RSC
- For material being reproduced from an article in *Physical Chemistry Chemical Physics* the acknowledgement should be in the form:
    - [Original citation] - Reproduced by permission of the PCCP Owner Societies
- For material reproduced from books and any other journal the acknowledgement should be in the form:
    - [Original citation] - Reproduced by permission of The Royal Society of Chemistry

The acknowledgement should also include a hyperlink to the article on the RSC website.

The form of the acknowledgement is also specified in the RSC agreement/licence signed by the corresponding author.

Except in cases of republication in a thesis, this express permission does not cover the reproduction of large portions of text from the RSC publication or reproduction of the whole article or book chapter.

A publisher of a non-RSC publication can use this document as proof that permission is granted to use the material in the non-RSC publication.

APPENDIX B

Copyright Permission Letter for Chapter 4

The Copyright permission letter for Chapter 4 is attached below.

[Rui Li, Lihong Bao and Xiaodong Li. 2011. *CrystEngComm.* 13: 5858-5862.

http://pubs.rsc.org/en/Content/ArticleLanding/2011/CE/c1ce05537b#!divAbstract].

Reproduced by permission of The Royal Society of Chemistry.

RSC | Advancing the Chemical Sciences

Royal Society of Chemistry
Thomas Graham House
Science Park
Milton Road
Cambridge
CB4 0WF

Tel: +44 (0)1223 420 066
Fax: +44 (0)1223 423 623
Email: contracts-copyright@rsc.org

www.rsc.org

Acknowledgements to be used by RSC authors

Authors of RSC books and journal articles can reproduce material (for example a figure) from the RSC publication in a non-RSC publication, including theses, without formally requesting permission providing that the correct acknowledgement is given to the RSC publication. This permission extends to reproduction of large portions of text or the whole article or book chapter when being reproduced in a thesis.

The acknowledgement to be used depends on the RSC publication in which the material was published and the form of the acknowledgements is as follows:

- For material being reproduced from an article in *New Journal of Chemistry* the acknowledgement should be in the form:
    - [Original citation] - Reproduced by permission of The Royal Society of Chemistry (RSC) on behalf of the Centre National de la Recherche Scientifique (CNRS) and the RSC

- For material being reproduced from an article *Photochemical & Photobiological Sciences* the acknowledgement should be in the form:
    - [Original citation] - Reproduced by permission of The Royal Society of Chemistry (RSC) on behalf of the European Society for Photobiology, the European Photochemistry Association, and RSC
- For material being reproduced from an article in *Physical Chemistry Chemical Physics* the acknowledgement should be in the form:
    - [Original citation] - Reproduced by permission of the PCCP Owner Societies
- For material reproduced from books and any other journal the acknowledgement should be in the form:
    - [Original citation] - Reproduced by permission of The Royal Society of Chemistry

The acknowledgement should also include a hyperlink to the article on the RSC website.

The form of the acknowledgement is also specified in the RSC agreement/licence signed by the corresponding author.

Except in cases of republication in a thesis, this express permission does not cover the reproduction of large portions of text from the RSC publication or reproduction of the whole article or book chapter.

A publisher of a non-RSC publication can use this document as proof that permission is granted to use the material in the non-RSC publication.
